SLAC-225
UC-34d
(E)

HADRON PRODUCTION BY e^+e^- ANNIHILATION AT CENTER-OF-MASS ENERGIES BETWEEN 2.6 AND 7.8 GeV*

James Leon Siegrist

Stanford Linear Accelerator Center

Stanford University, Stanford, California 94305

October 1979

Prepared for the Department of Energy

under contract number DE-AC03-76SF00515

Printed in the United States of America. Available from National Technical Information Service, U.S. Department of Commerce, 5285 Port Royal Road, Springfield, Virginia 22161. Price: Printed copy $8.00; Microfiche $3.00.

---

* Ph.D. dissertation.

HADRON PRODUCTION BY e^+e^- ANNIHILATION AT CENTER-OF-MASS ENERGIES BETWEEN 2.6 AND 7.8 GeV

Results are presented on multihadron production by e^+e^- annihilation from the Mark I and Mark II detectors at SPEAR. Other than the narrow resonances $\psi(3095)$ and $\psi'(3684)$, the total hadronic cross section varies between 36.5 and 6.4 nb over the center-of-mass energy range 2.6 to 7.8 GeV with complicated structure near 4.1 GeV not completely resolved by these measurements. Evidence for scaling of inclusive momentum distributions of hadrons is presented.

ACKNOWLEDGEMENTS

Completion of this work would not have been possible without the many members of the SLAC-LBL collaboration. I am pleased to acknowledge their contributions, discussions, and encouragement over the years. Special thanks goes to my wife, Kathy, for her support during my graduate studies, and my advisor, R. Schwitters, for his continuous assistance and guidance. Also, I am pleased to thank W. Chinowsky, M. Breidenbach, R. Larsen, and B. Richter for their countless discussions and daily guidance during my graduate studies at SLAC. Finally, I would like to thank the Stanford Physics Department and the SLAC Staff for making my graduate experience a pleasant one.

TABLE OF CONTENTS

I. INTRODUCTION

Hadron production by e^+e^- annihilation proceeds dominantly by the transmission of a single timelike photon between the leptonic and hadronic systems (Figure 1). Other competing processes for hadron production, such as the photon-photon processes (Figure 2), generally have much smaller cross sections in the SPEAR energy range than single photon exchange.[1] In e^+e^- annihilation, the dynamics of the initial state electron and positron are well described by quantum electrodynamics, allowing study of the unknown interactions among the final state particles. All discrete additive quantum numbers (charge, baryon number, lepton number, strangeness,...) in the initial state equal zero, so the total available energy can couple with final states with the quantum numbers of the photon: spin one, negative parity, and negative charge conjugation. Electron-positron annihilation provides a unique probe for studying hadronic interactions.

A useful standard of reference for one photon processes is the reaction $e^+e^- \to \mu^+\mu^-$. The total cross section for muon pair production as calculated with QED in lowest order is

$$\sigma_{\mu\mu} = \frac{4\pi\alpha^2}{3s} \beta \left(\frac{3-\beta^2}{2}\right).$$

Here, s is the center of mass energy squared, β is the

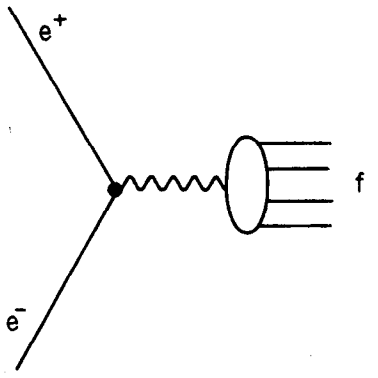

Fig. 1. ONE-PHOTON EXCHANGE

2895A18

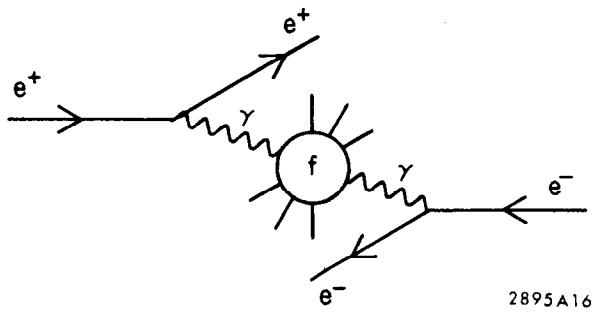

Fig. 2. Schematic diagram of the photon-photon process leading to the final state e^+e^-f.

velocity of the muon in units of the speed of light, and α is the fine structure constant, ~ 1/137. At high energies, where $\beta \approx 1$

$$\sigma_{\mu\mu} = \frac{86.8(\text{nb})}{s(\text{GeV}^2)}$$

The differential cross section for unpolarized incident beams is given at high energies by

$$\frac{d\sigma_{\mu\mu}}{d\Omega} = \frac{\alpha^2}{4s}[1 + \cos^2\theta]$$

where θ is the polar angle relative to the positron beam direction. The s^{-1} cross section dependence is typical for one photon exchange processes in e^+e^- annihilation. Comparison of hadron production with the point-like muon pair cross section occurs naturally in experimental measurements since hadronic yields are usually normalized to electrodynamic processes proportional to $\sigma_{\mu\mu}$. The ratio $R = \sigma(e^+e^- \rightarrow \text{hadrons})/\sigma_{\mu\mu}$ provides a useful measure for hadron production.

Early expectations, which concentrated on two-body hadron production, gave small values of $\sigma(e^+e^- \rightarrow \text{hadrons})$ relative to $\sigma_{\mu\mu}$ because of form factor considerations. Results from pioneering work done at Frascati,[2] Orsay,[3] and Novosibirsk[4] showed that hadrons are produced in e^+e^- annihilation with a large cross section, $R > 1$. Second

generation results from the non-magnetic detector BOLD at CEA,[5] a device with much larger solid angle, showed a higher R value at E_{cm} = 4 and 5 GeV (Figure 3). These results were confirmed by the SLAC-LBL collaboration with measurements at SPEAR that were first presented at the 1973 Irvine Conference.[6] In November 1974, while trying to understand what was thought to be the smooth variation of R with energy, the ψ(J) resonance was discovered.[7] This resonance was discovered independently in pp interactions at Brookhaven[8] and was observed shortly thereafter at Frascati[9] and DESY.[10] A second narrow resonance, the ψ',[11] was discovered at SPEAR just a few days later. The discovery of these resonances indicated a complexity and richness of structure in hadronic production in this energy regime which even today remains to be completely understood.

The large value of R and other characteristics of hadron production in e^+e^- annihilation can be described most easily in terms of a quark parton model.[12] The total hadronic cross section in this model equals the sum of the individual parton pair cross sections, each proportional to the muon pair cross section. The ratio R is just

$$R = \Sigma i(Qi/e)^2$$

where Qi is the charge of the i^{th} spin ½ parton. If a threshold for the production of higher mass partons is reached, then there will be an upward step in R equal to

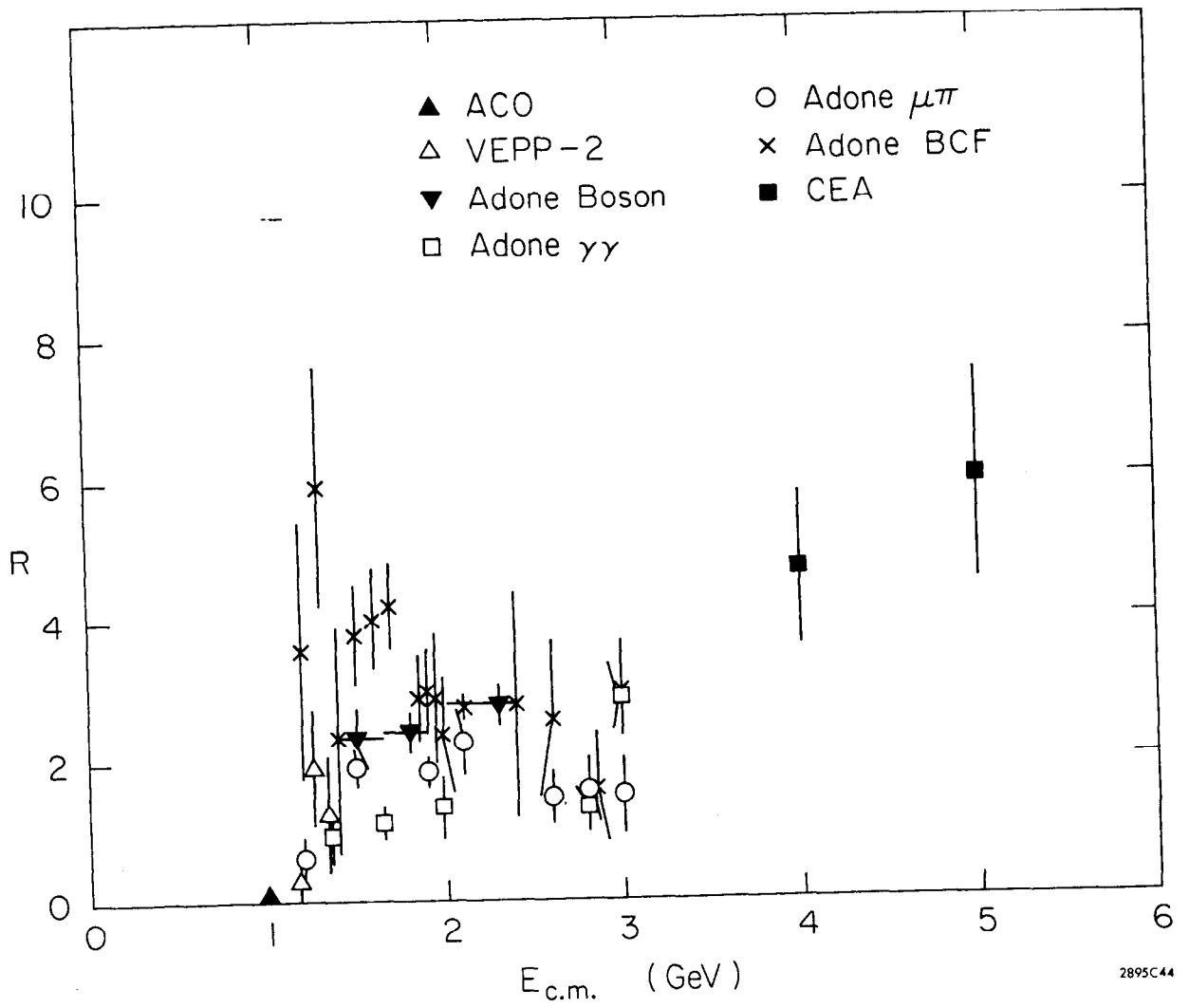

Fig. 3. Early measurements of $R = \sigma(e^+e^- \to \text{hadrons})/\sigma(e^+e^- \to \mu^+\mu^-)$ as a function of center-of-mass energy E_{cm}. Data from Frascati (ADONE),[2] Orsay (ACO),[3] Novosibirsk,[4] and Cambridge (CEA).[5]

the squared charge of the new parton. For fixed numbers of partons of specified charges, R has a constant value and hadron production is said to exhibit scaling. Corrections to this simple model can be calculated using quantum chromodynamics (QCD) to describe the interactions among the final state particles.[13] For all such models, the quantity R is of fundamental significance, giving direct information on the number and properties of the partons produced.

Another aspect of the parton model for hadronic production is the jet-like structure of final states arising from the limited transverse momentum of hadrons relative to the initial parton direction. The angular distribution of the jet axis for spin ½ quark-anti-quark production $(1 + \cos^2\theta)$ has been found to agree with the observed distribution.[14] On quite general grounds, it has been shown[15] that the single-particle inclusive cross sections in the one-photon exchange channel can be written, for the case of no beam polarization, in the form

$$E_f \frac{d^3\sigma}{d^3p_f} = \frac{\alpha^2}{2s^2} \left[(w_1+w_o) + (w_1-w_o)\cos^2\theta\right]$$

where p_f and E_f are the single-particle momentum and energy. The structure functions w_1, w_o are functions of E_f, s, and the particle species. They are defined by

$$w_o = \sum (2\pi)^3 \, \delta^4(P_i - P_f) \, |\langle f|J_z|0\rangle|^2$$

(all final states except p_f)

$$w_1 = \sum (2\pi)^3 \, \delta^4(P_i - P_f) \, |\langle f|J_t|0\rangle|^2$$

(all final states except p_f)

where $\langle f|J_z|0\rangle$ is the matrix element of the final state current J^μ parallel to p_f that gives rise to the state f; $\langle f|J_t|0\rangle$ is the matrix element of a component of J^μ perpendicular to p_f; P_i and P_f are the net four-momenta of the initial and final states. w_o represents the probability that the final state has zero net helicity along p_f, while w_1 gives the probability that the final state has net helicity one along p_f. Bjorken[16] has argued that at high energies hadron production by one photon exchange should exhibit scaling such that w_o and w_1 become functions of only one dimensionless quantity x, the ratio of E_f to the beam energy E. If scaling holds, then

$$\frac{d\sigma}{d\Omega dx} = \frac{\alpha^2}{8s} \, \beta x \left[\left(w_1(x) + w_o(x)\right) + \left(w_1(x) - w_o(x)\right) \cos^2\theta \right]$$

where $\beta = p_f/E_f$ is the particle velocity and $x = E_f/E$. Limitations in statistical accuracy preclude meaningful evaluation of the structure functions from the present data, so we present momentum distributions only as integrals over

production angle. The dependence of $\frac{d\sigma}{dx}$ on x and s reflects the dynamics of the photon-hadron vertex in the single photon exchange process.

In this report, we discuss what has been learned about hadron production, excluding the decay properties of the narrow resonances $\psi(3095)$ and $\psi'(3684)$, with a thorough discussion of the analysis procedures and systematic errors. The measurements reported here are the most complete in this energy range to date. In Section II we describe the Mark I apparatus, Section III has details of the event selection procedures in the Mark I, and Section IV describes the procedures for detection efficiency determination. Results on R and the single particle inclusive momentum distributions from Mark I data are presented and compared with published results from PLUTO and DASP in Section V. In Sections VI, VII, and VIII we describe the Mark II detector, Mark II event selection procedures, and present preliminary results from the Mark II on R and the single particle inclusive momentum spectra.

II. APPARATUS

A. SPEAR

The advantage of the simplicity of the initial state in electron positron colliding beam machines is gained at the expense of rate of interactions. The maximum current that can be collided in each beam in SPEAR depends on the machine energy and ranges up to 35 mA/beam. The upper limit on the beam current is set by overheating of the vacuum chamber due to Ohmic losses from beam-induced currents in the wall. The energy range of SPEAR is 1.3 to 3.9 GeV/beam. Beams are injected into SPEAR from the SLAC linac up to the maximum injection line energy, 2.5 GeV. The typical residual pressure around the ring is $\sim 10^{-9}$ torr and beam lifetimes are typically four hours. Figure 4 shows the average luminosity delivered, taking into account time for injection, beam loss, and other interruptions.

The beams are separated electrostatically during injection, acceleration, and special runs for background measurement. Each beam is stored as a single bunch, with beams crossing in each experimental area once every 780 nsec. When the separating plates are turned off, the beams collide in a region of Gaussian shape with FWHM 0.01 cm in the vertical and 0.2 cm in the horizontal transverse directions, and an energy dependent length along the beam line of a few centimeters.

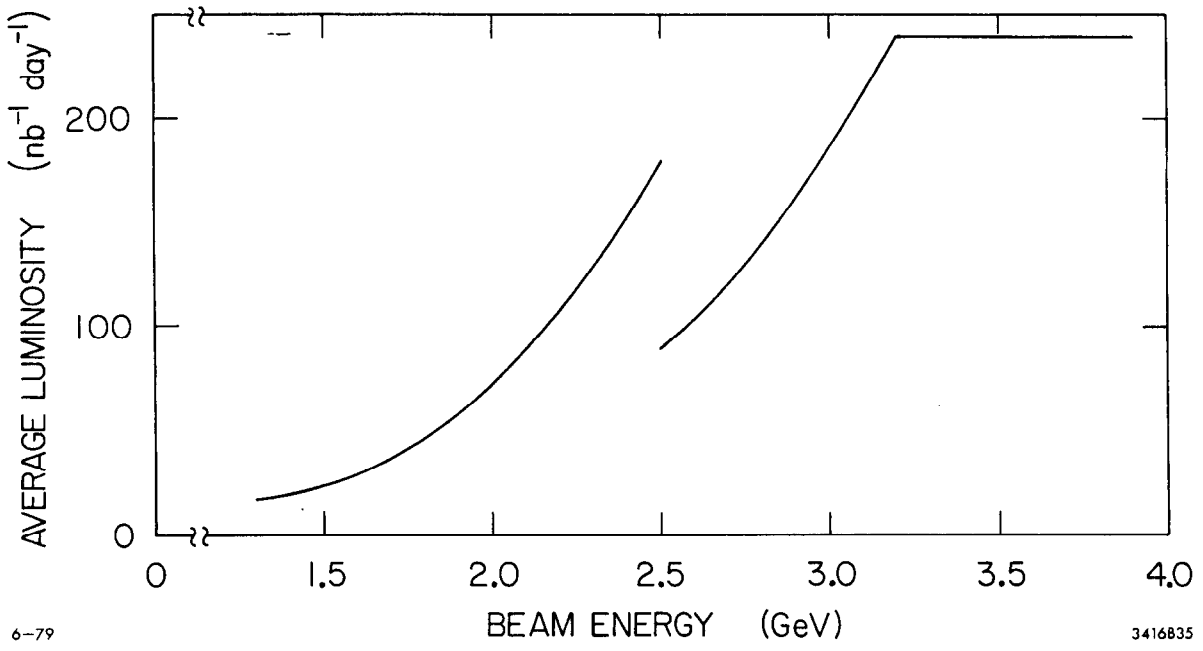

Fig. 4. Average luminosity delivered at SPEAR versus beam energy.

The machine energy is determined by the bend magnet current, and is monitored by a flip coil measuring $\int B.d\ell$ in a reference bend magnet connected in series with the ring magnets. The energy determined from the flip coil measurement is corrected for orbit distortions. The uncertainty is estimated to be ±0.1% in the calibration of the energy and ±0.1 MeV in setting the energy. The energy spread of the beam is determined by fluctuations in synchrotron radiation. This spread in beam energy E is typically (FWHM) $\delta E/E \simeq 0.05\% \times E(GeV)$. Measurement and monitoring of the beam energy and its spread are particularly important for running in the region of the narrow resonances ψ, ψ'.

B. The Mark I Magnetic Detector

The SLAC-LBL Mark I magnetic detector occupied the West experimental area at SPEAR from 1973 to summer 1976. The purpose of the detector was to provide as large a solid angle coverage as possible for the measurement of the properties of the final state particles produced in the beam collision region. The detector covered 50° to 130° in polar angle (θ, with respect to the e^+ beam) with 2π azimuthal (ϕ) acceptance, for a total of 0.65 of 4π solid angle coverage. Figures 5 and 6 present an end view and a sectioned side view of the apparatus.

Particles emerging from the region of the beam collision passed in sequence through the vacuum chamber, cylindrical scintillation counters immediately surrounding

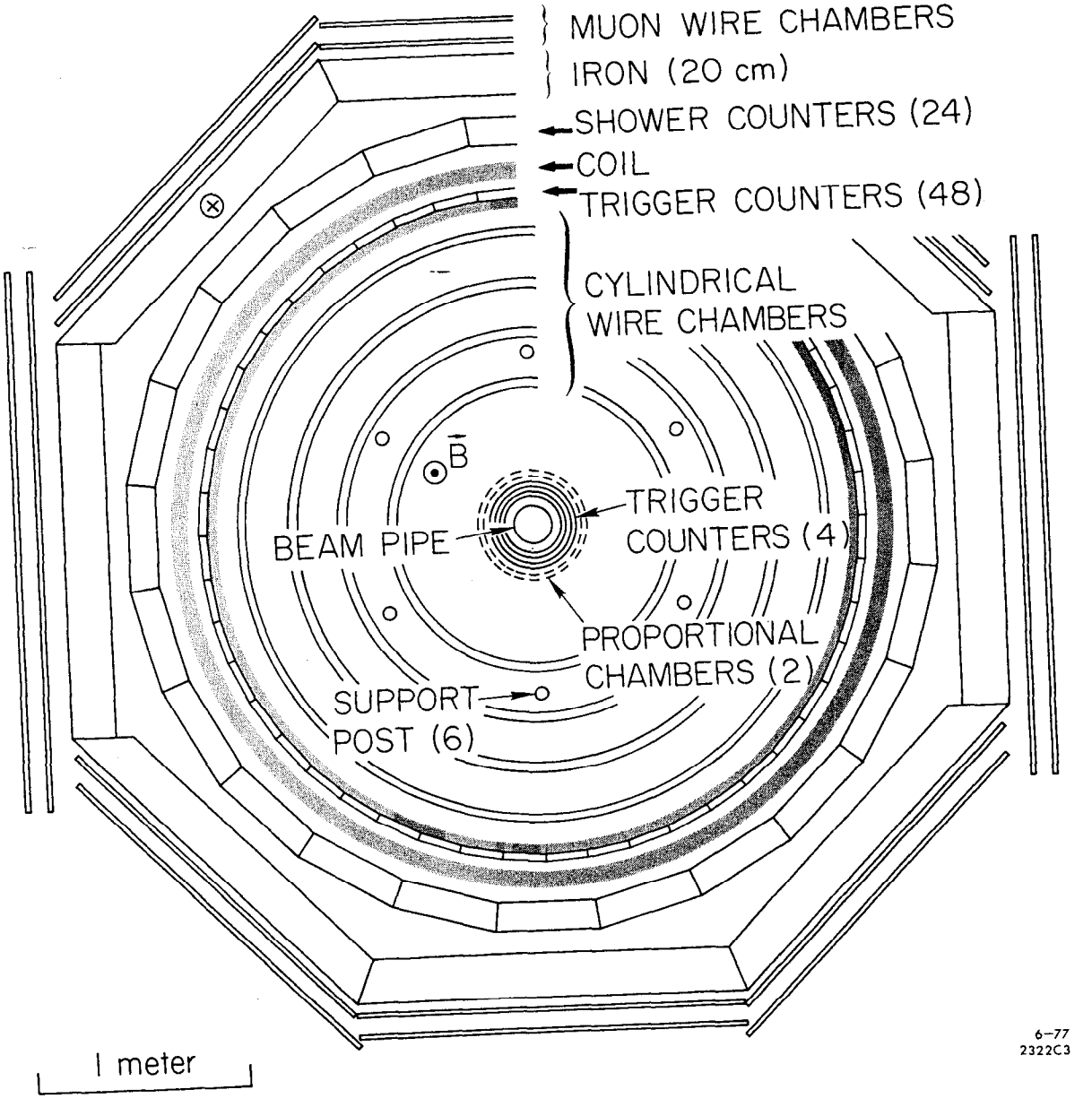

Fig. 5. End view, Mark I magnetic detector.

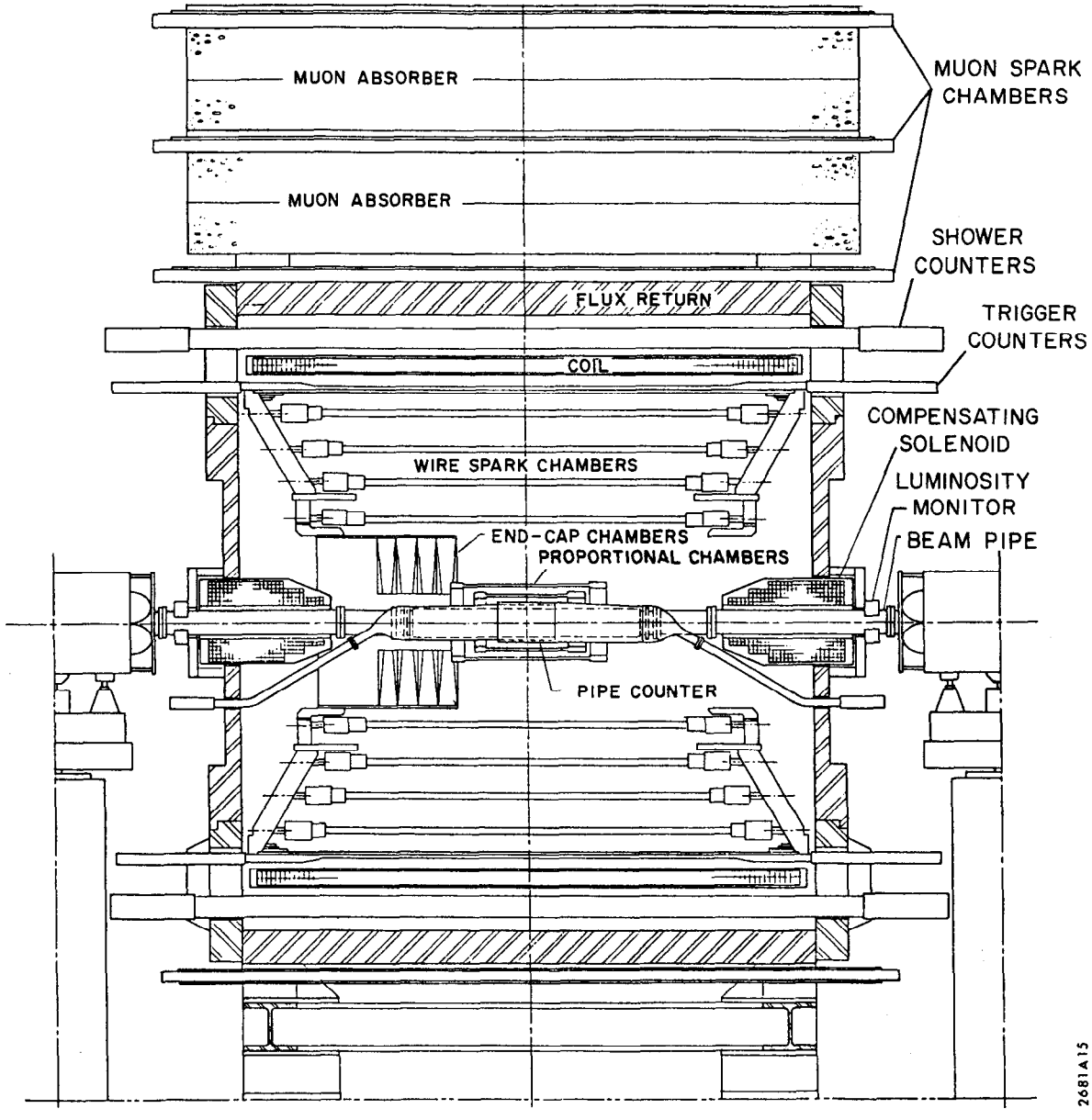

Fig. 6. Sectioned side view, Mark I magnetic detector.

the vacuum chamber, a system of magnetostrictive spark chambers, an array of time-of-flight scintillation counters, the magnet coil, an array of lead and scintillator shower counters, the magnet flux return iron, and finally a set of planar spark chambers for muon identification. Table 1 presents the radii, lengths, angular range covered, and thickness of each of the detector components.

The vacuum chamber was a corrugated cylinder of stainless steel. The four hemi-cylindrical plastic scintillation counters immediately surrounding the vacuum pipe ("pipe counters") were each viewed through a Lucite light pipe by a 56DVP phototube. The primary purpose of these counters was to reduce the detector trigger rate from cosmic rays. The two sets of proportional wire chambers just outside the pipe counters had a wire spacing of 0.21 cm and 0.28 cm, respectively. The gas mixture used was 18.7% carbon dioxide, 6.3% ethyl bromide, and 75% argon. Signals from the proportional chamber wires were latched after each beam crossing. This set of chambers had a rms spatial resolution in the azimuthal direction of 700μ, with no usable resolution along the beam line (z).

Each of the four sets of cylindrical wire spark chambers consisted of 2 gaps, one with wires at $\pm 2^{o}$ and one with wires at $\pm 4^{o}$ with respect to the beam line. Signals from both ground and high voltage wires were recorded using a magnetostrictive technique. A gas mixture of 90% neon

TABLE 1

MARK I DETECTOR COMPONENTS

(all dimensions in cm)

Item	Average Radius	Fraction of 4π Acceptance	Length (z)	Thickness	Fraction of Radiation Length	Fraction of Absorption Length
Beampipe	8.0	-	-	0.0273	0.016	0.002
Pipe Counters	12.0	0.83	90	1.37	0.033	0.020
MWPC1	17.3	0.82	$\pm$25	1.98	0.0066	-
MWPC2	22.4	0.88	$\pm$41	1.98	0.0066	-
WSC1	66	0.86	$\pm$110	3.8	0.0017	0.001
WSC2	91	0.77	$\pm$110	3.8	0.0017	0.001
WSC3	112	0.73	$\pm$120	3.8	0.0017	0.001
WSC4	135	0.71	$\pm$134	3.8	0.0017	0.001
TOF Counters	152.4	0.65	$\pm$130	2.5	0.060	0.037
Coil	166.4	0.74	$\pm$182.9	11.0	1.0	0.24
Shower Counters	178.4	0.66	$\pm$155	13.0	5.79	0.22
Flux Return	211	-	$\pm$183	20.0	11.4	1.17
Muon WSC	219	0.73	$\pm$234	5.7	0.22	0.07

and 10% helium was used. The chambers had a 1.1 mm wire spacing and an rms spatial resolution in the azimuthal direction of 340μ. In the z direction, the rms resolution was 1.0 cm and 0.5 cm for 2^{o} and 4^{o} stereo gaps, respectively.

Immediately outside the spark chambers was a ring of 48 plastic scintillation counters, each 20 cm wide, viewed at each end by a 56DVP phototube. These counters ("trigger counters") determined flight times for use in charged particle identification and were used in the detector trigger. Signal pulse heights were recorded in order to enable off-line correction for time slewing. The rms time-of-flight resolution for this system was about 350 psec.

Outside the solenoid coil was an array of 24 shower counters each constructed of 5 sheets of 0.64-cm thick Pilot F scintillator interleaved with 5 sheets of 0.64 cm thick lead. Each counter was 48 cm wide, viewed on each end by an RCA 4522 phototube. This set of counters provided electron-hadron identification information and was also used in the detector trigger. The rms energy resolution averaged over all counters, as measured with Bhabha events, was $\delta E/E \sim 35\%/\sqrt{E}$. The muon identification spark chamber planes, the endcap spark chambers, and the photon detection capabilities of the shower counters were not used in this analysis; they are discussed in Reference 17.

The magnetic field was generated by a solenoid in series with two compensation coils that served to ensure the $\int B.d\ell$ along the beam line was zero, a necessary condition for stable beam storage. The magnet dissipated 2.8 MW at the operating current of 4350 Amp. The solenoid field was monitored by measuring the voltage across a shunt that was calibrated during field mapping. The field was mapped with a Hall probe before the tracking chamber package was inserted into the coil. Field components were measured at about 5000 points over the tracking volume r = 20 to 140 cm, z = -125 to +125 cm. The variation of the field magnitude was less than 3%. A polynomial expression in r and z only was fit to the field data to yield a parameterization accurate to 0.05% in B_z and 3 Gauss in B_r and B_ϕ. The absolute value of the field strength was measured at the center of the magnet by a magnetic resonance probe to be 3891±1 Gauss at the operating current. The error in the measured track momenta due to uncertainty in the field is much less than that due to the measurement error in the tracking chambers.

C. Trigger

The Mark I trigger was derived from signals from a beam pickup electrode, the pipe counters, trigger counters, and shower counters. All coincidences were formed using a 15 nsec wide gate derived from the beam pickup electrode

signal. About 200 nsec after beam crossing, the various counter latches were interrogated to find if a valid latch configuration for triggering had been made. If not, the latches were cleared and the system made ready for the next beam crossing. If a valid latch configuration was found, the spark chamber high voltage was pulsed and the time and pulse height digitizers were started. After delay, the counter and spark chamber data were transferred via CAMAC to an XDS Sigma V computer which wrote $\sim$3 k bytes per event on tape. A randomly selected sample ($\sim$20%) of the recorded events were also analyzed on-line in the computer. These data were used for monitoring chamber and counter efficiencies and general detector performance. The trigger system was disabled for $\sim$.2 seconds while the spark chamber charging lines recharged and the data were written on tape.

The maximum trigger rate that could be tolerated was a few events per second because of the dead time during the spark chamber high voltage recharge. Coincidences between two or more trigger counters with 25 mA stored beam current occurred at a rate of $\sim$3 KHz. An examination of events obtained with such a trigger revealed that the majority of annihilation events contained at least one charged track with momentum $\geq$ 300 MeV. To reject the background, we required a configuration of a trigger counter in coincidence with the shower counter at the same or adjacent azimuths ("trigger-associated-shower", or "TASH"). The TASH

requirement in effect picked out charged tracks with momenta $\gtrsim$ 300 MeV. Two or more of the four pipe counter latches were required in the trigger coincidence to reduce the cosmic-ray background. To finally reduce the trigger rate to an acceptable level, a coincidence of two TASH configurations with at least two pipe counter latches was required. The event rate was at most 3 per second at all energies.

Inefficiencies in the pipe counters caused losses of < 1% of hadronic events. However, the TASH requirement had a significant effect on the multihadron detection efficiency by introducing a momentum bias in triggering.

For minimum ionizing particles, the TASH inefficiency is due to losses in gaps at counter edges, and light loss through attenuation. This inefficiency was measured using cosmic-ray data. Figure 7 shows the shower counter efficiency as a function of z position along the beam line, averaged over all 24 shower counters. The effect of this inefficiency is included in Monte Carlo simulations of the detector.

Hadron prongs of multihadron annihilation events suffer effects that cause further TASH coincidence inefficiency. Low momentum particles can range out in the solenoid coil ($\sim$ 25 gm/cm^2) and some hadrons interact before reaching the shower counter. The TASH efficiency was measured using events with three or more charged particles detected using an algorithm to correct for the two TASH hardware trigger

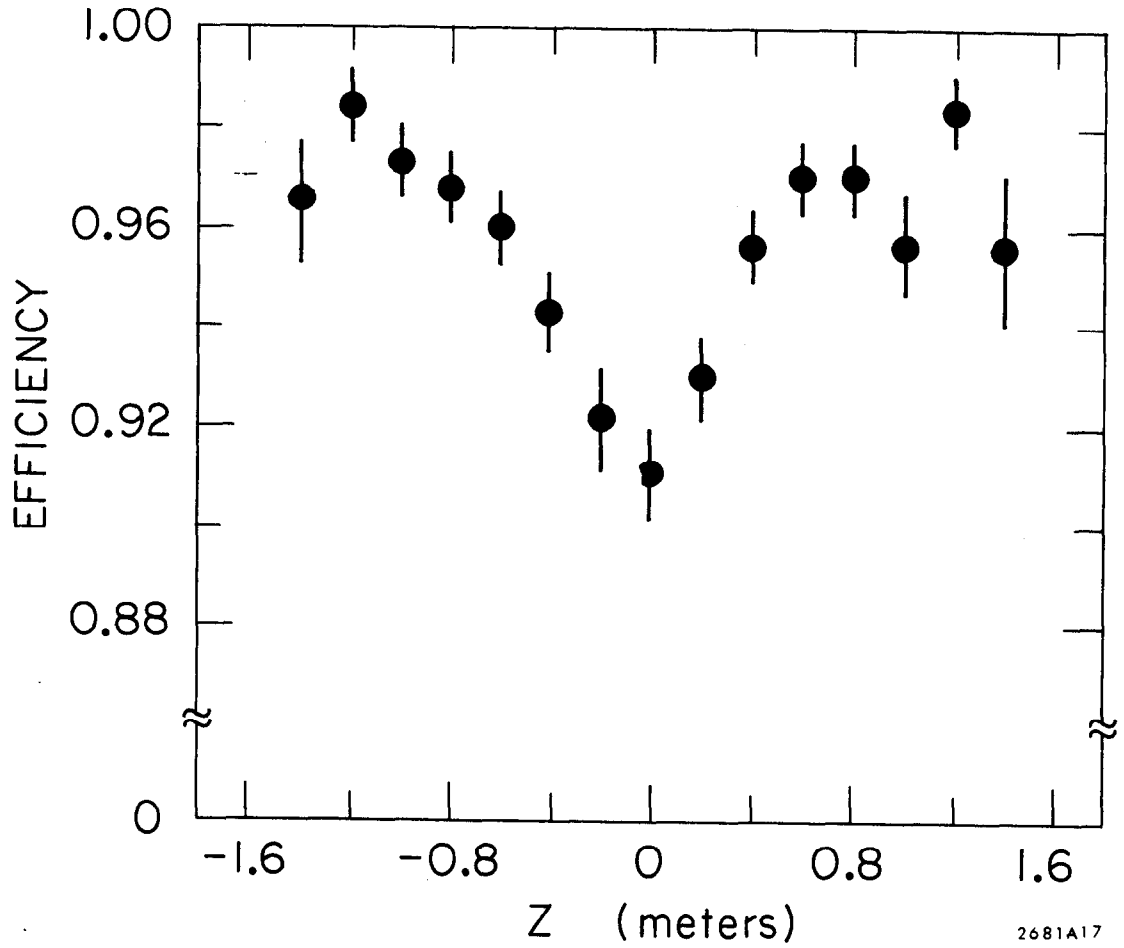

Fig. 7. Shower counter efficiency versus z position along the beam line as measured using cosmic-ray data.

requirement .[18] The measured TASH efficiency as a function of momentum for all charged tracks in multihadron events is shown in Figure 8. The arrow marks the accidental TASH probability as measured by the latching probability for shower counters not associated with charged tracks in multihadron events.[19] These single particle TASH coincidence efficiencies have an important effect on the detection efficiency and are included in Monte Carlo simulations of the detector.

D. Tracking[20]

To reconstruct tracks we first search for candidate track points in each of the four sets of cylindrical spark chambers. All points of intersection of oppositely oriented stereo wires in each of the eight spark gaps are found for each event. Each such intersection is used to define a search area ($\Delta\phi$ = 0.1 radians, Δz = 0.15 m) on the other gap of the set. Wires or intersections on the other gap within this search area are combined with the first intersection to define 3 or 4 wire space points, respectively. All remaining unpaired intersections on either gap define 2 wire space points. Any of 2, 3, or 4 wire space points can be used by the track recognition programs, that start with a selection of pairs of points from the two outer sets of chambers. These, with the origin, define a candidate track helix. Points in the inner sets of chambers falling within tolerances of the candidate track are added to the

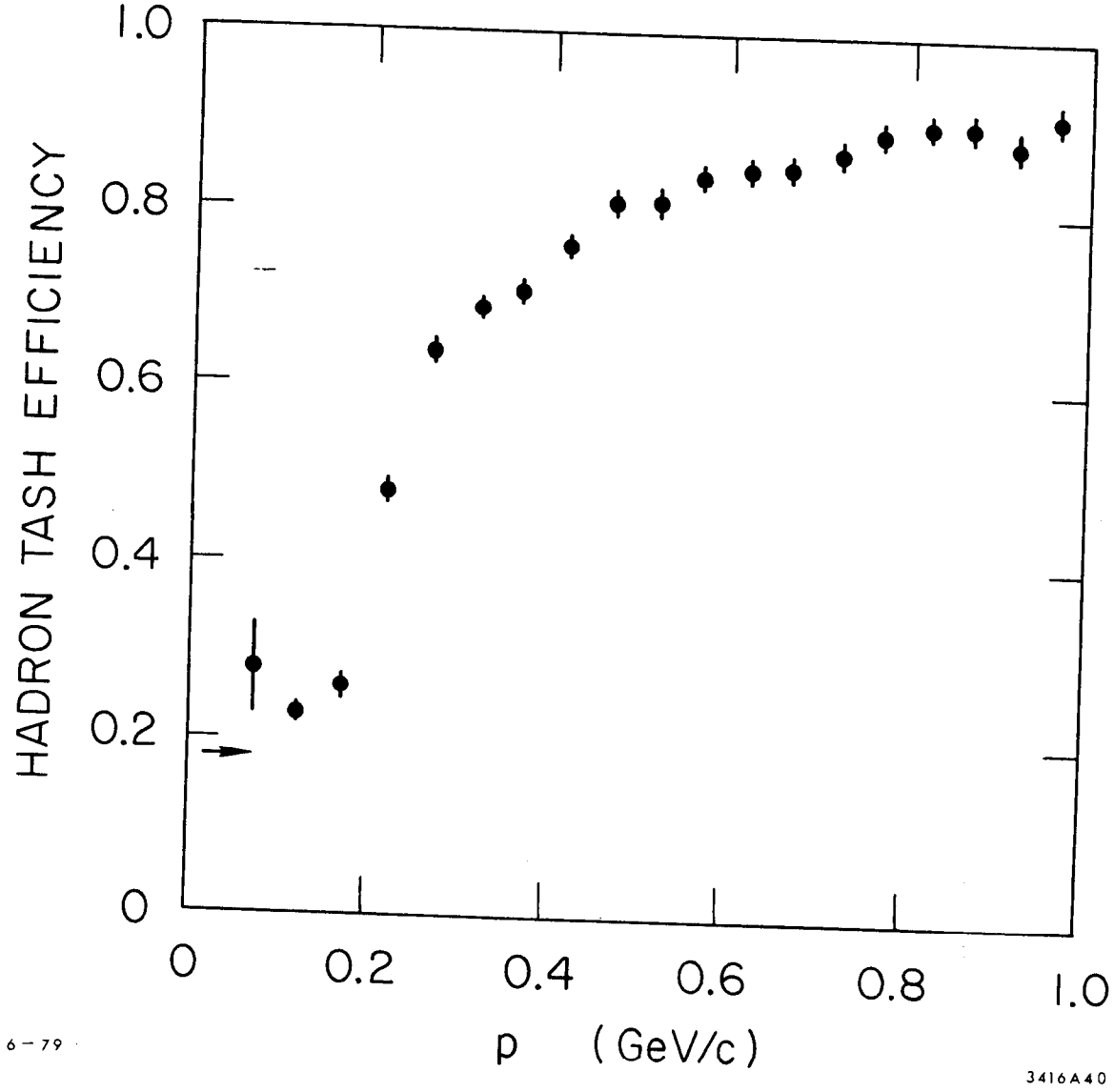

Fig. 8. TASH coincidence efficiency versus track momentum in multihadron events. The arrow marks the accidental TASH coincidence rate.

list of possible points. Tracks are required to have points in three or more sets of chambers to merit further consideration.

This type of space point and track definition has a track recognition efficiency almost independent of variations in the spark efficiency on a single gap. The system efficiency for the purposes of track recognition is increased, since a gap efficiency of ∿90% gives a space-point efficiency of 98 to 99%.

At high beam energies (> 3.5 GeV/beam), synchrotron radiation from the beam caused an increase in the number of random 2-wire space points. A visual scan of events revealed that spurious tracks from this source were about 6% of the total and were concentrated at momenta ≤150 MeV. At lower incident energies, fewer than 1% of tracks were judged to be spurious. To avoid this problem, data above 3.5 GeV/beam use 3 and 4 wire points only, and hadronic tracks below 150 MeV transverse momentum relative to the beam are ignored at all energies. The resulting tracking efficiency for tracks >150 MeV is >98% and is independent of multiplicity as determined by a visual scan of about 1000 hadronic events.

To construct an event vertex, tracks found by the above procedure were classified as primary or secondary, according to the value of the distance of closest approach to the beam axis (R_{min}). Primary tracks have R_{min} ≤0.15 m

and $|z| \leq 0.6$ m at R_{min}. All other tracks are classed as secondaries. The vertex is that point which minimizes the sum of the perpendicular distances to each primary track. In the χ^2 minimization procedure, weights were assigned based on individual track fits, taking into account position resolution and multiple scattering. The vertex distributions in radius and z of a randomly chosen sample of events are shown in Figures 9 and 10. The background of events with vertices at large z is due to interactions of the beam with residual gas. In addition, the vertex radial distribution shows a concentration of events at radii near $\sim$8 cm due to interactions of off-momentum beam particles in the beam pipe and pipe counters.

For annihilation events, the track fits and hence the momentum resolution were improved by constraining all tracks to a common vertex position and refitting them. The transverse position of the interaction point was measured in Bhabha scattering events with a precision of $\lesssim$0.5 mm in x and y. This beam constrained fit was further improved by ad-hoc corrections to angles and momenta determined from study of Bhabha events. These corrections for slight errors in the beam position and chamber alignment constants altered measured quantities by less than 2%. After all corrections, the rms momentum resolution was found to be

$$\delta p/p \simeq [(0.013\ p(\text{GeV}))^2 + (0.006)^2]^{\frac{1}{2}}$$

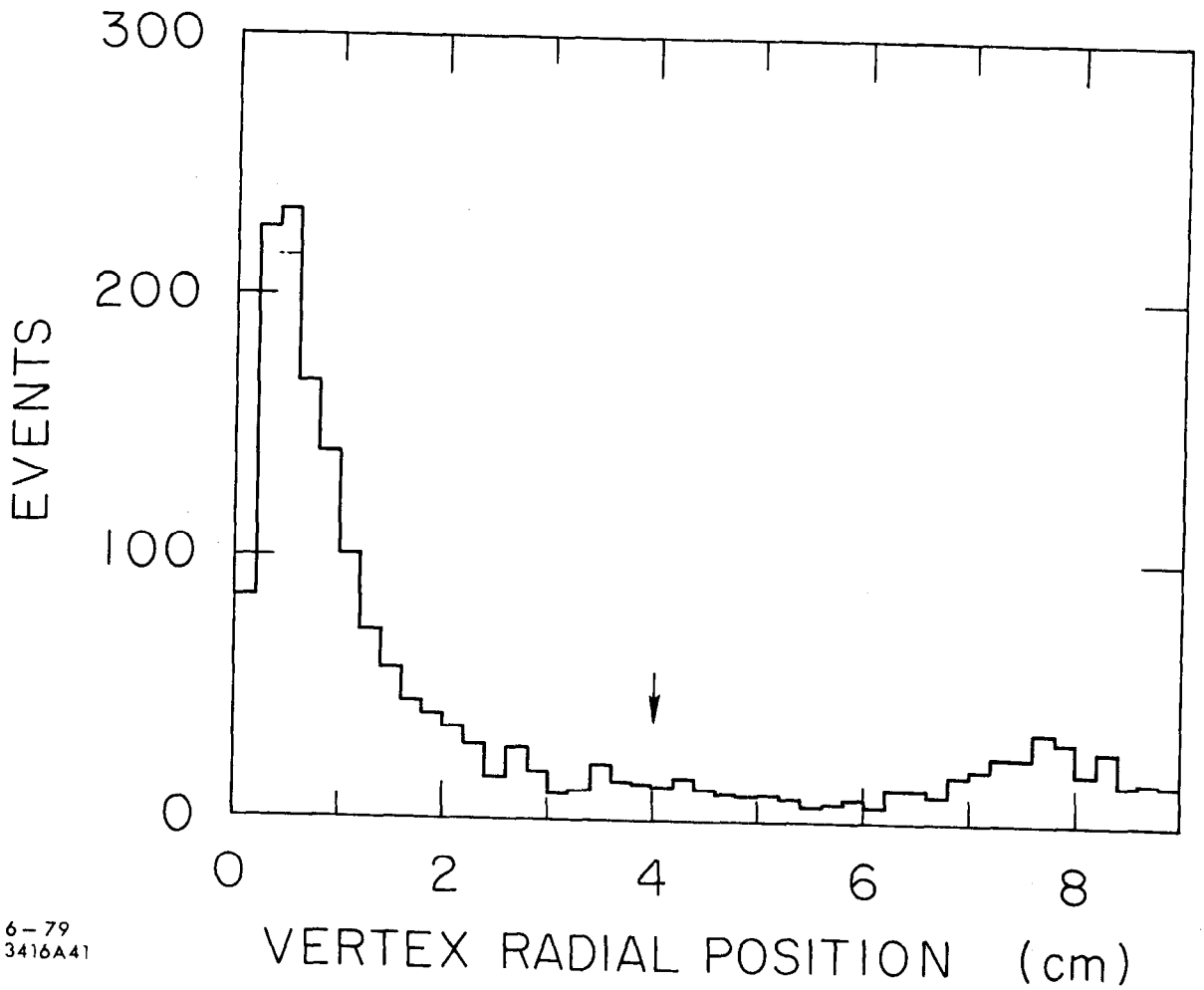

Fig. 9. Radial distribution of event vertices. The arrow marks the vertex radius cut for hadronic event definition.

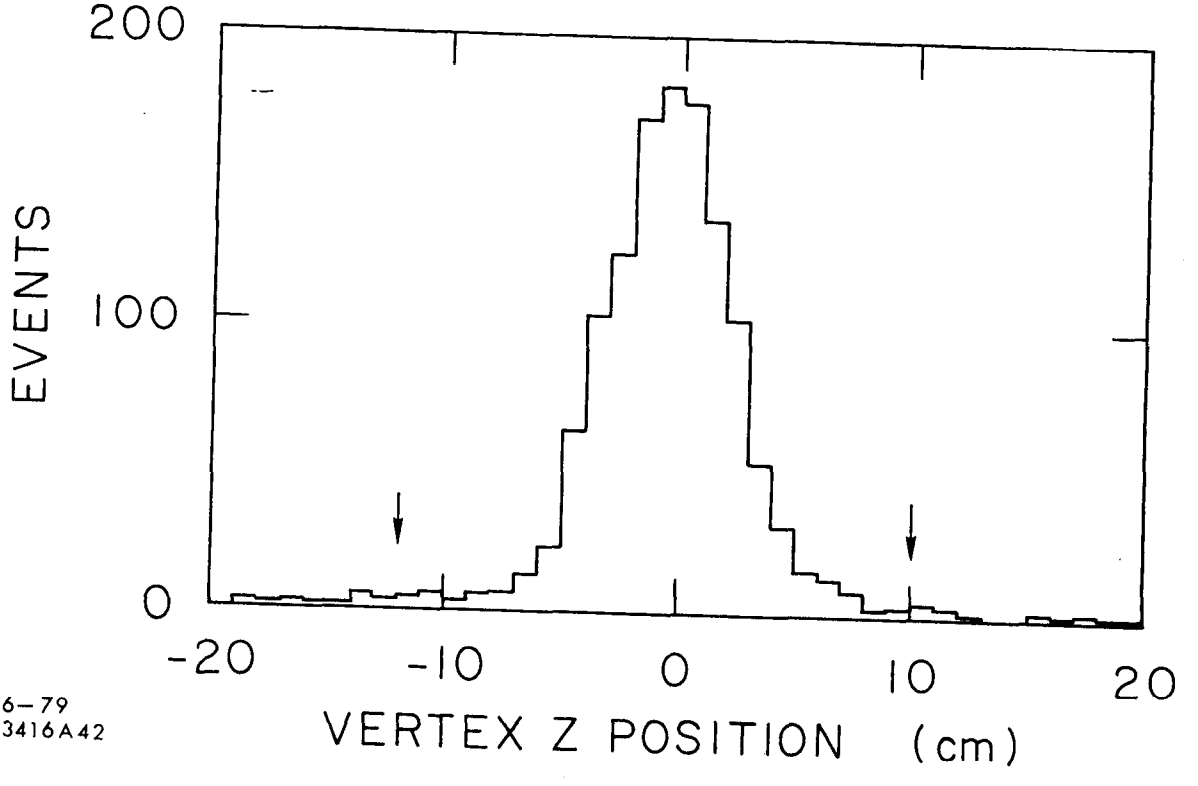

Fig. 10. z distribution of event vertices for events with vertex radius <4 cm. The arrows mark the boundaries of the signal region.

III. EVENT SELECTION AND BACKGROUND REMOVAL IN THE MARK I DETECTOR

Events were selected by requiring that the vertex be within the volume $r \leq 15$ cm, $|z| \leq 40$ cm and that there be two TASH with a charged track projecting to each. In addition to events from the reaction $e^+e^- \rightarrow$ hadrons, the event sample contains the following background: cosmic rays, elastic scatters, muon pairs, two photon exchange events, beam-gas interactions, beam-wall interactions, and heavy lepton decays. About 25% of the events logged on tape during colliding beam running are hadronic events and about 25% are elastic scatters or muon pairs. Two prong events in which tracks are collinear to within 10° were labelled cosmic rays if the time of flight counters recorded a difference in time expected of a single particle crossing the detector. Such events were removed from further consideration.

A. Hadronic Event Selection

The cuts applied to the data depend on the observed topology:

1. Two prong events; to be retained in the hadron sample we required that the sum of the charges be zero, that the azimuthal angle between the tracks be greater than 20° and less than 160°, and that each track have momentum greater than 300 MeV. These cuts eliminate the Bhabha and

muon pair events from the two-prong sample and reduced events from the two photon exchange process to less than 2% (Section III. b).

2. Greater-than-two prong events; we removed from the hadron category events that have either a) one or more tracks identified as an electron[21] and a pair of oppositely charged tracks forming a space angle greater than 170°, or b) a pair of oppositely charged tracks with summed pulse height greater than 100, an azimuthal angle between them greater than 175°, and each track having an $x > 0.4$ ($x = 2p/\sqrt{s}$). These cuts remove Bhabha events which contain a radiated photon which converts in the vacuum chamber or adjacent material.

To evaluate the systematic uncertainty in the sample of retained hadron events, a large number of events were visually scanned by physicists. In a sample that contained about 1000 hadron events we found about 20 events incorrectly classified by the foregoing criteria.

B. Backgrounds

After passing the above cuts, the remaining hadronic event sample contains background events from collisions of the beam with residual gas or the vacuum chamber wall, from the two photon processes $e^+e^- \to e^+e^-e^+e^-$ and $e^+e^- \to e^+e^-\mu^+\mu^-$ that survived the cuts, and from heavy lepton decays.

Effectively all events produced in the vacuum chamber wall are eliminated by imposing a vertex radial position cut, $r < 4$ cm. We estimate 5±3% of annihilation events were lost because of this cut.

Interactions of beam particles with residual gas nuclei yield events whose vertices are broadly distributed in z, as verified by study of events produced during single-beam operation of SPEAR. Only events whose vertices lie in the interval $-0.12 < z \leq 0.10$ m were called beam-beam events (Figure 10). The contamination of beam-gas events is determined to be ≤5% from the observed yields in the regions $-0.17 \leq z \leq -0.12$ and $0.10 \leq z \leq 0.17$. To correct for this background, distributions in multiplicity and momentum were formed from events from the signal and background z regions, and the distributions subtracted.

The number of events from the two-photon exchange processes that survived the cuts is estimated by a calculation[22] and displayed as a function of energy in Figure 11. This subtraction is less than 2% of hadronic events. No correction was made for the process $e^+e^- \to e^+e^-$ + hadrons, whose cross section is expected to be small[23] relative to the detected cross section for $e^+e^- \to e^+e^-e^+e^-$ or $e^+e^- \to e^+e^-\mu^+\mu^-$ at these energies.

The number of events originating from the decay of the heavy lepton τ[24] to be removed from the sample was determined by a Monte Carlo calculation. Model parameters used in the calculation are shown in Table 2. This subtraction is about

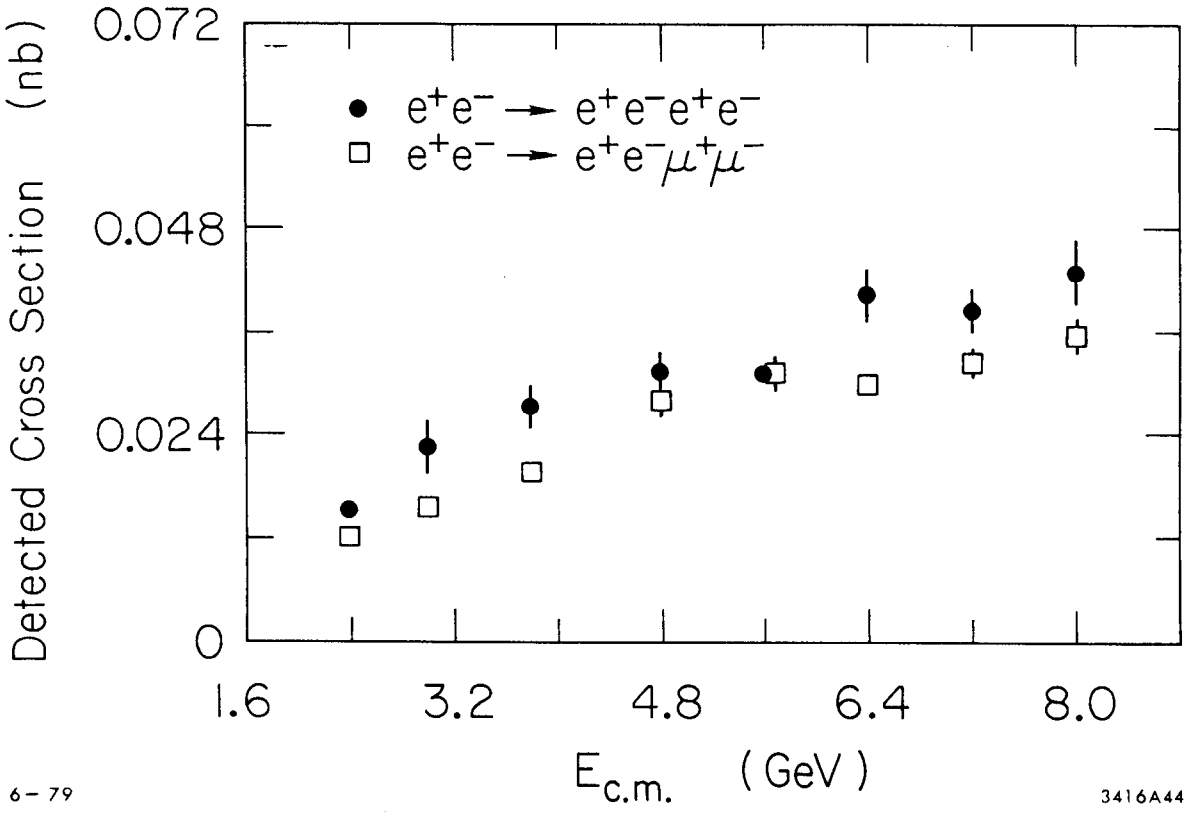

Fig. 11. Calculated detected cross sections for the processes $e^+e^- \rightarrow e^+e^-\mu^+\mu^-$ and $e^+e^- \rightarrow e^+e^-e^+e^-$ versus the center-of-mass energy.

TABLE 2

MONTE CARLO PARAMETERS USED FOR CALCULATION OF THE EXPECTED NUMBER OF DETECTED τ DECAY EVENTS

(Mark I)

Mass	1.78 GeV
Branching Fractions	
$\tau \rightarrow e\nu\nu$	0.20
$\mu\nu\nu$	0.20
$\pi\nu + K\nu$	0.13
$\rho\nu$	0.24
Continuum ν	0.23

10% of detected hadronic events. We prefer to subtract the τ contribution from the detected event sample rather than from the final corrected measured cross section because the detection efficiency corrections to the measured cross section depend on the production mechanism for the events; multihadronic detection efficiencies may not be applicable to τ decays.

C. Bhabha and Muon Pair Events

Selection of events from the reactions $e^+e^- \to e^+e^-$ and $e^+e^- \to \mu^+\mu^-$ has been discussed in Reference 25. These events are used to determine the time integrated incident beam luminosity. The time integrated luminosity measurement is the ratio of the number of Bhabha scattering events detected to the corresponding calculated production cross section.[26] Two checks on this measurement are the number of muon pair events detected and the number of small angle Bhabha scattering events detected in four arrangements of scintillation counters ("luminosity monitor") each centered at 20 mrad to the beam line. Within statistical errors, the luminosity measured from the muon pair events agrees with the Bhabha measurement, at all energies (Figure 12). The luminosity monitor provided high statistical accuracy (counting rate $\approx$10 Hz), but the measurements were subject to systematic errors of 10-15% due to uncertainties in the counter locations. The main function of the luminosity

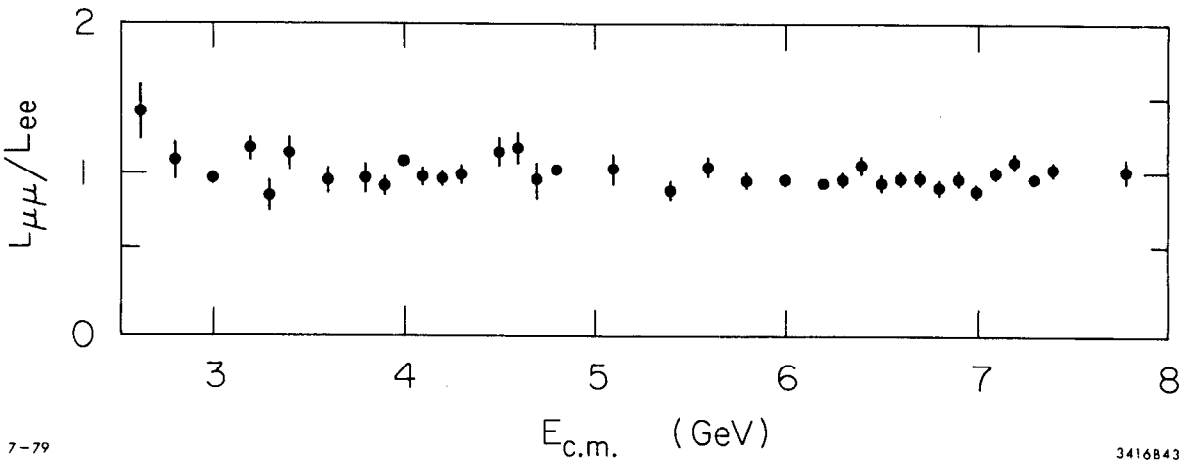

Fig. 12. Ratio of the time integrated luminosity measured by μμ events ($L_{\mu\mu}$) to the time integrated luminosity measured by Bhabha events (L_{ee}) versus center-of-mass energy.

monitor was to provide a continuous on-line relative normalization for evaluating the performance of the apparatus and storage ring.[27]

Bhabha events were chosen to set the normalization because their measurement has the smallest systematic and statistical errors of the three methods of luminosity measurement. The systematic error on the Bhabha integrated luminosity measurement is estimated to be ±6%, dominated by uncertainties in the trigger efficiency and event selection procedures.

D. Raw Yields

Characteristics of the observed events as reconstructed are essential guides in constructing models for Monte Carlo calculation of detector response. Figures 13 and 14 give for a random sample of hadronic events the observed number of hadronic tracks as a function of ϕ and $\cos\theta$ and demonstrate the 2π angular acceptance in ϕ and 0.65 acceptance in $|\cos\theta|$. No cut in $\cos\theta$ has been applied since the $\cos\theta$ distribution for detected events is fit very well by the Monte Carlo simulation of the detector after the trigger inefficiencies have been taken into account. Figure 15 gives the observed charged multiplicity distributions at several energies. The mean charged multiplicity in Figure 16 increases with energy consistent with logarithmic dependence on s, the square of the center-of-mass energy. Figure 17 shows the mean charged particle momentum and mean observed

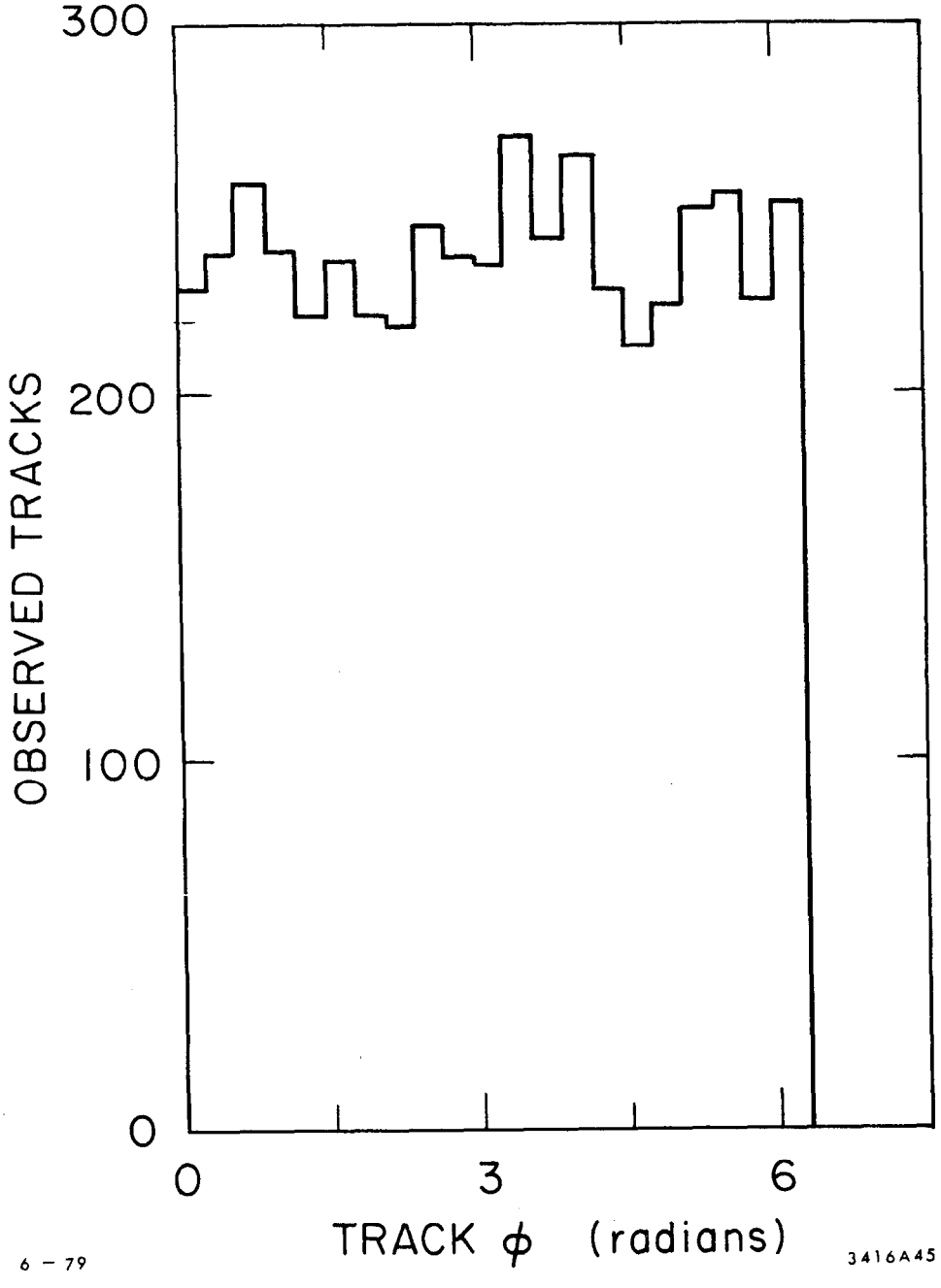

Fig. 13. Observed number of hadronic tracks versus track ϕ.

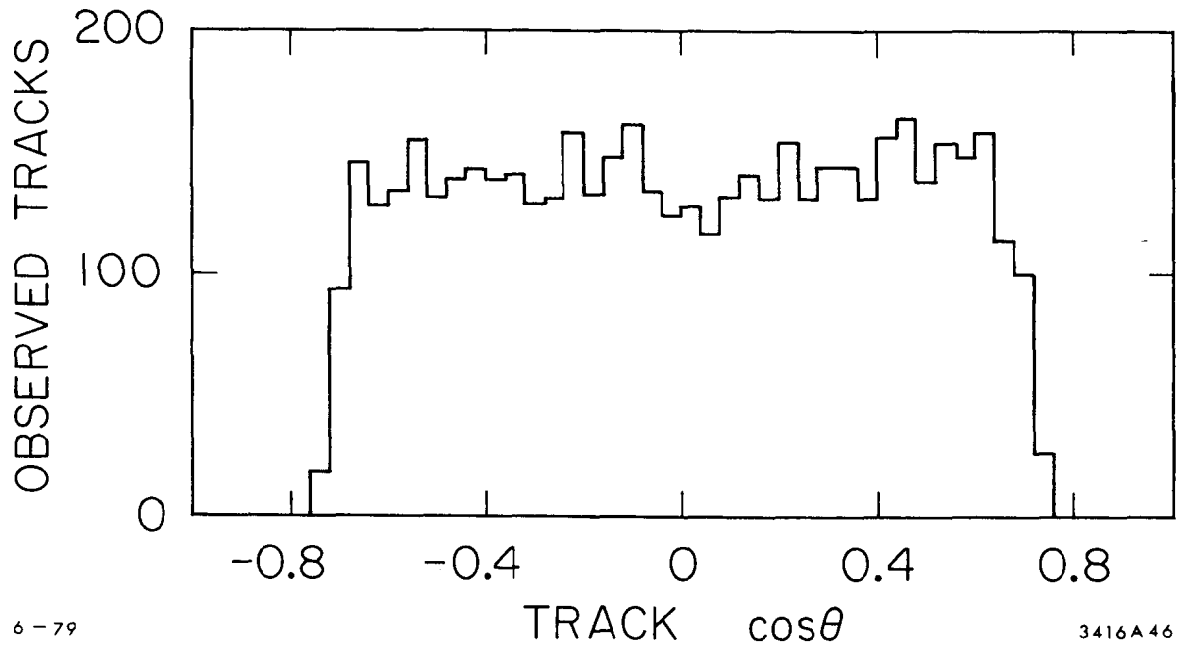

Fig. 14. Observed number of hadronic tracks versus track cos(θ).

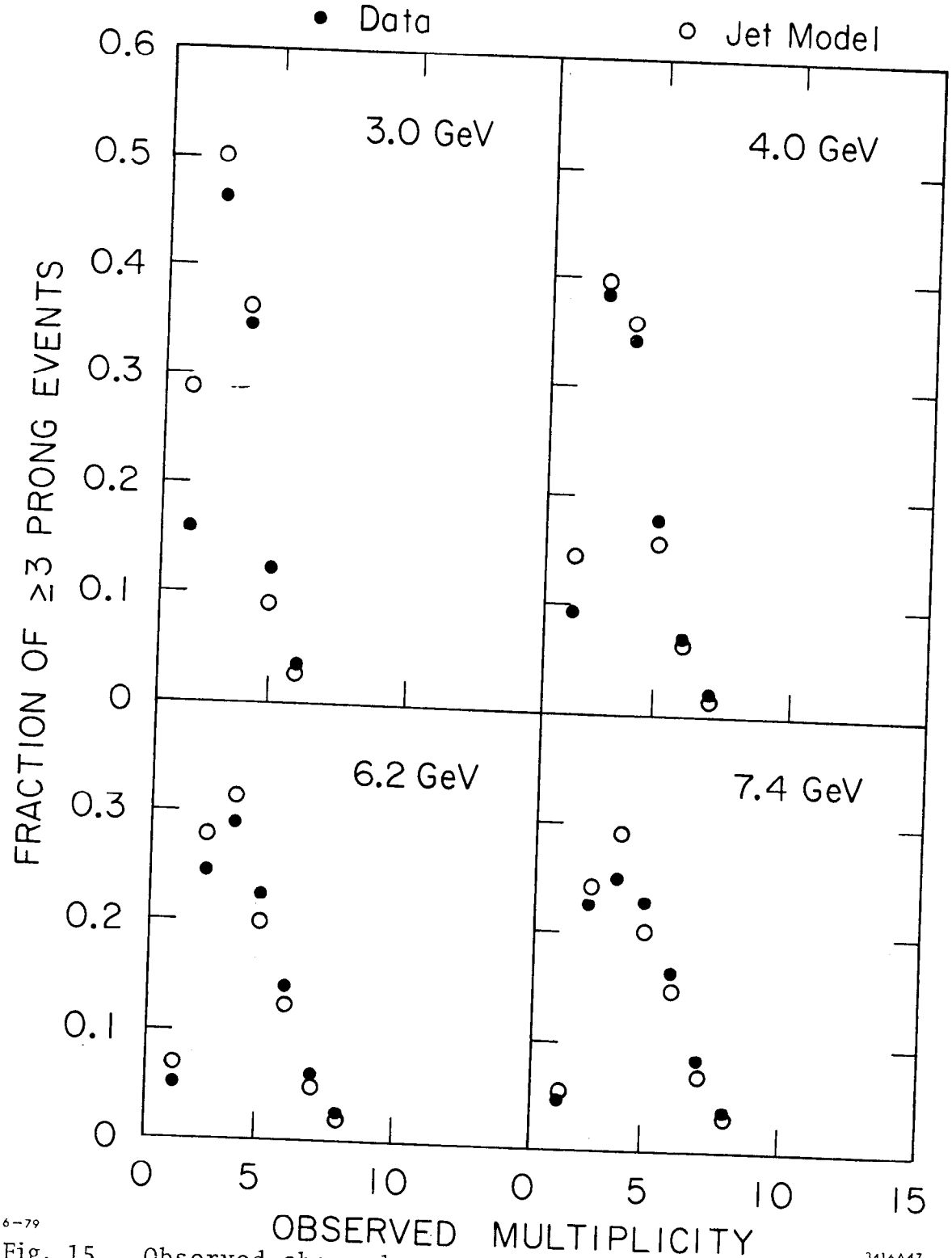

6-79

Fig. 15. Observed charged multiplicity fractions for hadronic events, with all backgrounds removed, normalized to the number of >2 prong events. The open circles are the jet model predictions.

3416A47

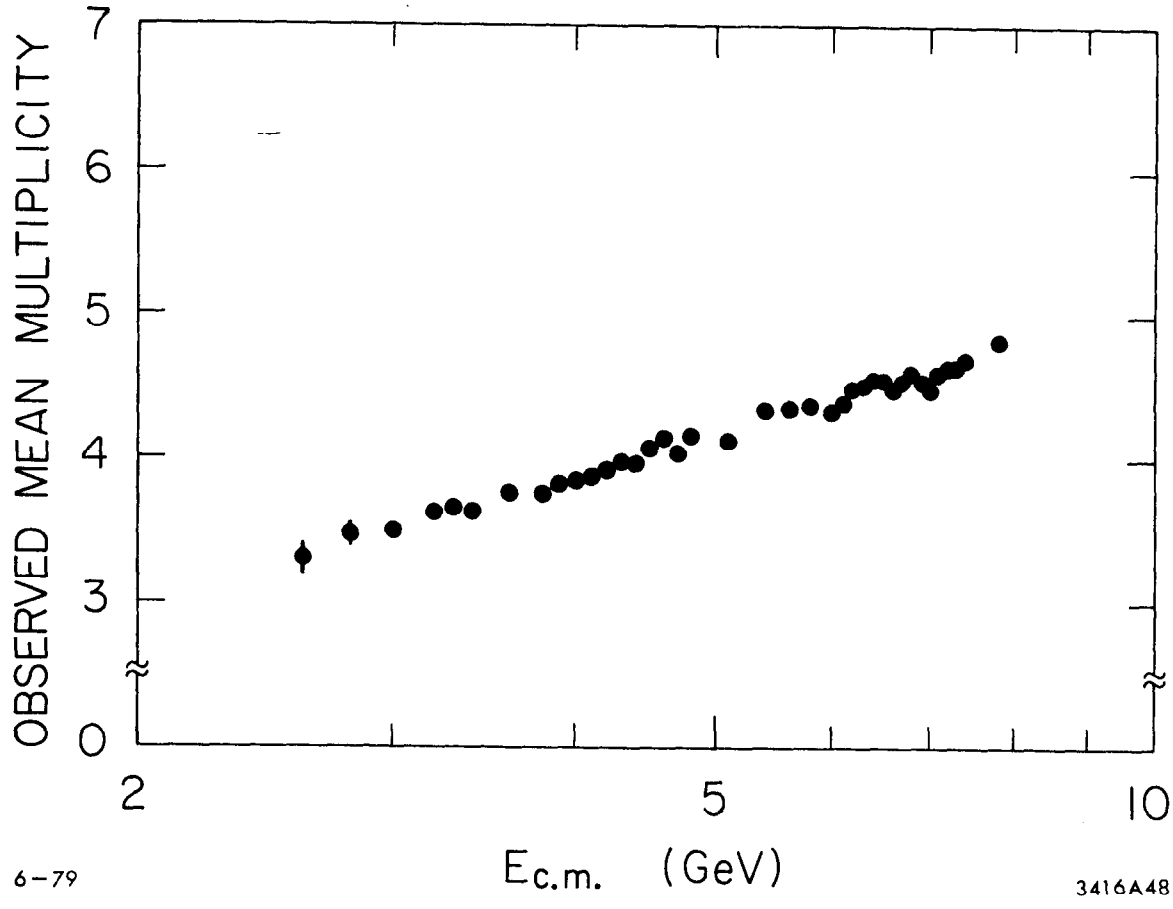

Fig. 16. Observed mean charged multiplicity for hadronic events versus center-of-mass energy.

charged energy fraction vs. E_{cm}. The general energy dependence of these parameters persists after correction for detector inefficiency.

Figure 18 displays the raw yields of muon pair and hadronic events relative to the Bhabha yield. The data indicate a dramatic increase in the hadron yield at $E_{cm} \simeq 4$ GeV. Figure 19 gives the observed differential cross section $s\frac{d\sigma}{dx}$ vs. x for hadronic events with three or more charged prongs. ($x = 2p/\sqrt{s}$, this choice of scaling variable is motivated by the fact that we measure the total particle momentum, p, but not the particle energy.) Some of the variation of the total hadronic yield with center-of-mass energy and of the inclusive single particle yield with track momentum is due to the dependence of the detection efficiency on the total center-of-mass energy and individual particle momenta.

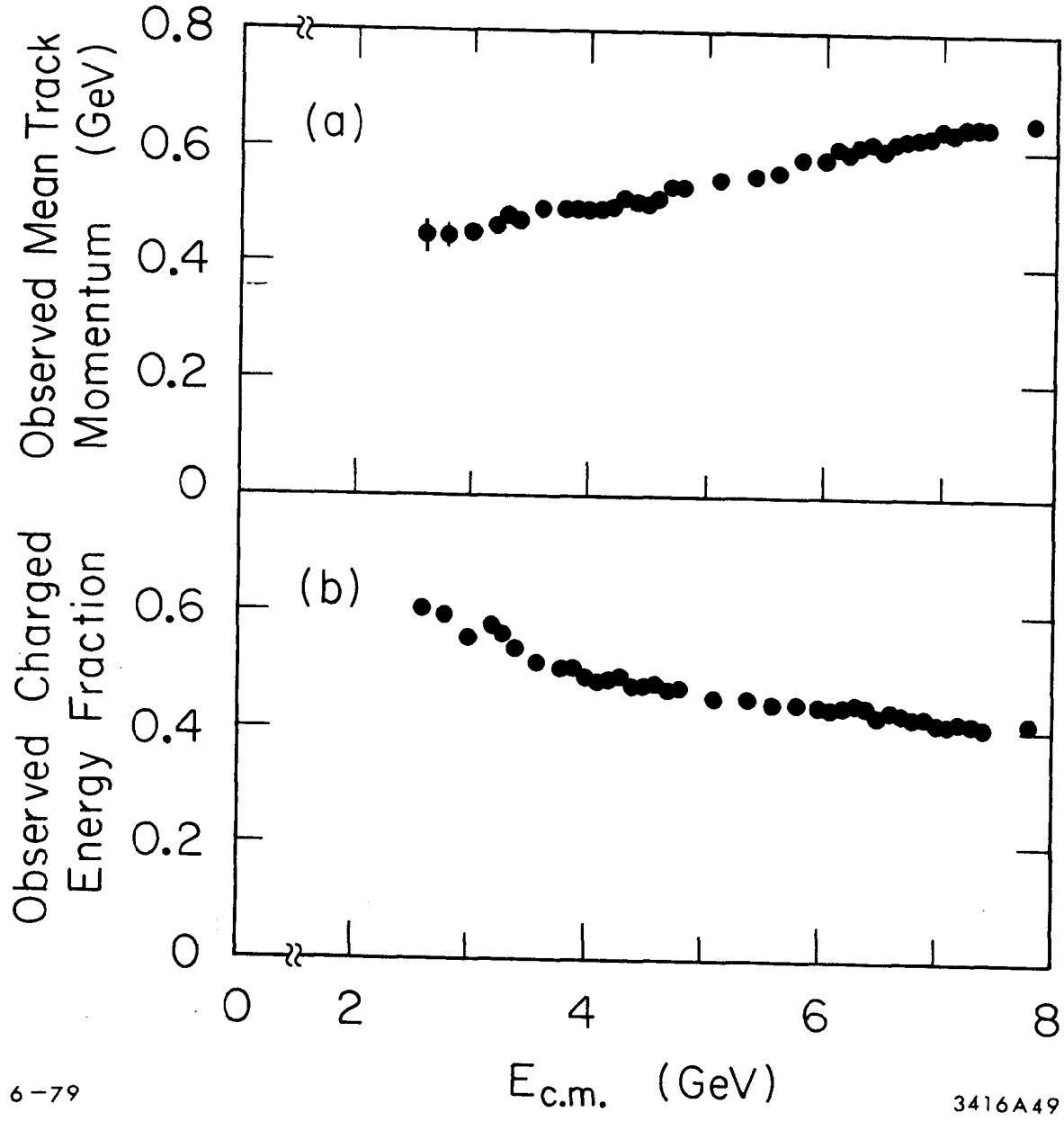

Fig. 17. a) Observed mean charged particle momentum versus center-of-mass energy for hadronic events with three or more charged particles detected.
b) Observed charged energy fraction (ratio of the mean total charged track energy to center-of-mass energy) versus center-of-mass energy. Pion masses are assumed for all tracks.

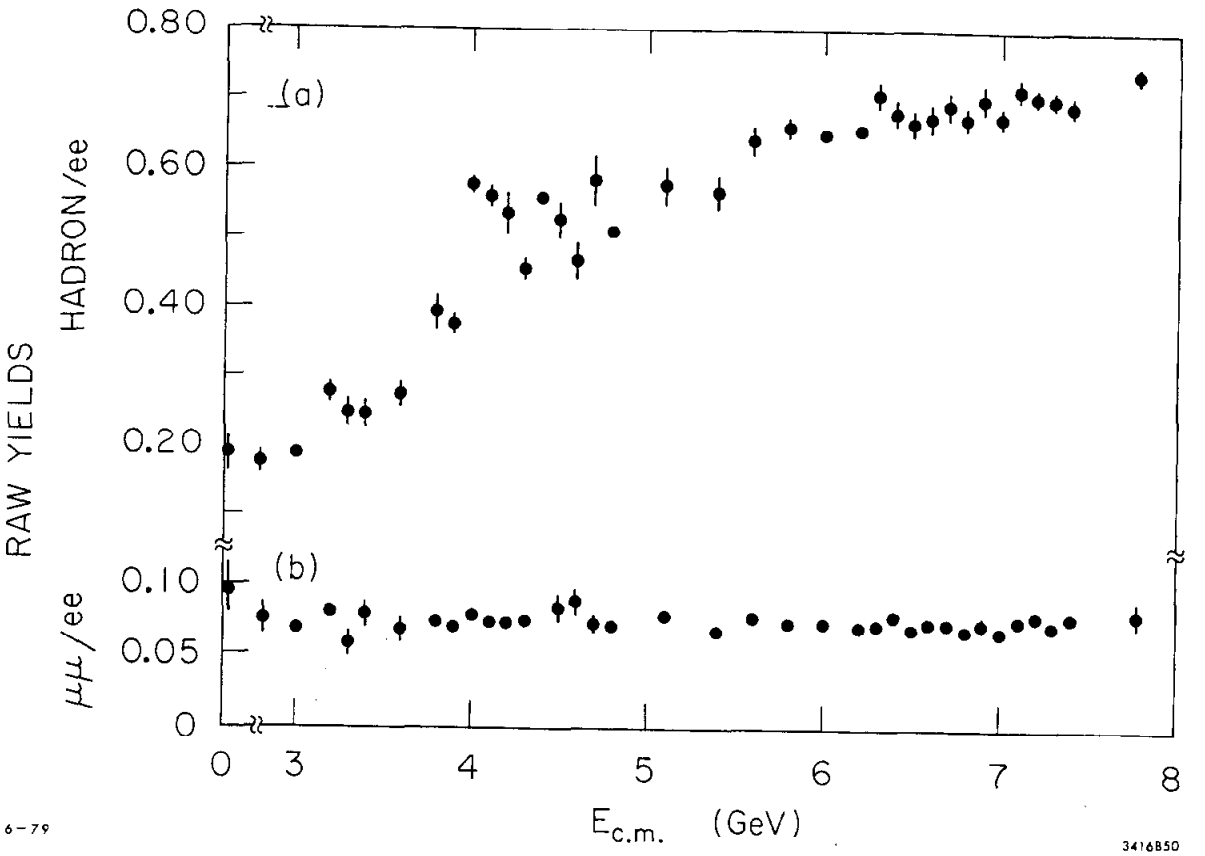

Fig. 18. a) Ratio of the number of detected hadron events to the number of detected Bhabha events versus E_{cm}.
b) Ratio of the number of detected muon pair events to the number of detected Bhabha events versus E_{cm}.

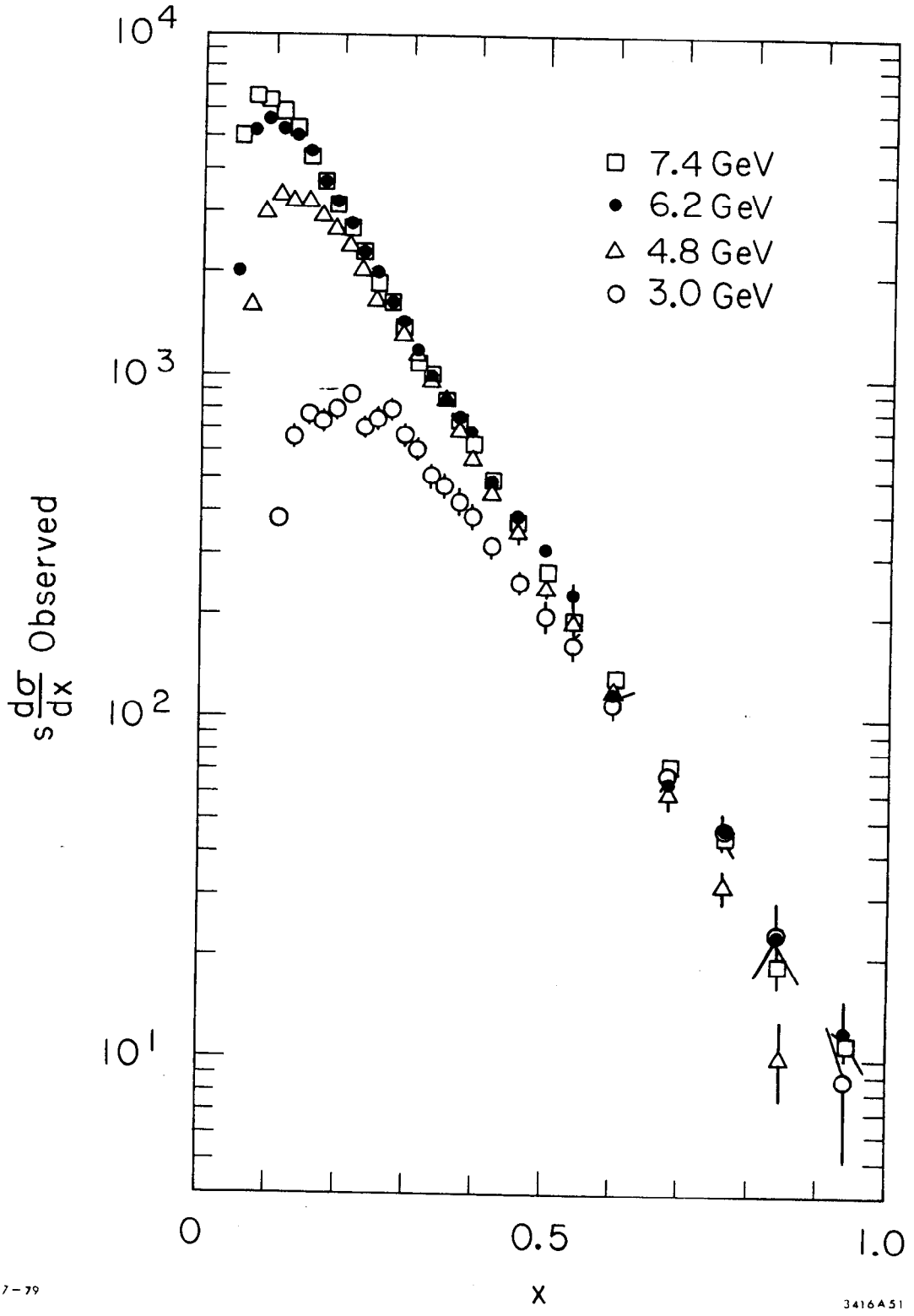

Fig. 19. Observed single particle inclusive x distribution for events with 3 or more detected charged particles versus $x = 2p/E_{cm}$.

IV. DETECTOR EFFICIENCY

A. The Unfold Method

The average hadronic detection efficiency (the probability that a produced event is observed) is a calculated quantity whose value depends on details of the apparatus and of the mechanism of particle production, the latter an unfortunate consequence of incomplete solid angle acceptance and a triggering scheme that fails to trigger on all hadronic events. Uncertain knowledge of the detection efficiency is the main contributor to systematic uncertainties in the determination of the total cross section. The average detection efficiency depends sensitively on the charged multiplicity distribution. The dependence on the production mechanism is reduced by using the detected multiplicity distributions from the data in the calculation of the average detection efficiency. Radiative corrections are included in the calculation because they are different for each multiplicity and so that we can directly relate observed cross sections to the cross section for hadron production from the isolated one photon exchange process.

The "unfold" method, a two step procedure, was used to deduce the number of events produced from the number of observed signal events. First, events were generated by a Monte Carlo calculation according to a specific production model. Parameters in the model were adjusted to make means of detected distributions in various quantities (multiplicity,

momentum,...) agree with the data. This first step was used only to determine a set of quantities ε_{qp}, the probabilities that a non-radiative produced event with p charged prongs will be detected with q charged prongs, by counting the fraction of generated events that should be detected. Then, using the number of signal plus background events in the data with q prongs detected, N_q, the q equations

$$N_q = NB_q + \sum_{p=2} \varepsilon_{qp} \tilde{N}_p \qquad (4.1)$$

are "unfolded" to determine $\tilde{N}_p$, the number of nonradiative events produced with p charged prongs. In equation 4.1, NB_q is the observed number of background events.

B. Monte Carlo Simulation

To calculate the ε_{qp}, events were generated from vertices distributed in z with a Gaussian variance equal to the observed variance (Figure 10). Neutral pions, etas, and kaons decayed according to their known decay modes. The produced particles were followed through all components of the detector. Photons from hadron decays were converted to e^+e^- pairs in the beam pipe, pipe counter, and proportional chambers according to an energy-dependent conversion probability. When particles traversed the region of a pipe, trigger, or shower counter, hits occurred with probability set by the measured pipe counter and TASH efficiencies.

Such hits were tallied to determine whether the event triggered the detector. Charged particles that passed through at least 3 of the 4 sets of spark chambers and that had momentum component transverse to the beam direction of at least 150 MeV were retained. The momenta and directions of the particles were changed from their generated values by using Gaussian resolution functions based on the measured resolutions. Events satisfying the trigger requirements were then analyzed with the same procedures as used for the actual data analysis.

The Monte Carlo simulation included a number of models of the production mechanism. Events were generated according to either Lorentz-invariant phase space or a limited transverse momentum jet model in which phase space is multiplied by a matrix element squared of the form

$$M^2 = e^{-(\sum_i p^i{}_\perp{}^2)/2b^2}$$

where $p^i_\perp$ is the momentum of the i^{th} particle perpendicular to the jet axis. The sum runs over all produced particles. The jet axis angular distribution is of the form

$$\frac{d\sigma}{d\Omega} \propto 1 + \alpha\cos^2\theta.$$

Only events containing charged and neutral pions were

produced, although some checks have been performed using models that included etas, kaons, and nucleons. The charged and neutral pion multiplicities were specified by separate Poisson distributions.

At selected energies, the production model parameters were determined by comparison with the data. The mean total multiplicity and ratio of numbers of charged to neutral pions were determined by requiring that the model yield the observed charged particle mean momentum and mean multiplicity for events in which three or more charged particles were detected. Figure 15 shows a comparison of calculated detected charged particle multiplicity distributions in the jet model and of the data at several energies.

The observed single particle inclusive x distribution for events with three or more detected charged particles along with the phase space and jet model predictions are shown in Figure 20. The jet model is in much better accord with the observations and, henceforth, is used to model the production mechanism. The parameter b was determined to be 300 MeV by fitting to the observed mean momentum transverse to the observed jet axis. We used $\alpha = 1$ in the jet axis angular distribution in agreement with the measured value $\alpha = 0.97 \pm 0.14$ previously reported.[28] Details of the jet analyses are presented in Reference 28.

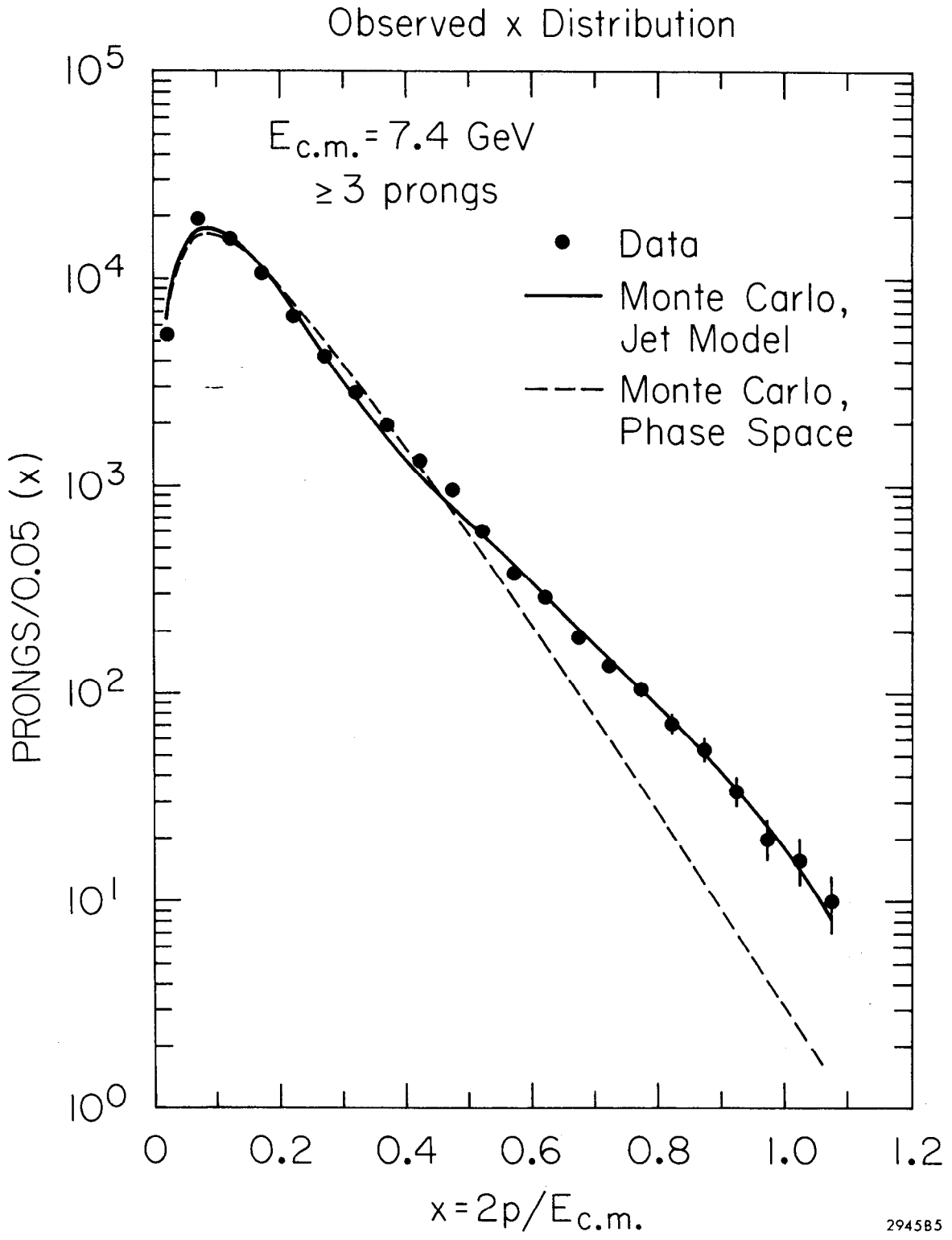

Fig. 20. Observed single particle x distribution for events with three or more detected charged particles for E_{cm} = 7.4 GeV along with the phase space and jet model predictions.

C. Radiative Corrections

The starting point in the evaluation of the corrections to the detector efficiency for initial state radiation is the third order expression of Bonneau and Martin,[29]

$$\sigma(4E^2) = \sigma_o(4E^2) \left[1 + \delta_1 + t \int_{\Delta}^{E} \frac{dk}{k} \left(1 - \frac{k}{E} + \frac{k^2}{2E^2} \right) \frac{\sigma_o(4E(E-k))}{\sigma_o(4E^2)} \right] . \tag{4.2}$$

that relates the production cross section at $s = 4E^2$ to the cross section σ_o for the isolated one photon exchange process. The term

$$\delta_1 = \frac{2\alpha}{\pi} \left(\frac{\pi^2}{6} - \frac{17}{36} \right) + t \left(\frac{13}{12} + \text{Ln} \frac{\Delta}{E} \right) \quad \text{with}$$

$$t = \frac{2\alpha}{\pi} \left(2 \, \text{Ln} \left(\frac{2E}{m_e} \right) - 1 \right)$$

includes contributions from renormalization graphs and soft photon emission. The integral in Equation 4.2 is the correction for undetected hard photons, of energy greater than the cut-off Δ, emitted in the initial state at $s = 4E^2$. Analogous expressions may be written for the inclusive differential cross section. No corrections are applied for radiation in the final state.

The energy distribution of radiated photon momenta is given by Equation 4.2. In order to incorporate the content

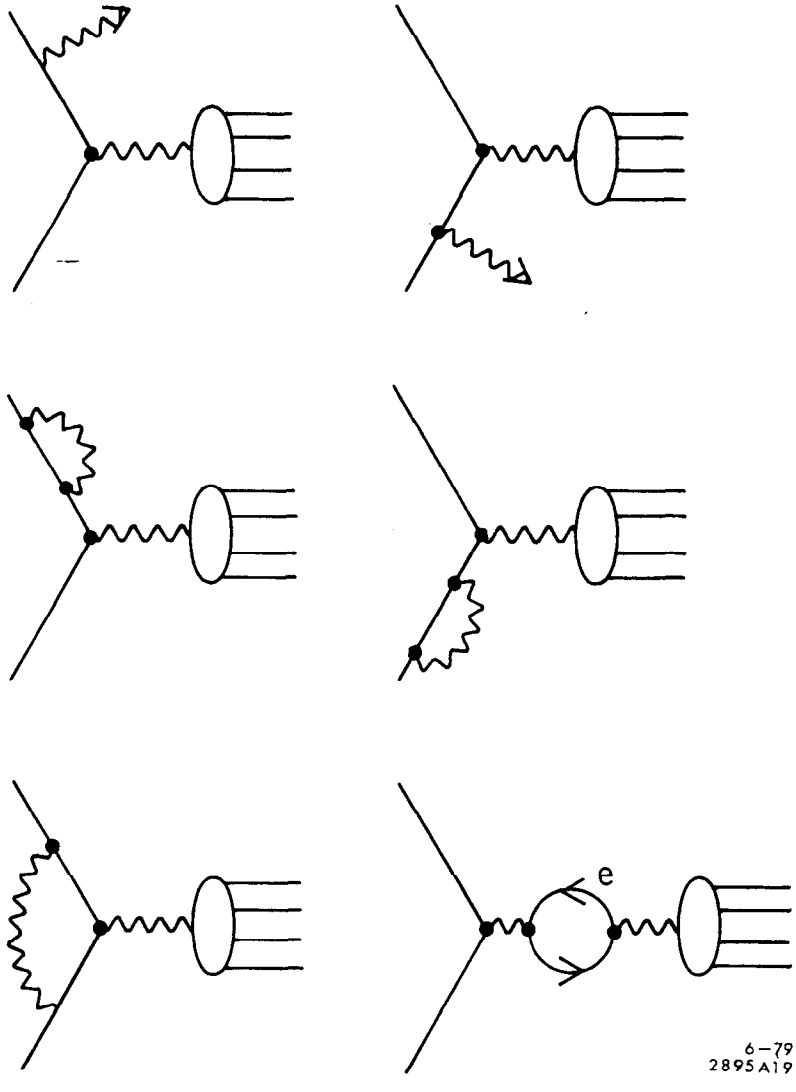

Fig. 21. Diagrams included in the radiative correction for $\sigma(e^+e^- \to \text{hadrons})$.

of Equation 4.2 into the Monte Carlo calculations of the matrix elements ε_{qp}, hadronic events at each interaction energy were generated with the jet model described above, using parameters appropriate to the radiated center-of-mass energy, and with radiated photon momenta only in the direction of the incident radiating particles. Note from Equation 4.2 that the number of produced events that do not radiate a hard photon is proportional to $\sigma_o(1+\delta_1)$. Each efficiency matrix element, ε_{qp}, is equal to the ratio of the detected partial cross section to the produced partial cross section σ_o^p. This ratio equals the ratio of the number of detected events, whether produced from events with hard photon emission or not, to the number of events produced without hard photon emission, all multiplied by $1+\delta_1$, i.e.,

$$\varepsilon_{qp} = \frac{\text{Number of events detected of mult. q from prod. mult. p}}{\text{Number of prod. events of mult. p with no hard } \gamma/(1+\delta_1)} \tag{4.3}$$

An analogous expression may be written for the inclusive detection efficiency $\varepsilon(x)$.

In principle, the integral Equation 4.2 should be iterated, using first the measured values of the cross section for σ_o in the integral, determining the efficiencies which yield a new produced cross section, putting that cross section back into the Monte Carlo calculation, etc., until

the process converges. In practice, since measurements are subject to systematic fluctuations and uncertainties, we have put as little structure as possible into the assumed σ_o consistent with our data. In this way, we hope to avoid "creating" peaks in the total cross section from mere statistical or systematic fluctuations, but may underestimate structure that is actually there.

In order to find structure indicated by the data, we first used the fitted jet model parameters to make a Monte Carlo generation of events at several beam energies with no radiation, and calculated a first approximation to the detection efficiency, the fraction of generated events that satisfy the selection criteria in the detector. Figure 22 shows the observed yield corrected with this efficiency determined without radiative correction and divided by the muon pair production cross section in the region 3.5-4.5 GeV. Indications of structure are seen near 3.77, 4.1 and 4.4 GeV. For these results, we have used for σ_o the smoothed representation of our previous results[30,31] and those of reference 32 shown in Figure 23.

There are two effects of the radiation process that must be evaluated in calculating the matrix elements ε_{qp}: 1) the center-of-mass energy of the hadronic states that are generated must conform to that contained in Equation 4.2 using the σ_o of Figure 23, and 2) we must evaluate the

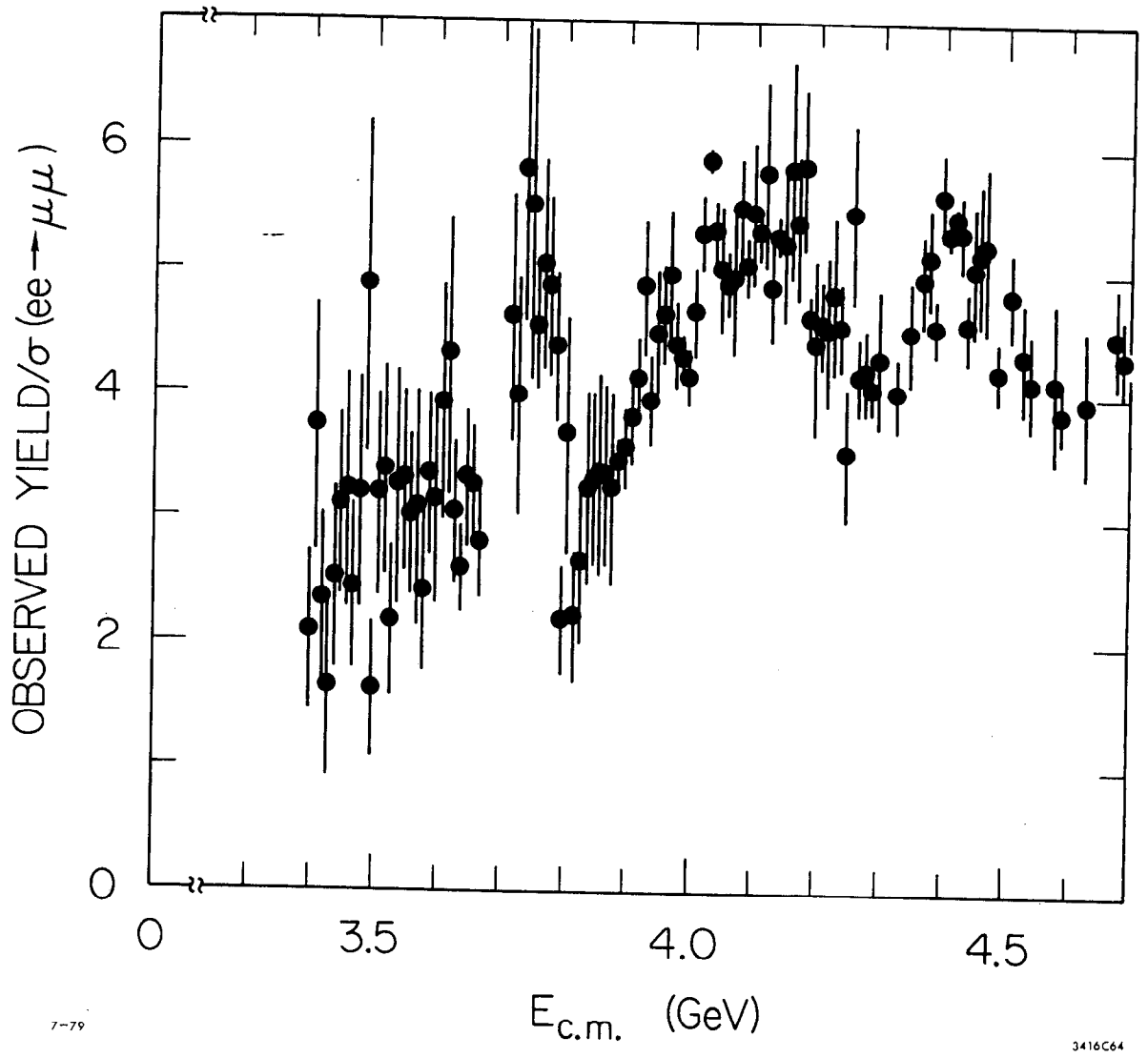

Fig. 22. Observed yield corrected with jet model efficiency determined without radiative corrections and divided by the muon pair production cross section versus E_{cm}.

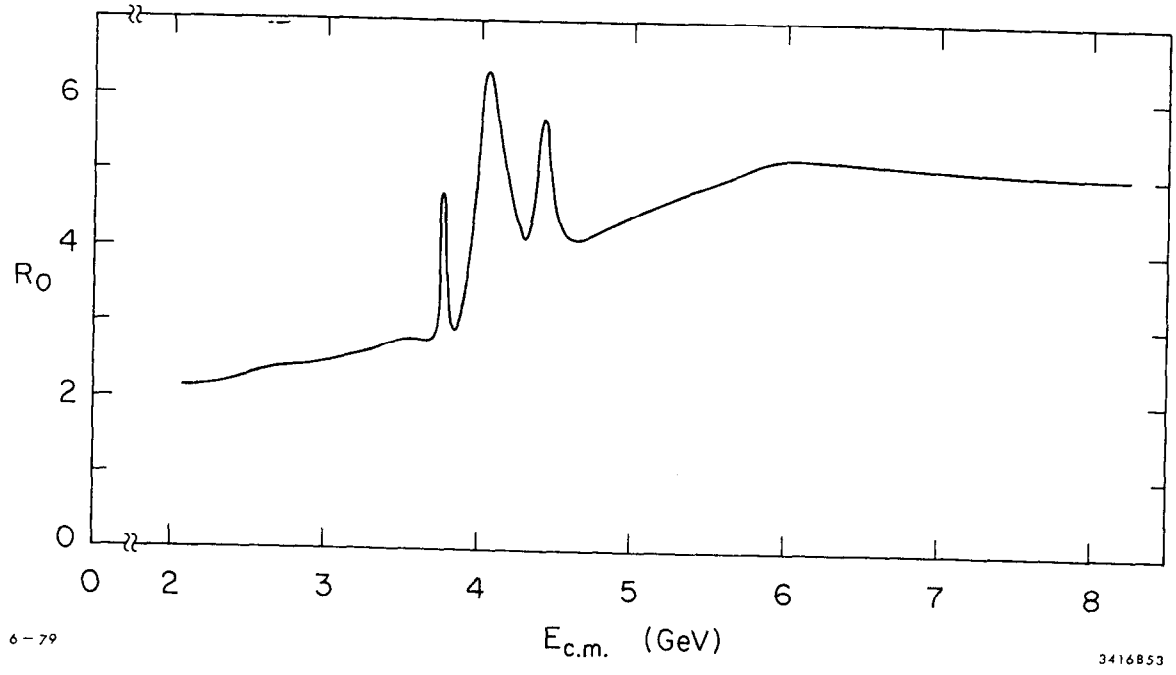

Fig. 23. Smoothed representation of R values versus E_{cm} used for $\sigma_0(s)$ in calculating the integral of Equation 4.2.

fraction of generated events that are produced with no radiation. Both are multiplicity dependent effects because the mean multiplicity is energy dependent. We define a factor

$$\Omega_p = \frac{\text{(total number of prod. events of mult. p) } (1+\delta)}{\text{Number of produced events of mult. p with no hard photon}} \qquad (4.4)$$

This factor, which is independent of the properties of the detector, was calculated in a series of Monte Carlo runs using for the mean multiplicity those values determined by fitting the jet model to the data. The Ω_p so determined have an energy dependence that varies rapidly in the region of structure in σ_o. We factor each Ω_p into a factor $\tilde{\Omega}_p$ that varies slowly with energy and a factor ω, common to all multiplicities, that reflects the structure in σ_o.

$$\Omega_p = \omega\tilde{\Omega}_p \ . \qquad (4.5)$$

The $\tilde{\Omega}_p$ were determined by a fit[33] to each Ω_p in an energy interval distant from sharp structure and these fits adjusted so that Equation 4.5 is satisfied for a common multiplicity independent ω. This factorization is possible to the extent that changes in the produced multiplicity distribution are small over the energy region of the sharp structure in σ_o. The results of these calculations are displayed in Figures 24 and 25.

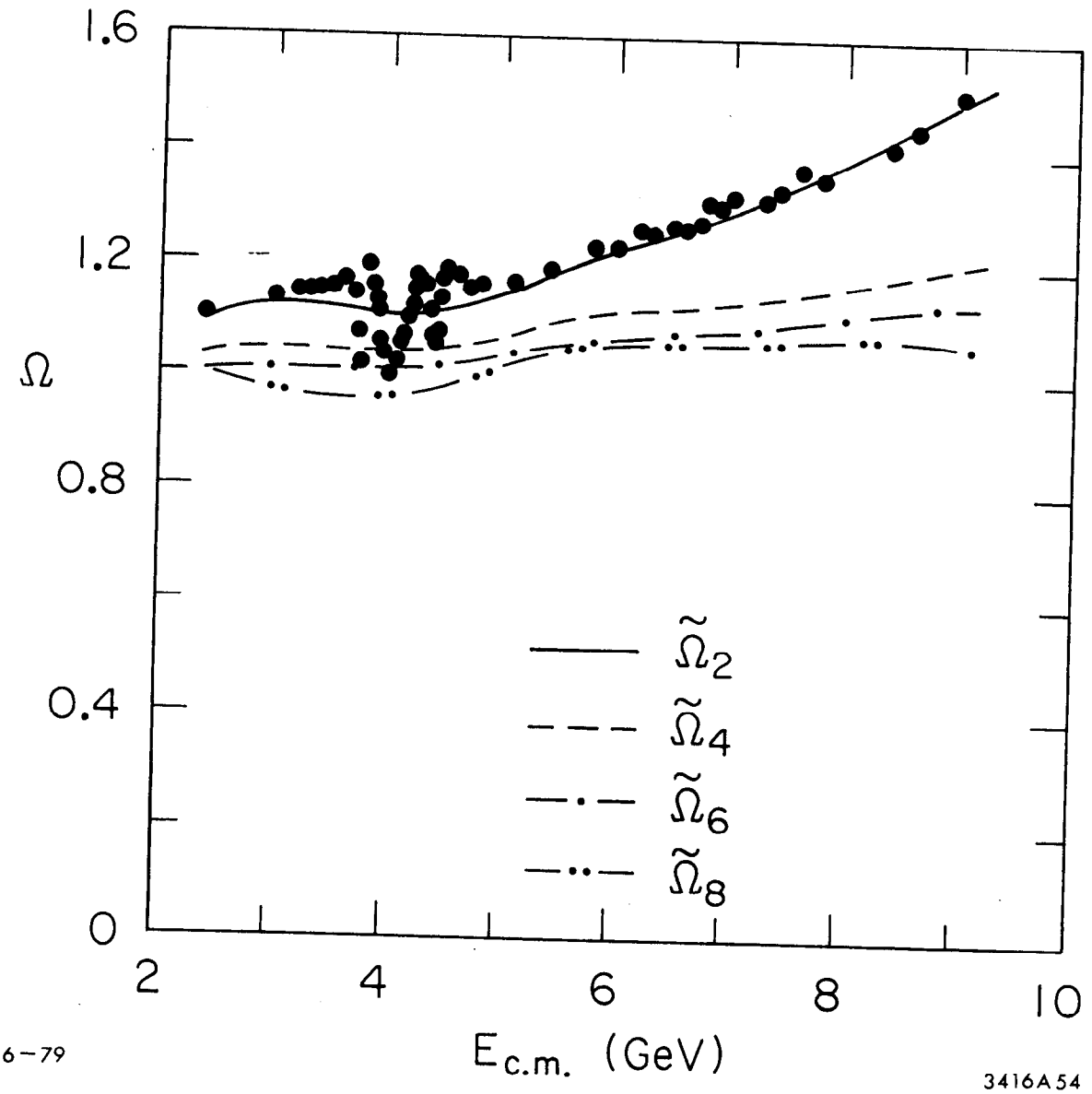

Fig. 24. The points are the Monte Carlo results for Ω_2 (Equation 4.4) versus E_{cm}. The curves are the factors $\tilde{\Omega}_2 \rightarrow \tilde{\Omega}_8$ (Equation 4.5) versus E_{cm}. The structure shown in Ω_2 is a reflection of the structure assumed for $\sigma_o(s)$ (Figure 21).

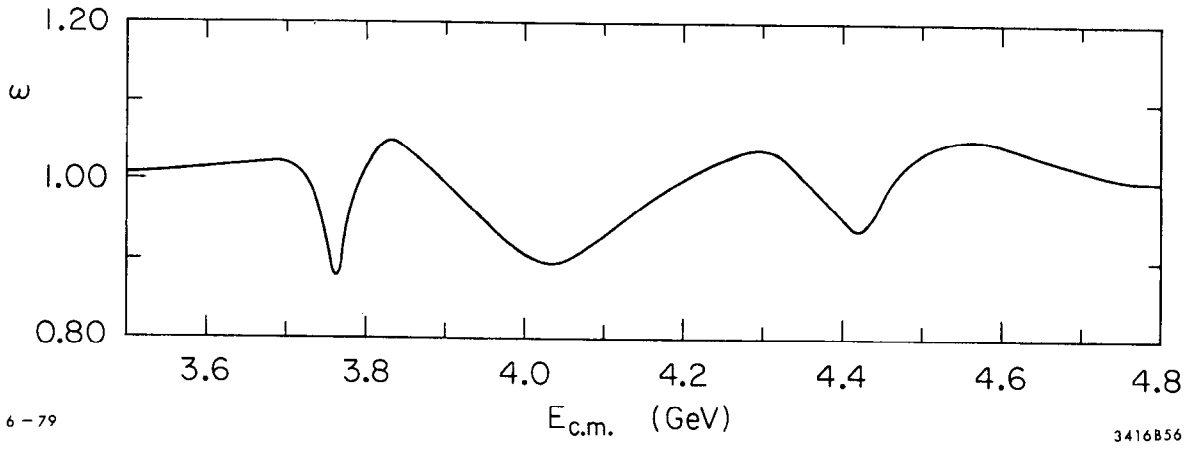

Fig. 25. ω (Equation 4.5) versus E_{cm}.

We include the properties of the detector in the detection efficiency by calculating the elements $\tilde{\varepsilon}_{qp}$ defined as the ratios of the number of events detected with multiplicity q which are produced from events of multiplicity p to the total number of events produced with multiplicity p. The factors $\tilde{\varepsilon}_{qp}$ contain the effects of the detector geometry, hardware efficiency, trigger criteria and event selection criteria. The Monte Carlo has been run at a set of energies across the range of the data, and smooth curves fit[33] through the Monte Carlo results for each of the matrix elements $\tilde{\varepsilon}_{qp}$. Figure 26 shows, for example, the elements $\tilde{\varepsilon}_{02} \rightarrow \tilde{\varepsilon}_{08}$ *vs.* energy along with the interpolation curves for the Monte Carlo results. The interpolation of the Monte Carlo results was accomplished with a spline fitting technique.[33]

We now have all the factors necessary to evaluate the ratio of the total number of events detected with q prongs to the number of events produced with p prongs by the isolated one photon exchange process:

$$\varepsilon_{qp} = \tilde{\varepsilon}_{qp} \, \tilde{\Omega}_p \, \omega \qquad (4.6)$$

This calculated matrix relates the observed multiplicity distribution to that produced by σ_o. As we are now able to deduce the produced multiplicity, the method is less dependent on any particular model of the multiplicity. The

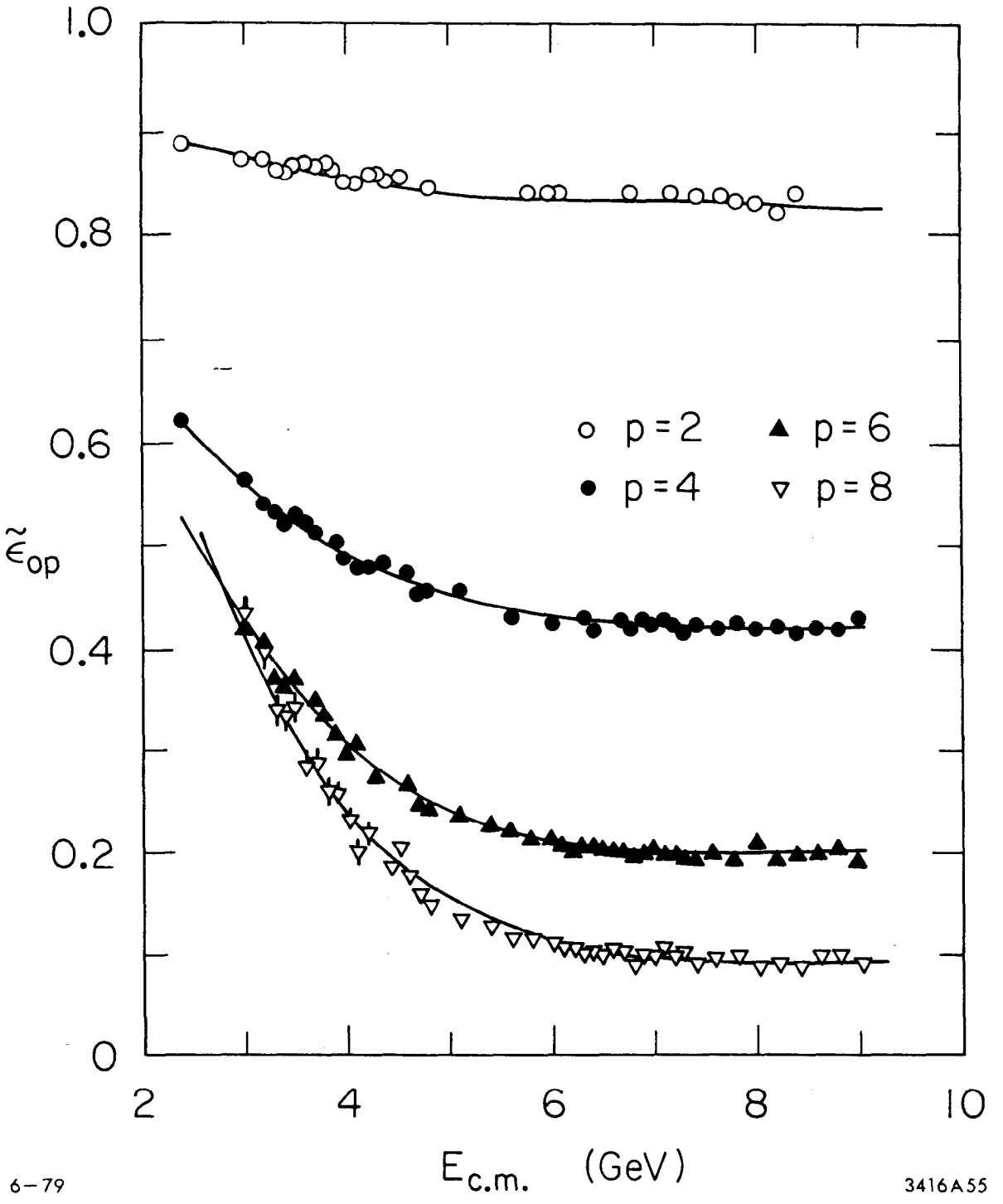

Fig. 26. Detection efficiency matrix elements $\tilde{\epsilon}_{02} \rightarrow \tilde{\epsilon}_{08}$ versus E_{cm}. These elements are the probabilities of completely missing a 2, 4, 6, or 8 produced charged prong event, respectively. They are defined by $\tilde{\epsilon}_{op} = 1 - \Sigma_i \tilde{\epsilon}_{ip}$. The large value ($\sim$20%) at high energy of the elements $\tilde{\epsilon}_{06}$, $\tilde{\epsilon}_{08}$ is caused mainly by the effect of the TASH triggering requirement. See Appendix I.

factor ω is common to all channels and cannot affect the results for the distribution in multiplicity; thus, for these purposes, we temporarily ignore ω and relate the observed and produced multiplicities by Equation 4.1:

$$N_q = NB_q + \sum_{p=2}^{\infty} \tilde{\varepsilon}_{qp} \quad \tilde{\Omega}_p \quad \tilde{N}_p \tag{4.7}$$

where N_q is the observed number of signal plus background events of q prongs. Equation 4.7 is "unfolded" by a maximum likelihood method to find $\tilde{N}_p$, the number of events produced with p charged prongs. In order to unfold Equation 4.7, the log-likelihood is maximized. The likelihood function is a product of Poisson distribution functions over the detected charged particle multiplicity bins and is given by

$$\mathscr{L} = \prod_q \frac{\mu_q^{N_q}}{N_q!} e^{-\mu_q}$$

where μ_q is the predicted number of signal plus background events of detected multiplicity q. From these results, we can define an average detection efficiency which would be valid if there were no fine structure in σ_o.

$$\bar{\varepsilon} = \frac{\sum_q (N_q - NB_q)}{\sum_p \tilde{N}_p} \tag{4.8}$$

Figure 27 shows $\bar{\varepsilon}$ values determined from the unfolds of a restricted sample of the data. As the energy increases, the detection efficiency gradually rises. This rise is caused by the slowly rising mean charged particle multiplicity and the diminished effect of the TASH requirement with the increasing mean track momentum. The smooth curve of Figure 27 was used to interpolate $\bar{\varepsilon}$. The product of factors $\bar{\varepsilon}\omega$ yields the true average detection efficiency, with full account taken of the radiative effects implied by Figure 23.

For reasons of computational economy, the radiative tails of the $\Psi(3095)$ and $\Psi'(3684)$ were not included in the foregoing analysis. (They would have appeared as very large variations in the ω parameter at energies close to these states.) Rather, they were subtracted from the corrected measured cross section according to the relation.[34]

$$\sigma_{\text{tail}}(E) = \sum_{\Psi,\Psi'} \frac{6\pi^2\Gamma_{ee}}{M^2} (t/k)\ (k/E)^t\left(1-k/E+\frac{k^2}{2E^2}\right)\ \Phi$$

where Γ_{ee} is the leptonic width of the resonance[35] (Ψ or Ψ'), $k = E - (M^2/4E)$, and Φ is the multiplicative correction to the detection efficiency due to the center-of-mass motion. The factor Φ is determined by Monte Carlo calculation, and the tail subtraction is computed analytically. Φ ranges from 0.5 in the region far above the resonance ($\sim$ 7 GeV) to 1 near the resonances.

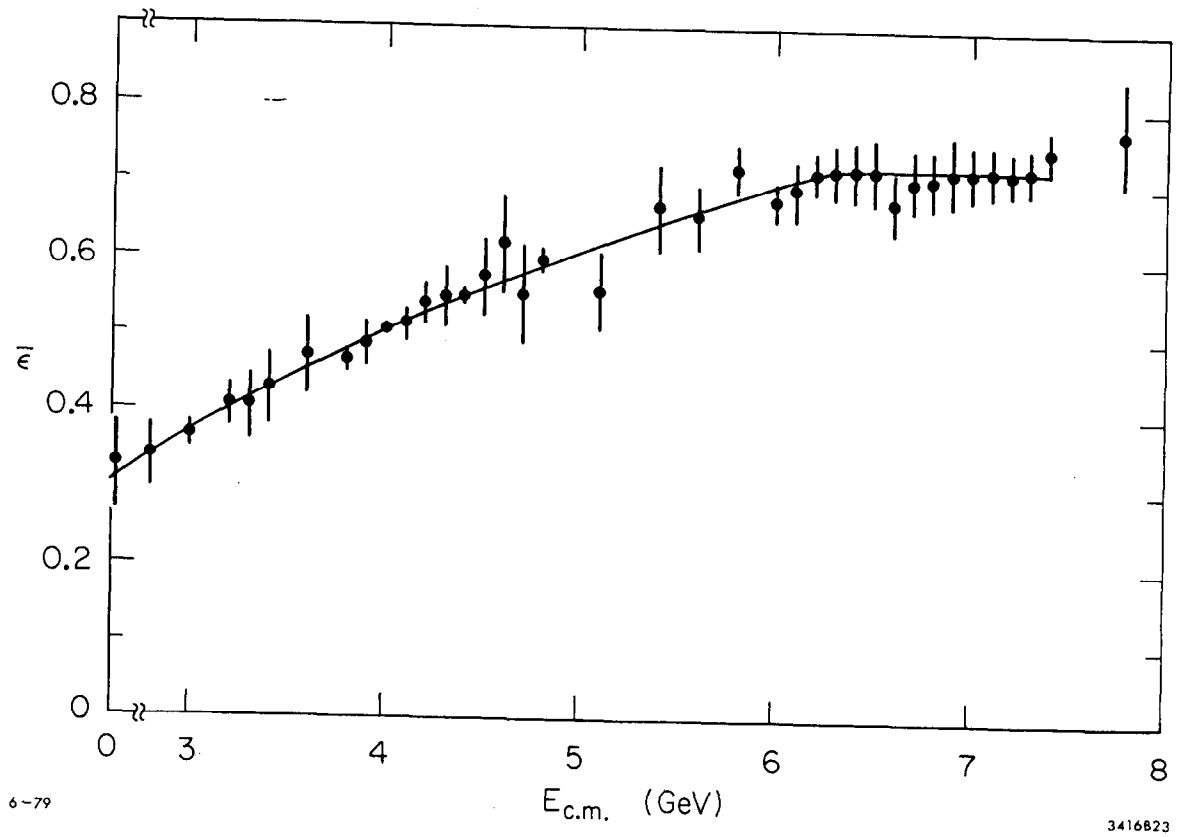

Fig. 27. Effective hadronic detection efficiency $\bar{\epsilon}$ (Equation 4.8) versus E_{cm}. The curve is used for interpolation.

The calculation of the inclusive efficiency $\varepsilon(x)$, which relates the observed x distributions to those produced by the isolated one photon exchange process, utilizes observables to the extent that the mean multiplicity and momentum of the jet model have been adjusted to generate the corresponding observed quantities. Events were generated with an energy spectrum conforming to Equation 4.2 and the efficiency calculated as the fraction of tracks generated by σ_o within a particular x interval that should be observed in the detector in events with at least 3 charged tracks detected. Figure 28 shows the single particle inclusive momentum detection efficiency, $\varepsilon(x)$, vs. x. The low overall value of $\varepsilon(x)$ is caused by the limited acceptance and the TASH trigger requirement. The most important effect causing the negative slope of $\varepsilon(x)$ is the requirement of three or more charged prongs detected in the event in order for tracks to be included in the detected sample. Radiative corrections, electrons from converted gammas and π^o Dalitz decays, momentum dependence in the trigger, and the jet angular distribution are other effects that cause $\varepsilon(x)$ to be higher at low x. The finite momentum resolution tends to favor the high x region over the low x region. All these effects are included in the Monte Carlo calculations of $\varepsilon(x)$, performed at each energy where inclusive momentum spectra were measured.

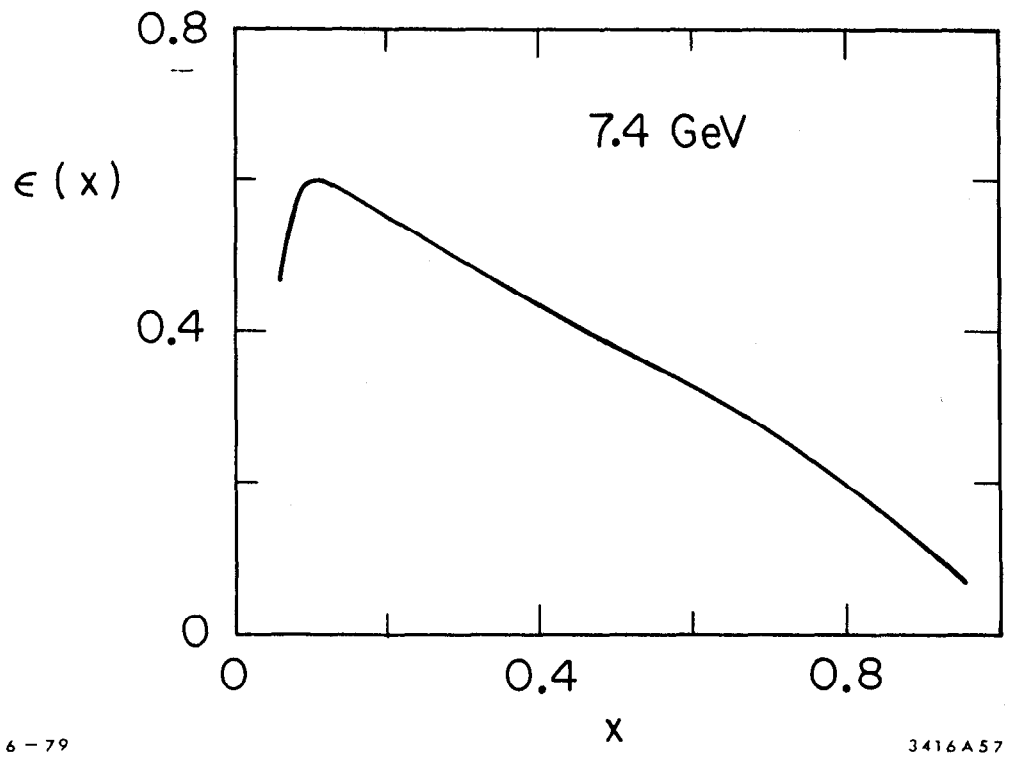

Fig. 28. Single particle inclusive detection efficiency, $\varepsilon(x)$, versus $x = 2P/E_{cm}$ for 7.4 GeV.

The accuracy with which the slope of $\varepsilon(x)$ can be determined dominates the systematic error in the shape of the inclusive momentum spectra. The variation of the individual detection efficiency matrix elements ε_{qp} with the particular production model is as large as ±12%. The variation with the production model of $\bar{\varepsilon}$ determined by the unfold technique is ±8%, about half as large as the variation when $\bar{\varepsilon}$ is determined directly as the fraction of the generated events detected in the Monte Carlo. The variation of $\bar{\varepsilon}$ and $\varepsilon(x)$ with production model was used in estimating the systematic uncertainty in the $\bar{\varepsilon}$ and $\varepsilon(x)$ determinations.

V. MARK I RESULTS

A. Total Annihilation Cross Section

The total annihilation cross section into multihadron final states was computed from

$$\sigma(ee \to \text{hadrons}) = \frac{N\nu}{\bar{\varepsilon} L \omega} - \sigma_{tail} \qquad (5.1)$$

where N is the total number of observed events with backgrounds removed, $\bar{\varepsilon}$ and ω are the efficiency factors described in Section IV, ν is the correction for losses due to the vertex radius cut, L is the time integrated luminosity determined from Bhabha scatter events, and σ_{tail} is the correction for the radiative contributions of the $\psi(3095)$ and $\psi'(3684)$. Figure 29 shows the ratio R of this cross section to the muon pair production cross section calculated in lowest order QED. The errors shown are statistical errors.

There are additional overall and point-to-point systematic uncertainties. At energies >6 GeV, the estimated uncertainty in the detection efficiency (±8%), the luminosity (±6%), the event selection procedures (±2%), and the background subtractions (±3%) yields an overall possible systematic error of ±10%. From study of the dependence of the detection efficiency on the particle production model vs. energy and on the measured curve for the TASH efficiency (Figure 8) we conclude there is a possible additional smooth

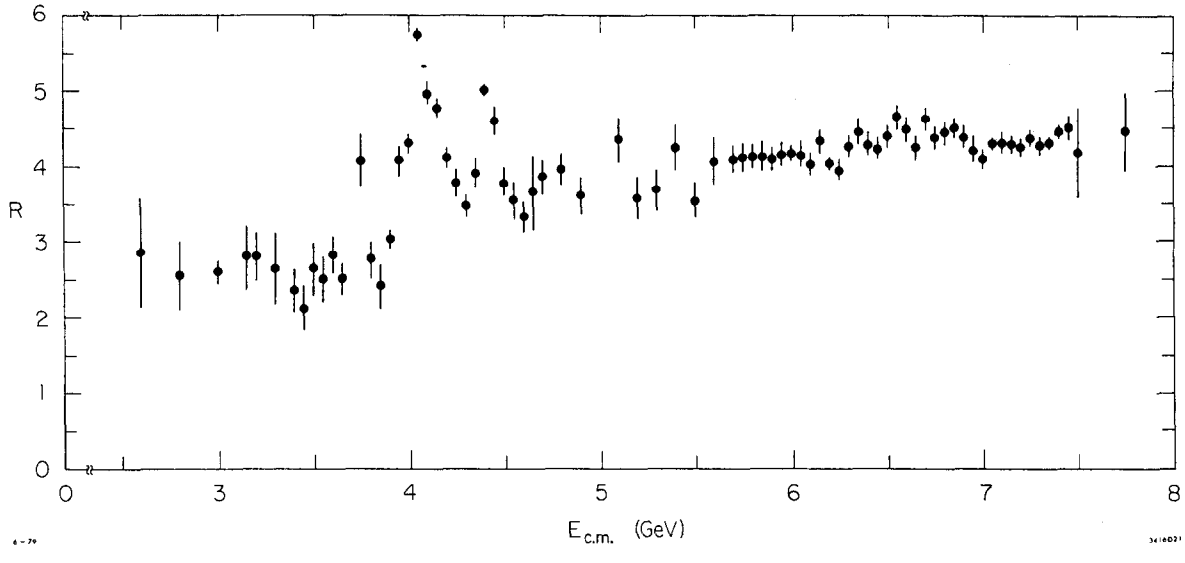

Fig. 29. The ratio $R = \sigma(e^+e^- \rightarrow \text{hadrons}) / \sigma(e^+e^- \rightarrow \mu^+\mu^-)$ versus E_{cm}. Tabulated values are contained in Table 3.

TABLE 3

R VALUES FOR FIGURE 29

E_{cm}	R	+/-
2.60	2.84	0.74
2.80	2.54	0.46
3.00	2.59	0.15
3.15	2.79	0.42
3.20	2.80	0.32
3.30	2.65	0.46
3.40	2.35	0.28
3.45	2.12	0.30
3.50	2.63	0.35
3.55	2.50	0.30
3.60	2.82	0.26
3.65	2.50	0.19
3.75	4.08	0.36
3.80	2.76	0.26
3.85	2.40	0.29
3.90	3.04	0.13
3.95	4.07	0.20
4.00	4.29	0.13
4.05	5.73	0.09
4.10	4.97	0.15
4.15	4.78	0.13
4.20	4.11	0.14
4.25	3.78	0.18
4.30	3.47	0.15
4.35	3.91	0.19
4.40	5.01	0.08
4.45	4.60	0.18
4.50	3.79	0.18
4.55	3.55	0.25
4.60	3.33	0.19
4.65	3.64	0.53
4.70	3.86	0.23
4.80	3.97	0.19
4.90	3.61	0.25
5.10	4.34	0.29
5.20	3.57	0.27
5.30	3.68	0.27
5.40	4.24	0.31
5.50	3.57	0.24
5.60	4.08	0.32
5.70	4.09	0.16
5.75	4.12	0.20
5.80	4.13	0.16
5.85	4.13	0.19
5.90	4.09	0.14
5.95	4.17	0.16
6.00	4.17	0.09
6.05	4.16	0.18
6.10	4.04	0.15
6.15	4.34	0.16
6.20	4.05	0.08
6.25	3.96	0.14
6.30	4.27	0.14
6.35	4.47	0.17
6.40	4.31	0.13
6.45	4.23	0.14
6.50	4.40	0.15
6.55	4.66	0.16
6.60	4.50	0.17
6.65	4.25	0.16
6.70	4.63	0.15
6.75	4.38	0.15
6.80	4.44	0.16
6.85	4.50	0.13
6.90	4.41	0.15
6.95	4.23	0.17
7.00	4.10	0.12
7.05	4.31	0.09
7.10	4.32	0.14
7.15	4.29	0.11
7.20	4.27	0.11
7.25	4.39	0.11
7.30	4.29	0.11
7.35	4.33	0.09
7.40	4.46	0.08
7.45	4.51	0.14
7.50	4.18	0.59
7.80	4.47	0.53

variation of ±10% from the highest energy to the lowest; i.e., the overall systematic error is estimated to be ±20% for E_{cm} = 2.6 GeV varying smoothly down to ±10% for $E_{cm} \geq 6$ GeV. By studying data taken at different times with the same machine energy setting, we estimate the systematic point-to-point fluctuations to be ±3%.

As can be seen from Figure 29, R is approximately constant below 3.1 GeV with the value 2.7±0.5. Above 5.5 GeV, R is again approximately constant with value 4.3±0.4. Figure 30 shows a more detailed plot of R in the transition region, 3.4-4.7 GeV. Clear maxima are seen at 3.77[36] GeV and 4.4[37] GeV. In addition, there is a broad region of excitation between 4.0 and 4.2 GeV whose detailed shape appears more complicated than that assumed in the radiative corrections (Figure 23). Statistical errors are shown in Figure 30, the systematic uncertainties are the same as for the data of Figure 29.

Using Equation 5.1, but replacing $N/\bar{\varepsilon}$ by the number of produced events of charge multiplicity p deduced from unfolding Equation 4.7, we obtain the "partial R values" for 2, 4, 6 and >6 produced charged prong events (Figure 31). Again, only statistical errors are given. The additional overall systematic and point-to-point uncertainties are larger for this calculation than for the data of Figure 29 since the R_p are correlated and depend sensitively on the number of events detected in each individual multiplicity

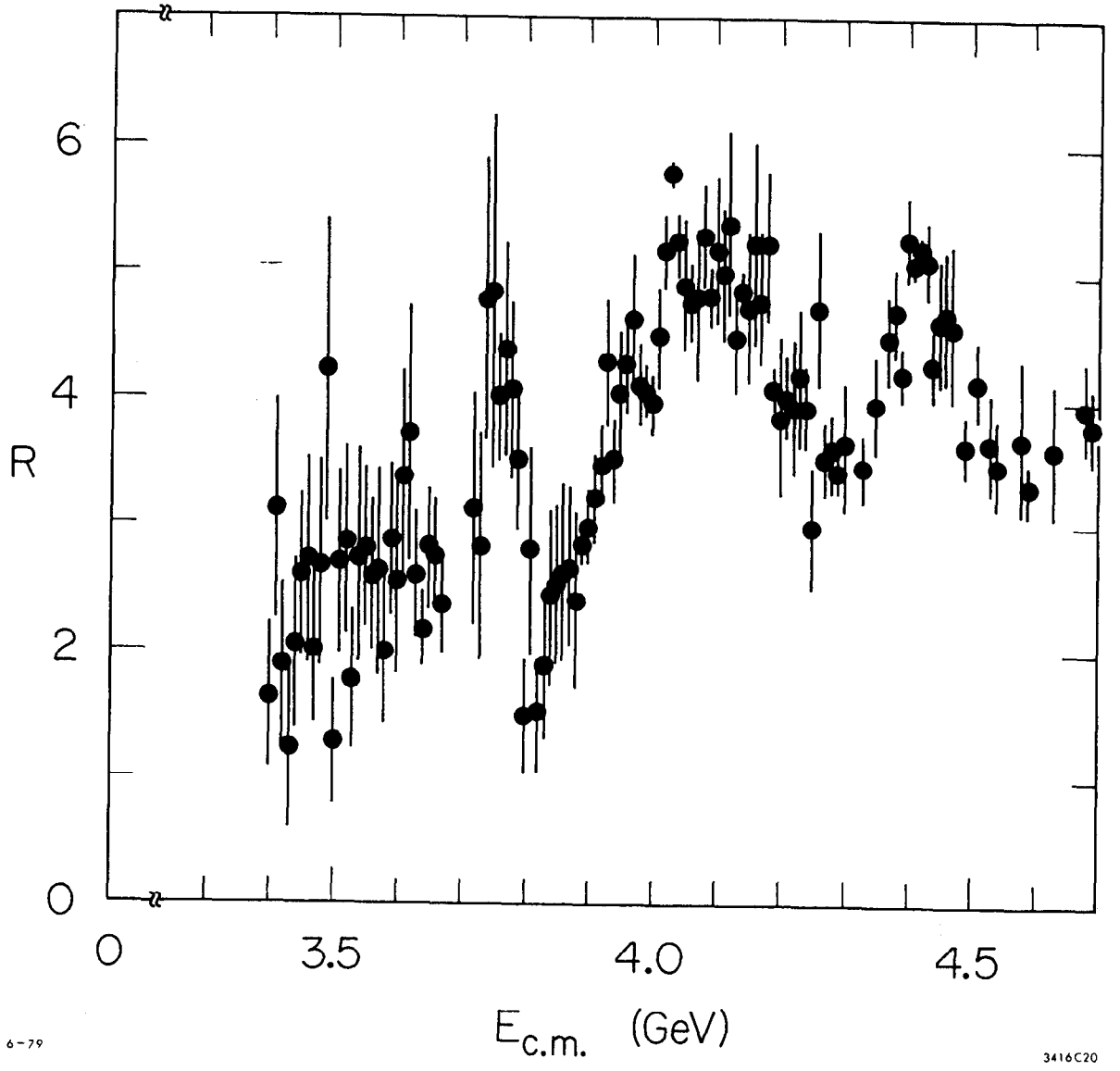

Fig. 30. Detailed plot of $R = \sigma(e^+e^- \to \text{hadrons}) / \sigma(e^+e^- \to \mu^+\mu^-)$ versus E_{cm} in the transition region 3.4 to 4.7 GeV. Tabulated values are contained in Table 4.

TABLE 4

R VALUES FOR FIGURE 30

E_{cm}	R	+/-	E_{cm}	R	+/-	E_{cm}	R	+/-
3.40	1.64	0.58	3.80	1.46	0.41	4.16	5.22	0.80
3.41	3.12	0.88	3.81	2.78	0.84	4.17	4.79	0.53
3.42	1.89	0.64	3.82	1.47	0.45	4.18	5.20	0.58
3.43	1.24	0.65	3.83	1.89	0.57	4.19	4.08	0.17
3.44	2.05	0.67	3.84	2.42	0.68	4.20	3.85	0.63
3.45	2.59	0.65	3.85	2.52	0.61	4.21	3.99	0.32
3.46	2.70	0.84	3.86	2.62	0.72	4.22	3.93	0.53
3.47	2.01	0.60	3.87	2.66	0.64	4.23	4.16	0.57
3.48	2.69	0.84	3.88	2.40	0.70	4.24	3.92	0.32
3.49	4.20	1.20	3.89	2.83	0.17	4.25	2.99	0.47
3.50	1.27	0.49	3.90	2.98	0.28	4.26	4.71	0.63
3.51	2.69	0.74	3.91	3.21	0.34	4.27	3.52	0.27
3.52	2.87	0.76	3.92	3.49	0.30	4.28	3.56	0.31
3.53	1.77	0.55	3.93	4.27	0.49	4.29	3.42	0.17
3.54	2.75	0.85	3.94	3.50	0.33	4.30	3.62	0.50
3.55	2.80	0.64	3.95	4.04	0.51	4.33	3.45	0.26
3.56	2.59	0.59	3.96	4.27	0.38	4.35	3.96	0.38
3.57	2.62	0.84	3.97	4.61	0.53	4.37	4.46	0.34
3.58	2.01	0.60	3.98	4.11	0.33	4.38	4.67	0.38
3.59	2.87	0.59	3.99	4.04	0.19	4.39	4.19	0.21
3.60	2.56	0.74	4.00	3.94	0.22	4.40	5.26	0.34
3.61	3.38	0.86	4.01	4.47	0.36	4.41	5.06	0.10
3.62	3.70	1.01	4.02	5.16	0.30	4.42	5.17	0.09
3.63	2.60	0.52	4.03	5.77	0.10	4.43	5.08	0.30
3.64	2.18	0.31	4.04	5.21	0.25	4.44	4.26	0.28
3.65	2.82	0.49	4.05	4.88	0.50	4.45	4.59	0.49
3.66	2.78	0.43	4.06	4.75	0.27	4.46	4.63	0.53
3.67	2.37	0.39	4.07	4.73	0.59	4.47	4.58	0.62
3.72	3.12	0.94	4.08	5.29	0.40	4.49	3.61	0.22
3.73	2.83	0.88	4.09	4.79	0.22	4.51	4.13	0.31
3.74	4.78	1.16	4.10	5.17	0.56	4.53	3.64	0.38
3.75	4.80	1.37	4.11	4.97	0.21	4.54	3.47	0.34
3.76	4.01	0.51	4.12	5.39	0.72	4.58	3.69	0.57
3.77	4.38	0.84	4.13	4.47	0.42	4.59	3.26	0.20
3.78	4.05	0.69	4.14	4.83	0.14	4.63	3.59	0.52
3.79	3.52	0.55	4.15	4.72	0.59	4.68	3.93	0.36
						4.69	3.77	0.29

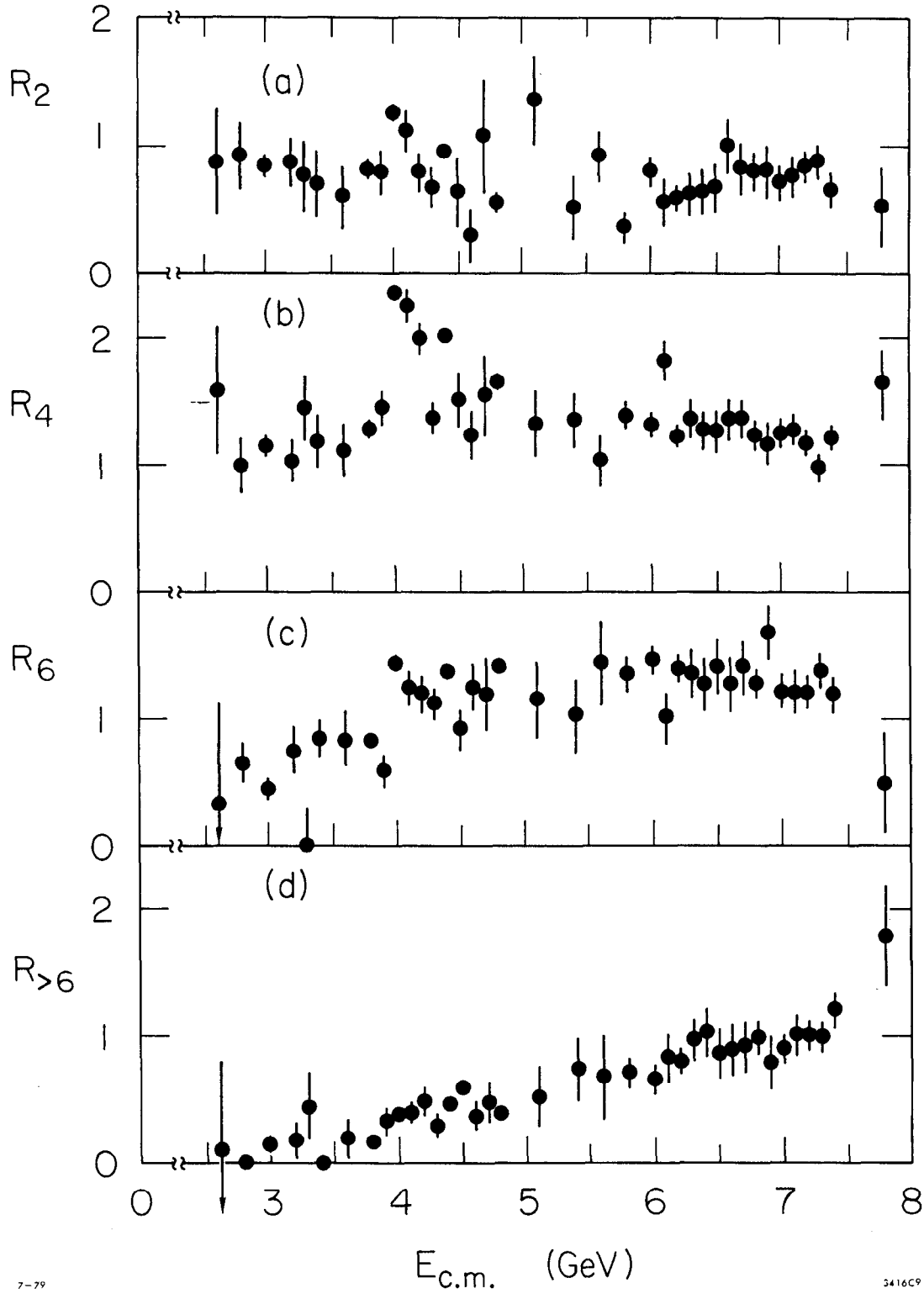

Fig. 31. Partial R values for 2, 4, 6 and >6 charged prong events produced versus E_{cm}.

bin. The overall systematic uncertainty is estimated to be ±25% for E_{cm} = 2.6 GeV varying smoothly to ±15% for $E_{cm} \geq 6$ GeV. The point-to-point fluctuations are estimated to be ±5%.

Figure 32 shows the produced charged production fractions f_2 - $f_{>6}$ calculated as the ratio of R_p to R. The production fractions show smooth variation across the energy range with no peaks in the threshold region near 4.0 GeV. The effect of the charm contribution to the annihilation yield is to increase the total R value while leaving the multiplicity distribution unchanged.

These results for the total R values and the R_p values are in good agreement within quoted errors, with data from the experiments of Pluto[38] and DASP[39] (Figure 33). For E < 3.7 GeV, all experiments agree on a flat R and agree on the value to within ±10%. All experiments find structure in the 4.0-4.2 GeV region, but a detailed comparison depends crucially on radiative corrections in this region. All experiments find a clear peak at 4.4 GeV, but differ as to its height and width. Again, this comparison depends sensitively on the radiative corrections applied. Around 5 GeV experiments again agree on the value of R to within ±10%. Figure 34 shows the partial R value R_2 from the Pluto collaboration, again, in satisfactory agreement with the results reported here. In summary, agreement in R is

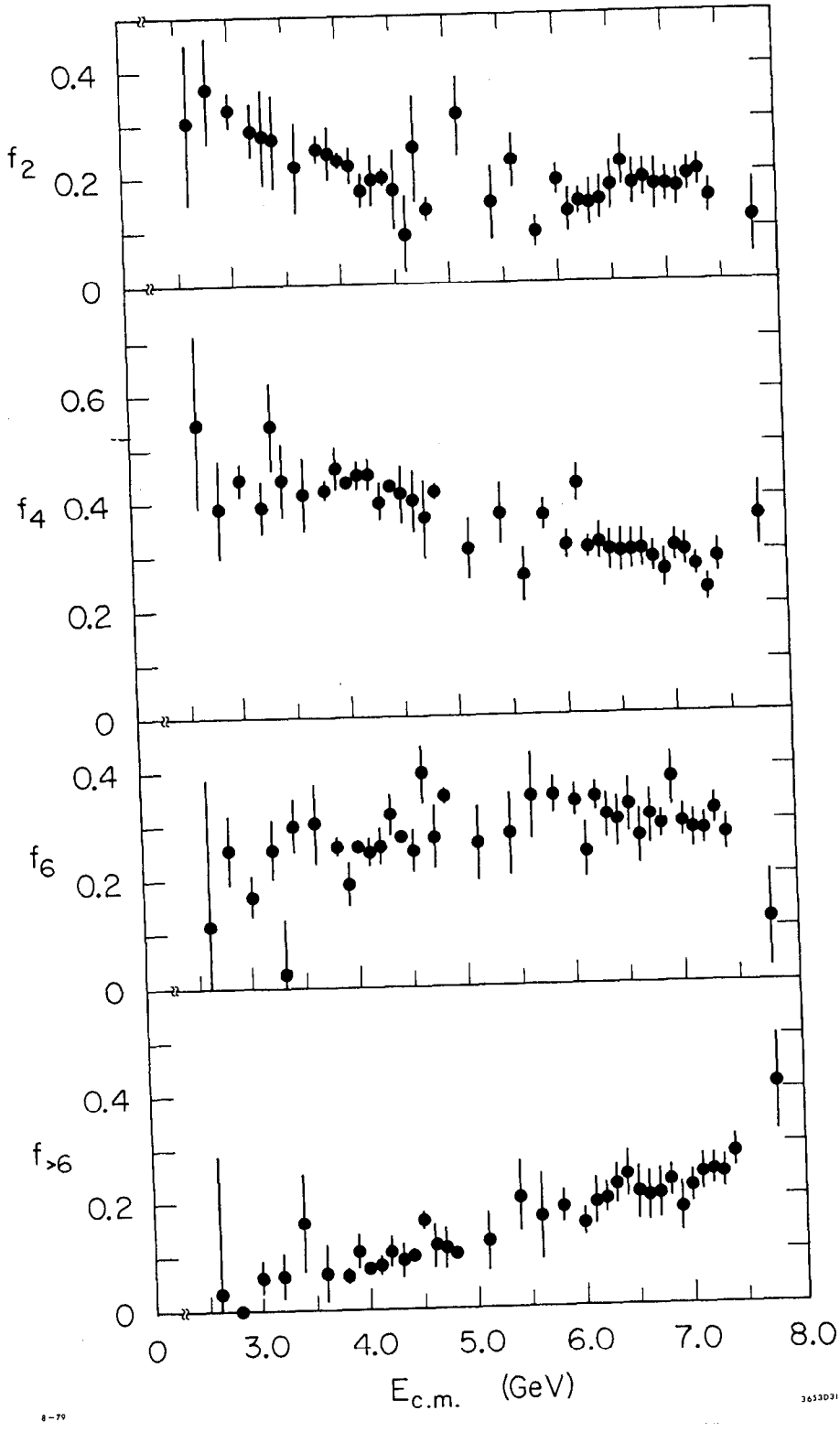

Fig. 32. Produced charged production fractions f_2-$f_{>6}$ (the ratio of R_p to R) vs. E_{cm}.

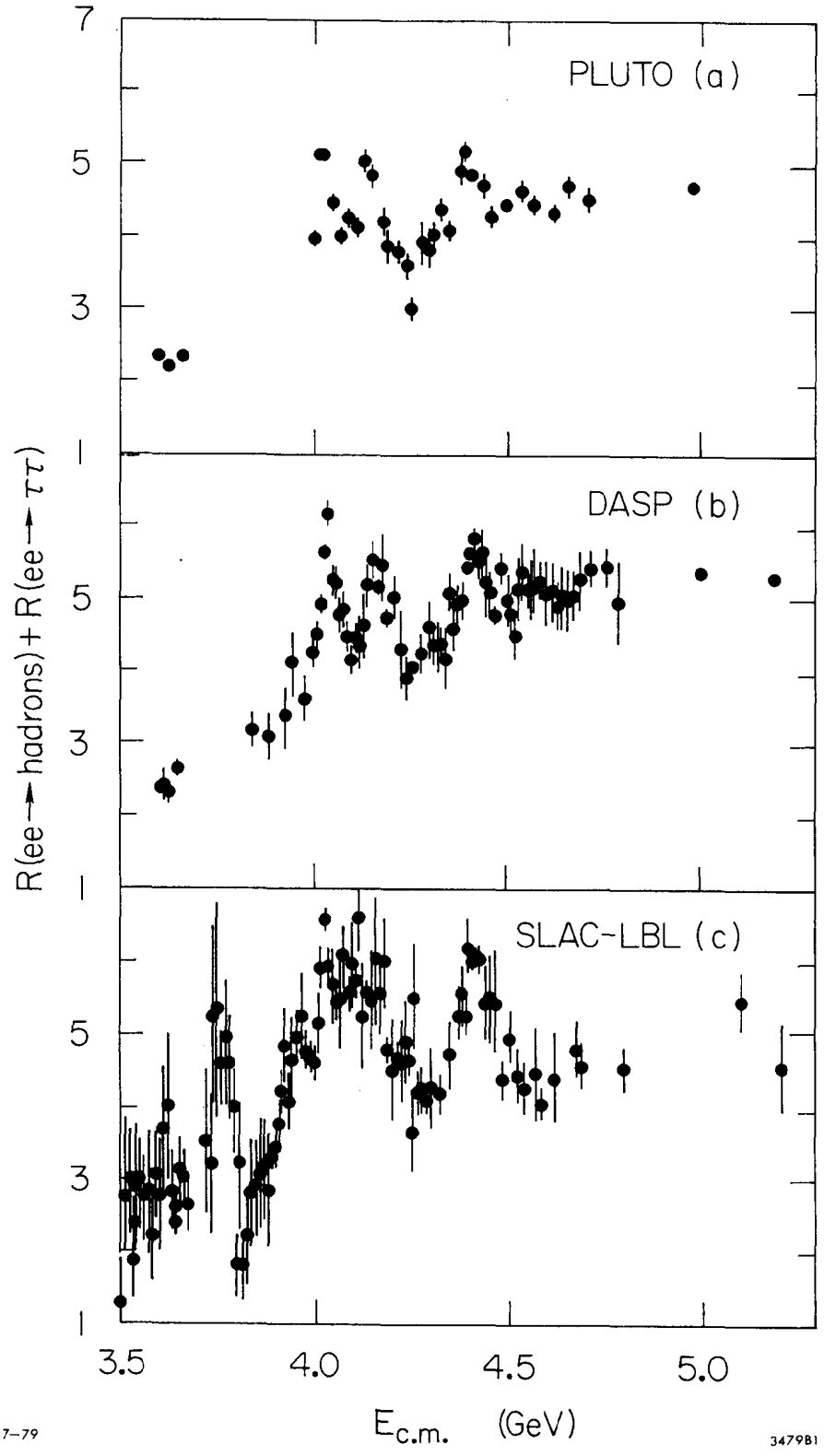

Fig. 33. R values for this experiment (SLAC-LBL), PLUTO, and DASP versus E_{cm}. The heavy lepton contribution has been added.

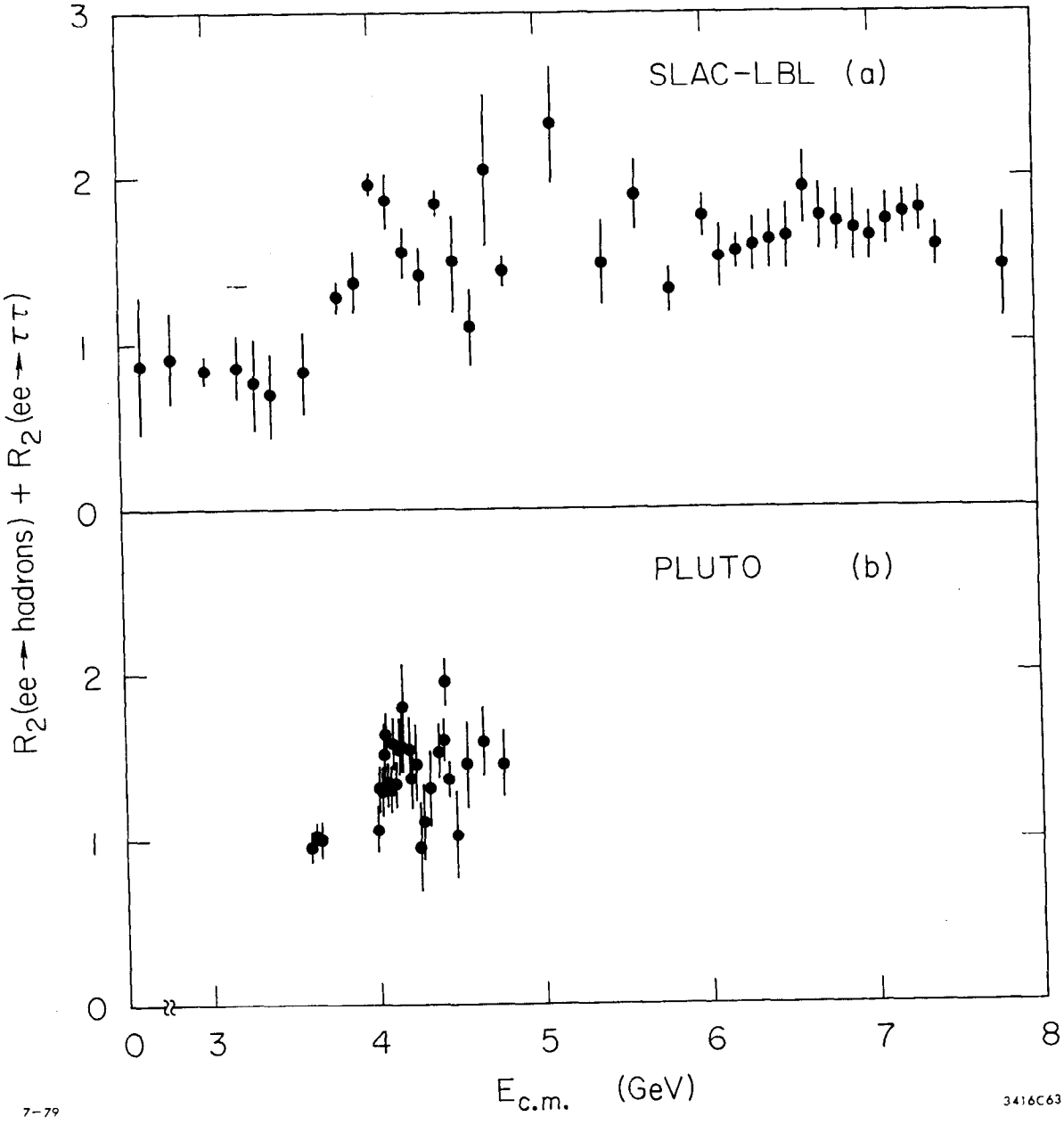

Fig. 34. R for 2 charged prong-produced events with the heavy lepton contribution added for this experiment (SLAC-LBL) and the PLUTO experiment.

good, well within quoted systematic uncertainties and possible differences in radiative corrections applied.

B. Moments

In spite of the dramatic change in the production dynamics indicated by the data in the 4.0 GeV region, there is little change in the average properties of events in this region. Figure 35 shows the mean produced charged particle multiplicity as a function of energy using the unfold results. We see variation consistent with $Ln(E_{cm})$ behavior, well represented by

$$\langle N_{ch} \rangle (E_{cm}) = A + BLn (E_{cm}), \; A = 2.09, \; B = 1.67.$$

From comparison of the phase space and jet model unfold results, we estimate the systematic uncertainty on the mean charged multiplicity is ±5%.

Figure 36 shows corrected values for the produced mean track momentum and mean charged energy fraction as a function of energy. Again, these plots show little or no sharp variation with energy. Care must be taken in interpreting the behavior of the energy dependence of the charged energy fraction shown in Figure 36. A more complicated production model, including the effect of heavy particles, does not show the fall of mean charged energy fraction with increasing beam energy.[40] This effect is model dependent and may only be an artifact of our simple all-pion model.

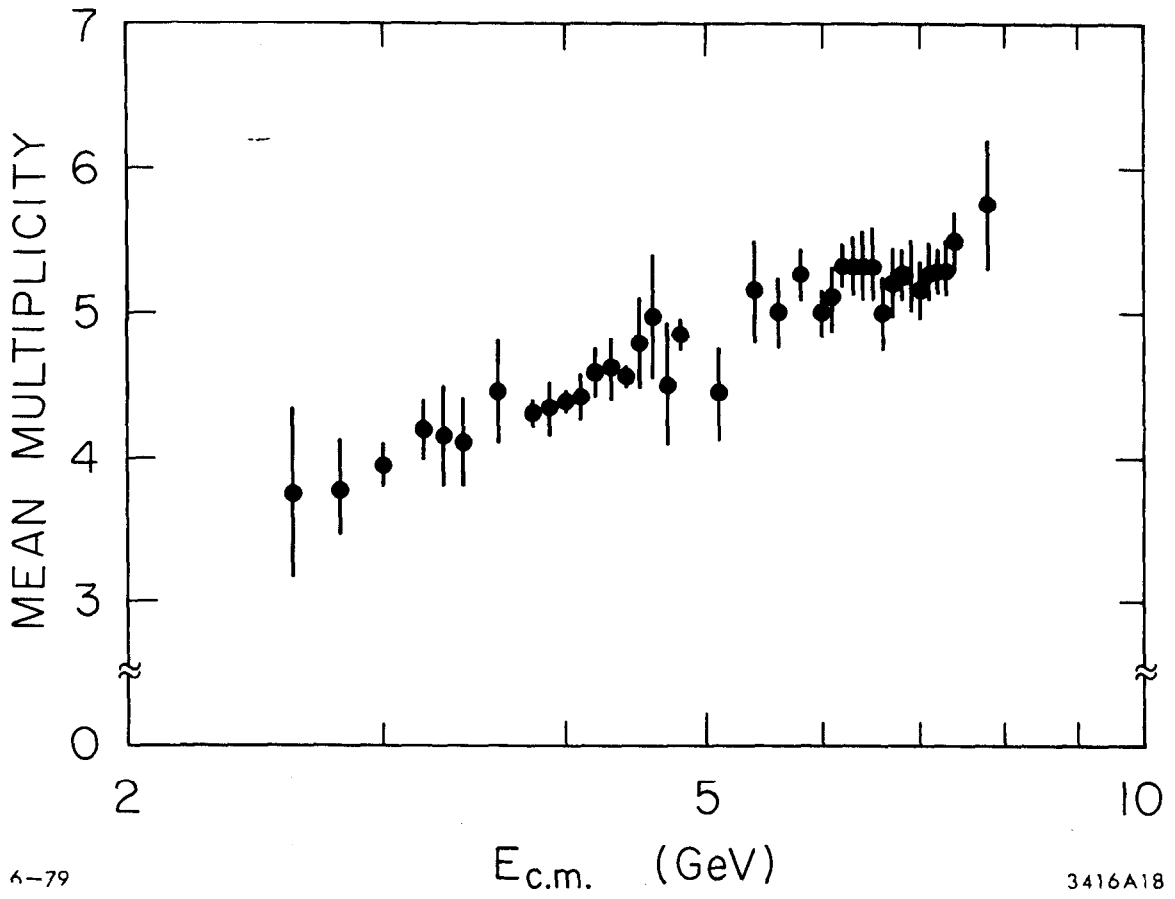

Fig. 35. Mean produced charged multiplicity versus E_{cm}. Tabulated values are contained in Table 5.

TABLE 5

MEAN MULTIPLICITY VALUES FOR FIGURE 35

E_{cm}	Mean Charged Multiplicity	+/-	E_{cm}	Mean Charged Multiplicity	+/-
2.60	3.75	0.59	5.40	5.15	0.35
2.80	3.79	0.34	5.60	4.96	0.26
3.00	3.93	0.13	5.80	5.28	0.18
3.20	$4.1\bar{9}$	0.21	6.00	4.97	0.15
3.30	4.14	0.35	6.10	5.09	0.23
3.40	4.10	0.31	6.20	5.32	0.14
3.60	4.44	0.35	6.30	5.33	0.22
3.80	4.29	0.09	6.40	5.33	0.23
3.90	4.32	0.19	6.50	5.32	0.27
4.00	4.37	0.05	6.60	5.02	0.25
4.10	4.40	0.14	6.70	5.20	0.24
4.20	4.58	0.18	6.80	5.27	0.19
4.30	4.61	0.21	6.90	5.27	0.27
4.40	4.56	0.05	7.00	5.15	0.20
4.50	4.79	0.32	7.10	5.28	0.21
4.60	4.98	0.43	7.20	5.29	0.16
4.70	4.49	0.42	7.30	5.30	0.18
4.80	4.85	0.10	7.40	5.49	0.20
5.10	4.43	0.32	7.80	5.75	0.46

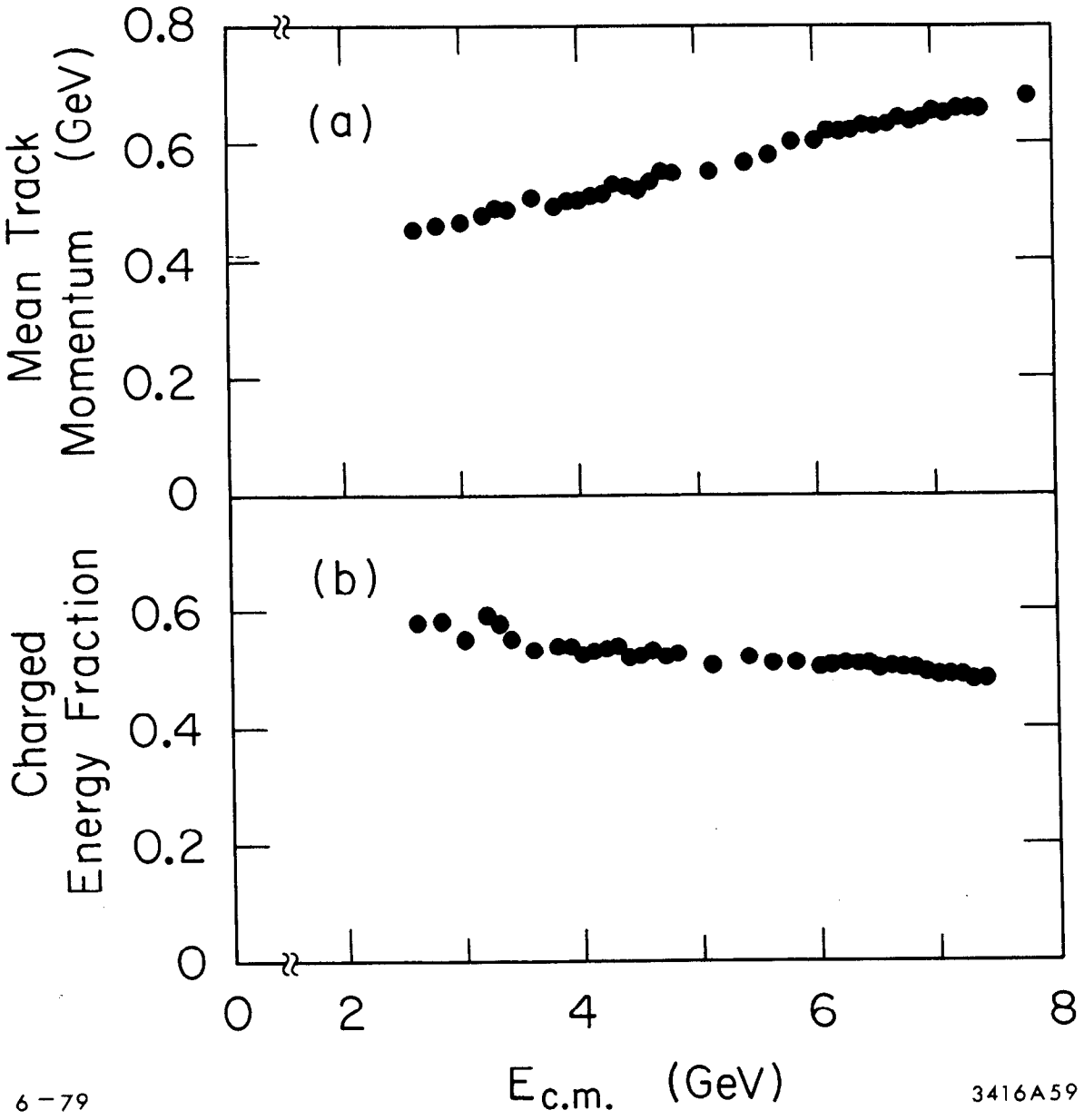

Fig. 36. a) Corrected mean charged particle momentum versus E_{cm}.
b) Corrected charged energy fraction versus E_{cm}.

C. Inclusive Momentum Spectra

The inclusive momentum spectrum, $\frac{d\sigma}{dx}$, is given for each x bin by

$$\frac{d\sigma}{dx}(x_i) = \frac{N(x_i).}{\varepsilon(x_i).L.\delta x_i} \qquad (5.2)$$

where $N(x_i)$ is the number of detected tracks in the bin centered on $x = x_i$, δx_i is the bin width, and $\varepsilon(x_i)$ is the single particle inclusive detection efficiency determined by the Monte Carlo calculation evaluated at $x = x_i$. No correction for ψ,ψ' radiative contribution is required, since spectra have been measured only at energies far enough away from the resonances that their effects are negligible.

Figure 37 shows the $s\frac{d\sigma}{dx}$ distributions vs. x. These values of differential cross section are subject to larger possible systematic errors than are the total cross section measurements, since their determination does not use an "unfold" procedure, and hence depends more critically on properties of the assumed production model. The $s\frac{d\sigma}{dx}$ results are subject to possible systematic uncertainty of ±15% at the highest and lowest x values, with smooth variation across the range of x. Also, the results at $x > 0.8$ are less reliable because of possible systematic errors from non-Gaussian tails of the momentum resolution at high x, and

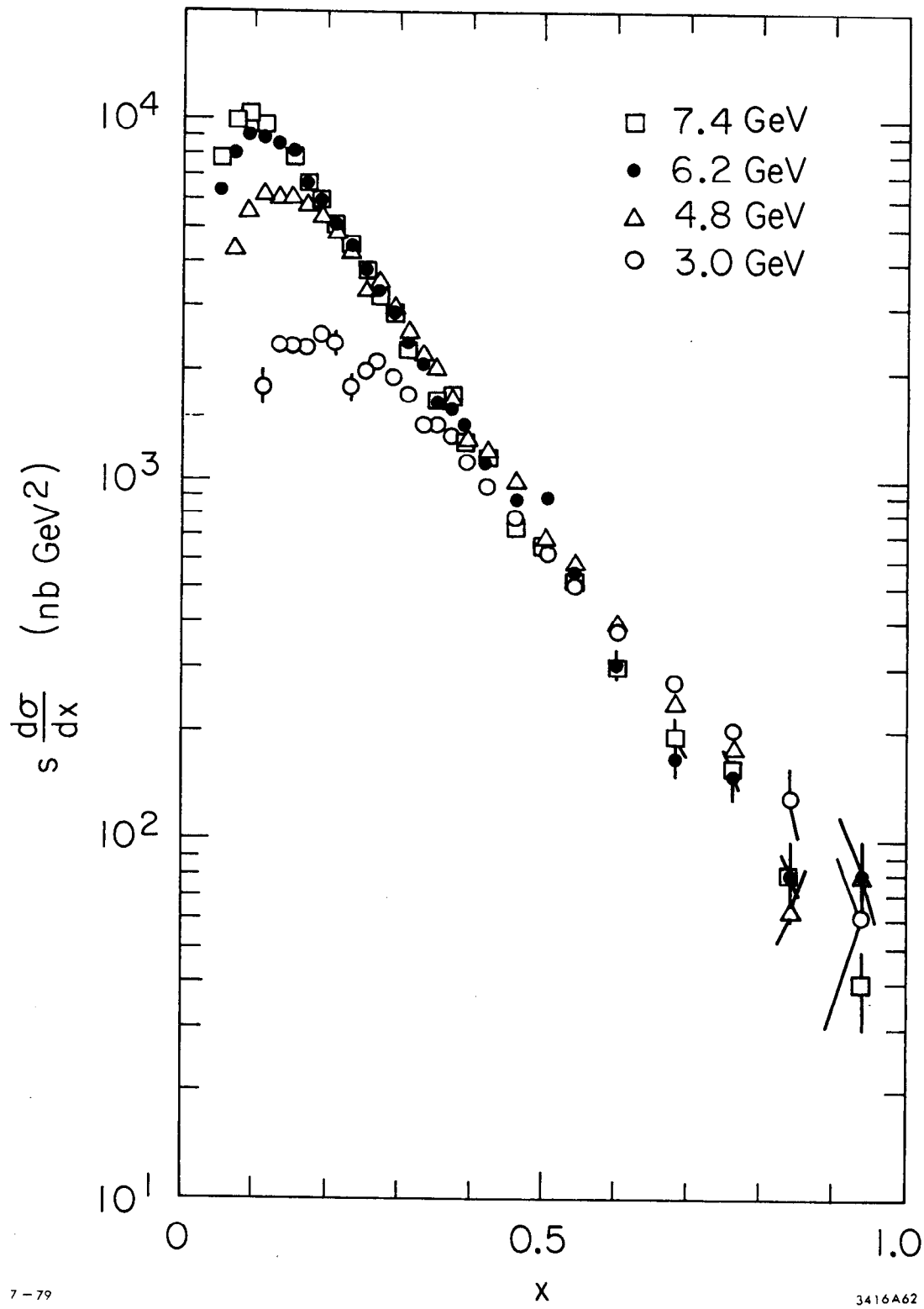

Fig. 37. Corrected single particle inclusive x distribution versus x.

the possibility of leakage from QED events into the hadronic event sample. Figure 38 shows for comparison $s\frac{d\sigma}{dx}$ at 4.03 GeV and 7.4 GeV. The data at 4.03 GeV show a "bulge" in the region $0.2 < x < 0.4$ relative to the "scaling" curve, the 7.4 GeV data. This "bulge" is due to the resonance charm particle production.

The integral of the inclusive spectrum is

$$\frac{1}{\sigma_{\mu\mu}} \int \frac{d\sigma}{dx}\, dx = \frac{3}{4\pi\alpha^2} \int s\frac{d\sigma}{dx}\, dx = R \quad \langle n_{ch} \rangle \quad . \qquad (5.3)$$

This sum-rule states that the area under the $s\frac{d\sigma}{dx}$ curves will rise with increasing energy, because the mean charged multiplicity is growing approximately logarithmically. This effect can be seen in Figure 37 as an increase restricted to the region $x \lesssim 0.3$, while in the region $x \gtrsim 0.3$ data lie on a universal curve (scaling). As a cross check on our methods, Table 6 compares $\frac{3}{R4\pi\alpha^2} \int s\frac{d\sigma}{dx}\, dx$ with $\langle n_{ch} \rangle$ as calculated from the inclusive cross section data of Figure 37 and the mean charged multiplicity and R data of Figures 29 and 35. The required extrapolation to small and large x was made with the Monte Carlo jet model distributions. As can be seen from Table 6 the values agree within 10%.

In order to better illustrate the scaling behavior, we show $s\frac{d\sigma}{dx}$ vs. E_{cm} in various x bins in Figure 39.

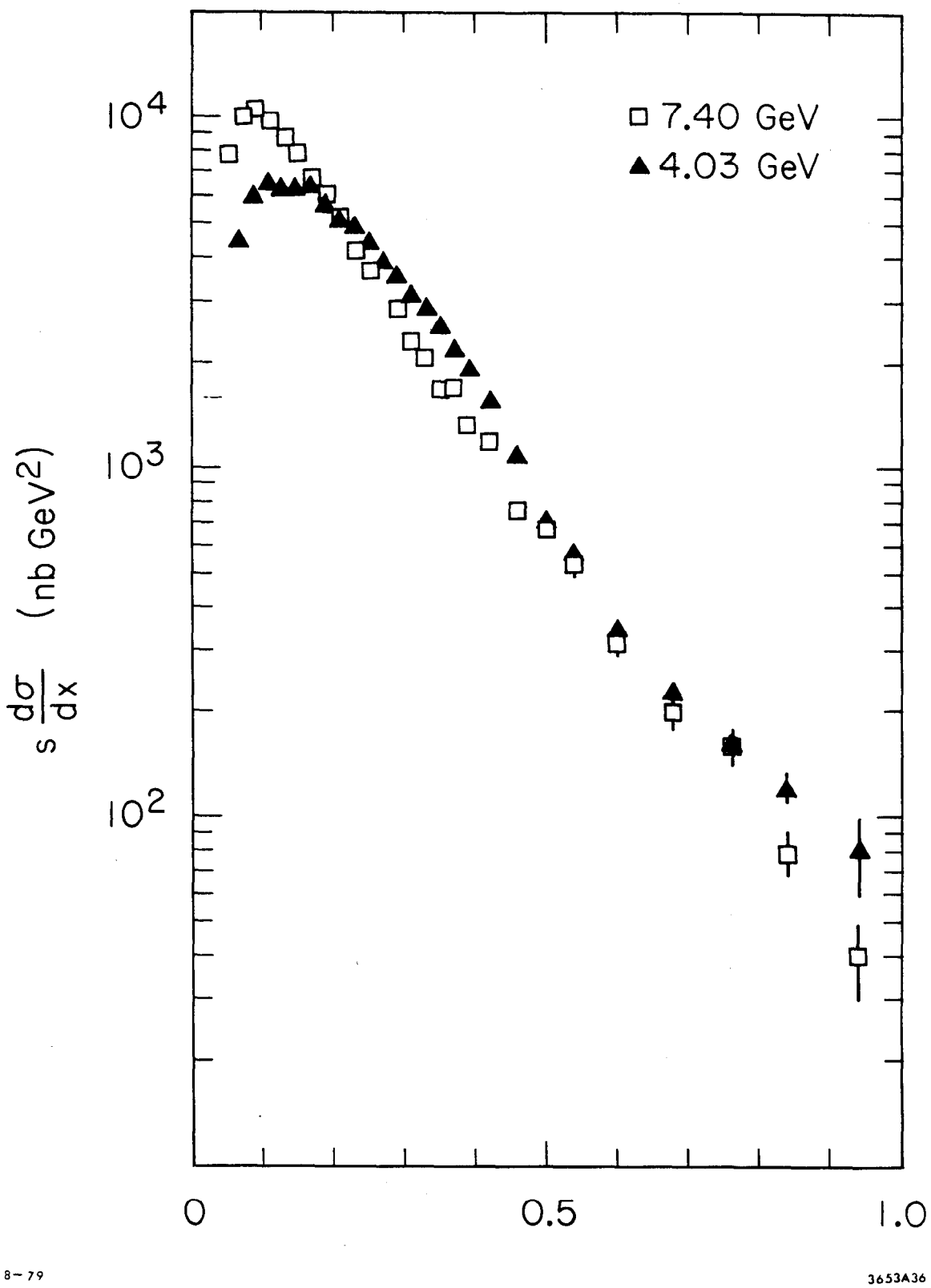

Fig. 38. Corrected single particle inclusive x distribution vs. x at 7.4 GeV and 4.03 GeV.

TABLE 6

COMPARISON OF THE SUM RULE OF EQUATION 5.3

ERRORS ARE STATISTICAL

E_{cm}	$\frac{3}{4\pi\alpha^2} \int s\frac{d\sigma}{dx}\, dx \,/\, R$	$\langle n_{ch} \rangle$
3.0	3.7 ± 0.2	3.9 ± 0.1
4.8	5.5 ± 0.2	4.9 ± 0.1
6.2	5.9 ± 0.3	5.3 ± 0.2
7.4	5.9 ± 0.3	5.5 ± 0.2

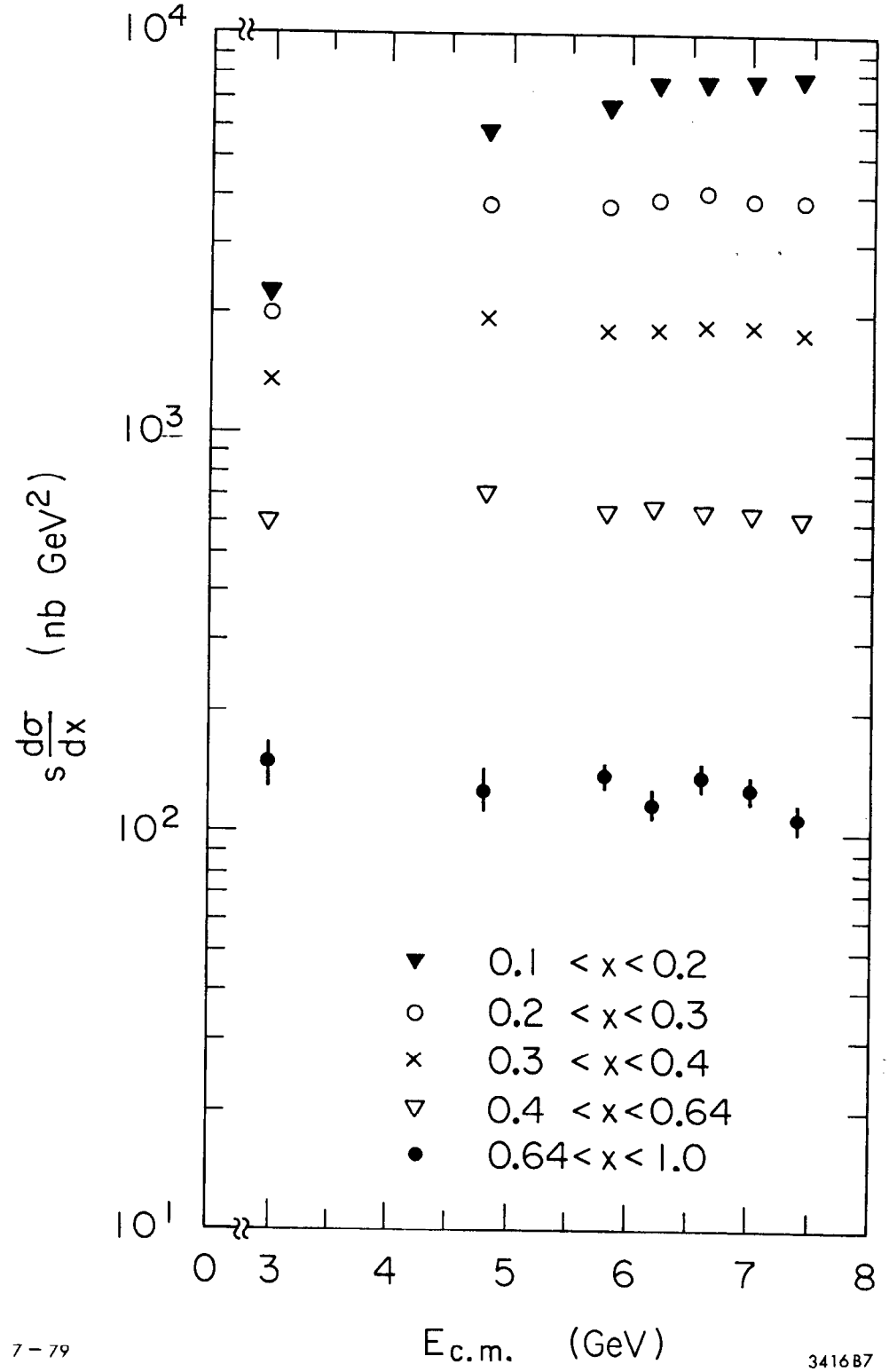

Fig. 39. Corrected single particle inclusive x distribution versus E_{cm}.

Scaling behavior is clearly evident for $x \gtrsim 0.3$. The data in Figure 37 are well approximated by the form $s\frac{d\sigma}{dx} = ce^{-\beta x}$ for $x > 0.3$, with $\beta = 6.8 \pm 0.3$ and $c = 2 \pm 0.3 \times 10^4$ where estimates of systematic uncertainties have been included in the stated errors. The inclusive momentum distributions reported here agree, within systematic errors, with previously published results from Pluto and DASP.[41]

The single particle angular distributions were fitted to the form $1 + \alpha\cos^2\theta$. Figure 40 shows best-fit values of α for various energies as a function of x. The α values appear to rise from the region $x \sim 0.3$ to a value consistent with the polarized beam measurement.[28] Although the statistical errors here are large, this measurement shows qualitatively that the angular distributions behave as one would expect in a spin-½ parton model.

D. Comparison with QCD Predictions

As discussed in the introduction, the ratio R in spin ½ quark-parton models is just

$$R = \sum_i (Q_i/e)^2$$

where the sum runs over available partons. Comparing this prediction with the data in the scaling regions $E_{cm} = 3$ GeV and $E_{cm} = 6$ GeV, we find ∿30% disagreement, with the data lying above the prediction. Here we have used the standard model with 3 colors and 3 quarks at 3 GeV, and 3 colors and

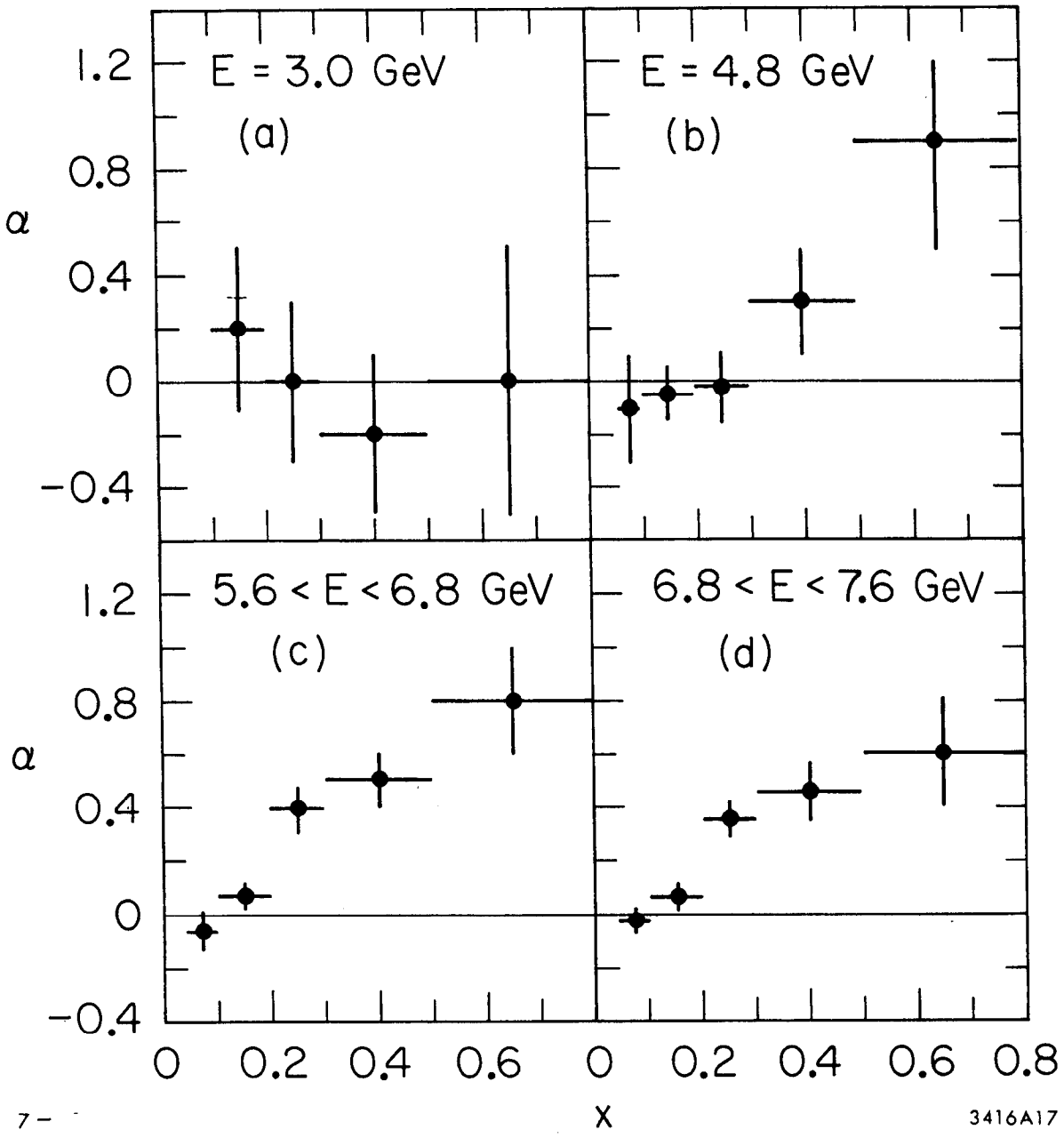

Fig. 40. Angular distribution coefficient versus x.

4 quarks at 6 GeV (R(3GeV) = 2, R(6GeV) = 10/3). Corrections for strong interactions among final state particles calculated in quark-gluon perturbation theory (QCD) through order α_s are[42]

$$R(s) = \sum_i (Q_i/e)^2 \, (1 + \alpha_s(s)/\pi)$$

where $\alpha_s(s)$ is the running strong coupling constant, and quark mass corrections have been neglected. If we apply this result in the scaling regions to determine $\alpha_s(s)$ from the data we find

$$\alpha_s(6 \text{ GeV}) = .82 \pm .38, \quad \alpha_s(3 \text{ GeV}) = 1.2 \pm .8 \quad .$$

These values for $\alpha_s(s)$ are higher than those determined from deep inelastic scattering ($\alpha_s \sim .2\text{-}.3$),[42] but are consistent with each other within the large systematic errors.

As discussed by Poggio, Quinn, and Weinberg,[42] the determination in quark-gluon perturbation theory of the total hadronic cross section is complicated in the SPEAR energy regime by the new quark threshold phenomena. This may preclude straightforward interpretation of the above results for α_s. These authors suggest a "smeared" R may be more reliably calculable since threshold behavior is averaged over. Their smeared function is

$$\bar{R}(s,\Delta) = \frac{\pi}{\Delta} \int_0^{\infty} \frac{R(s')\, ds'}{(s'-s)^2+\Delta^2} \quad . \tag{5.4}$$

We used $\Delta = 3.0$ GeV^2 and integrated from $s = 4.0$ GeV^2 to ∞, with $R = 2.75$ for $4 < s < 5.96$ GeV^2, our data from $s = 5.96$ to $s = 63.48$ GeV^2, and $R = 4.30$ for $s > 63.48$ GeV^2. The narrow resonances ψ and ψ' were not included in the calculation of $\bar{R}$. The result is shown in Figure 41, with calculated results of Poggio, Quinn, and Weinberg from a model containing 4 quarks. The data of Figure 41 are subject to the same systematic uncertainties as the R measurement, a possible 10% smooth variation from the highest energy to the lowest, and a ±10% overall systematic uncertainty. The "smearing" removes the contribution from point-to-point systematic errors. The calculation agrees with the data within the quoted errors up to $S \sim 30$ GeV^2. Above $S \sim 30$ GeV^2, the data lie systematically above the model, on the edge of the quoted systematic uncertainty.

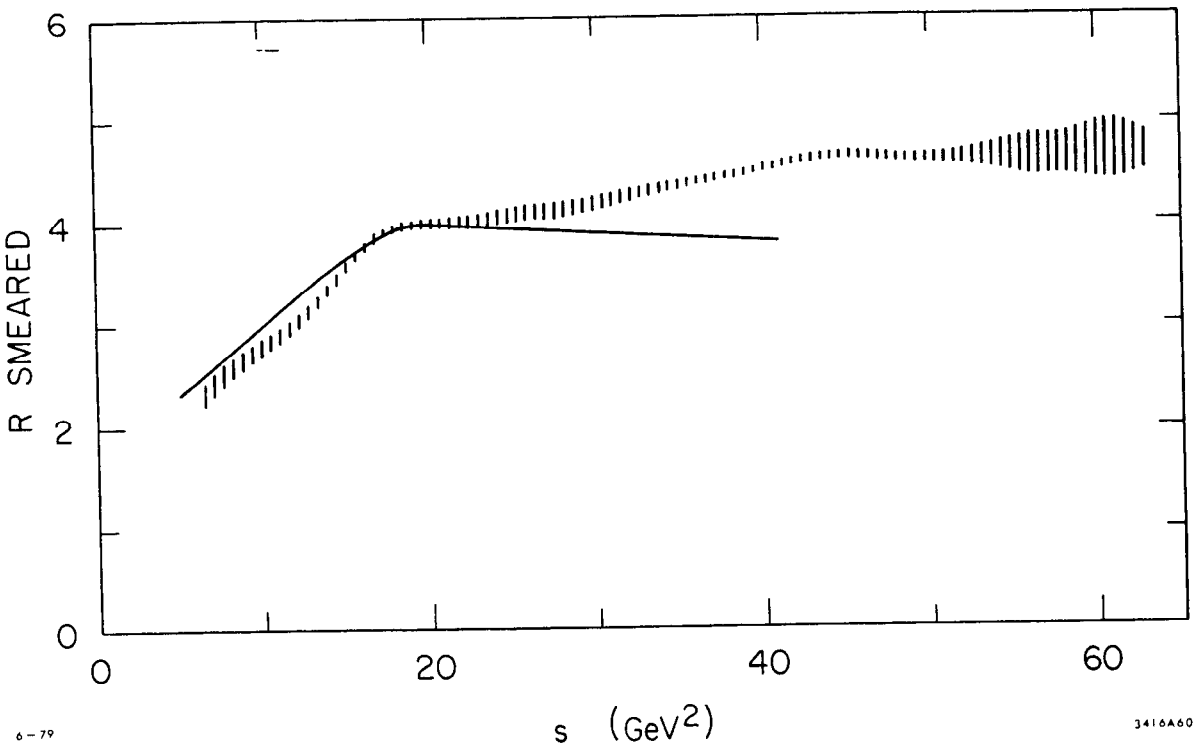

Fig. 41. Smeared R (Equation 5.4) versus s. The curve is a prediction of Poggio, Quinn, and Weinberg for a model containing 4 quarks.[42]

VI. THE MARK II MAGNETIC DETECTOR

A. Introduction

The SLAC-LBL Mark II magnetic detector was installed in the West experimental area of SPEAR in the summer of 1977, and came into full operation in the spring of 1978. The design of the Mark II is quite similar to that of the Mark I detector, but with significant improvements making the Mark II a more powerful detector for all aspects of e^+e^- physics. In particular, many of the trigger and detection biases important for total cross section and inclusive momentum spectra measurements have been reduced in the Mark II relative to the Mark I. The purpose of the Mark II is to provide as wide a solid angle coverage as possible for measurement of the properties of the particles produced in the beam collision region. The detector covers 32° to 148° in polar angle with 2π azimuthal acceptance for a total of 0.85 of 4π solid angle coverage. Figures 42 and 43 provide an expanded view and an end view of the detector.

Particles emerging from the region of the beam collision pass in sequence through the vacuum chamber, cylindrical scintillation counters immediately surrounding the vacuum chamber, a system of cylindrical wire drift chambers, an array of time-of-flight scintillation counters, the magnet coil, an array of lead and liquid argon shower counters, and finally two layers of interleaved magnet flux

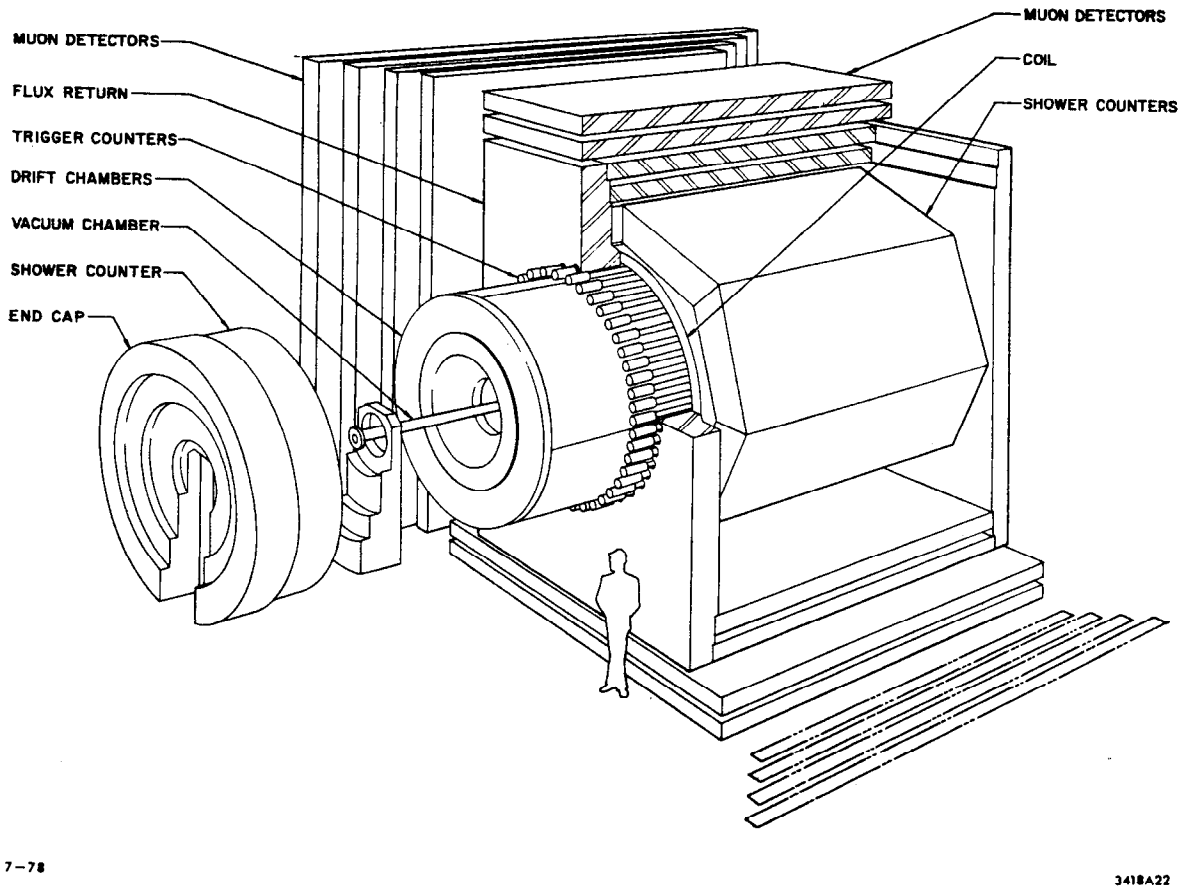

Fig. 42. Expanded view, Mark II magnetic detector.

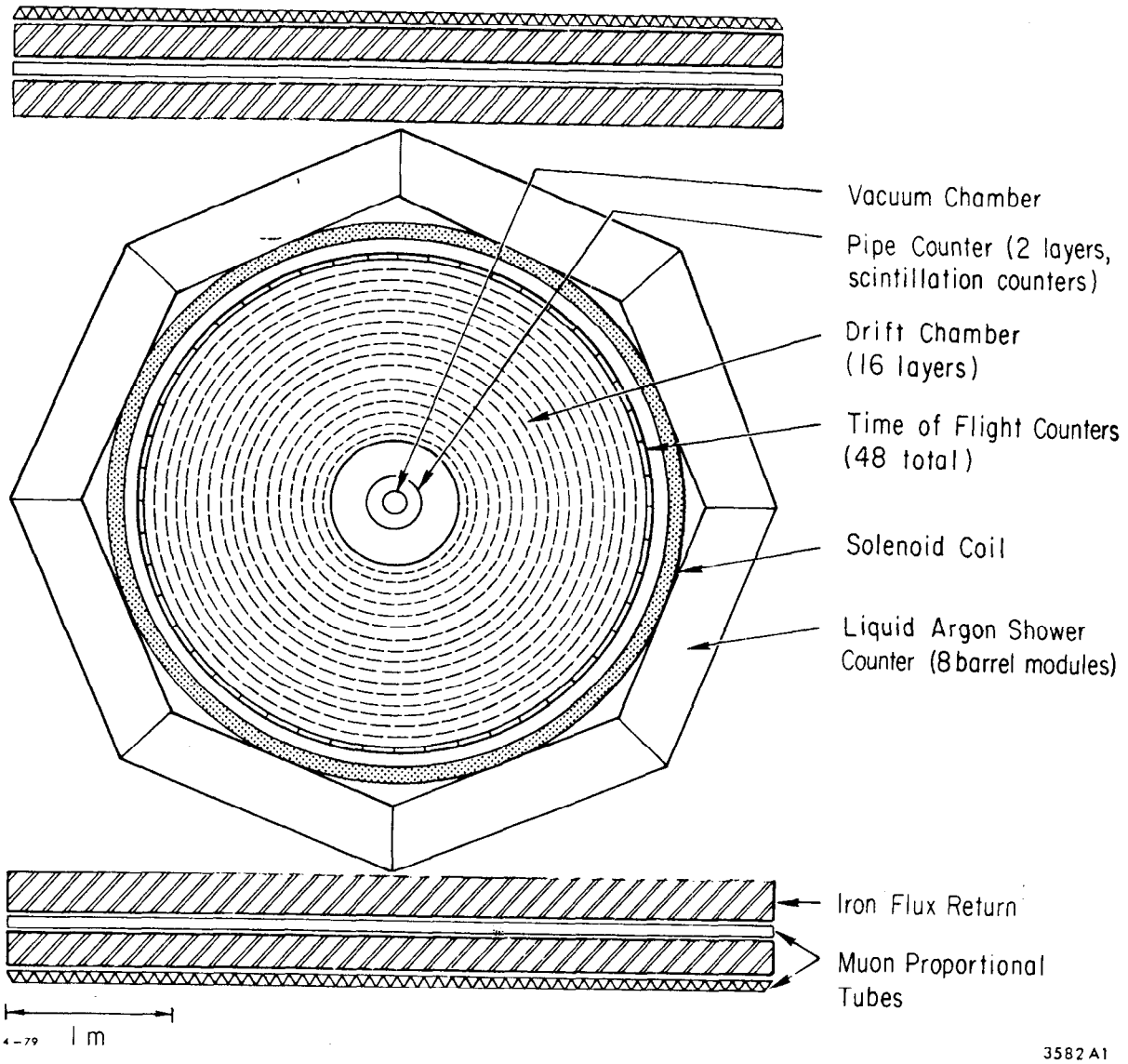

Fig. 43. End view, Mark II magnetic detector.

return and proportional tubes. Table 7 summarizes the radii, lengths, angular range covered, and thickness for each of the detector components.

The vacuum chamber is a corrugated cylinder of stainless steel. The four hemi-cylindrical plastic scintillation counters immediately surrounding the vacuum pipe ("pipe counters") are each viewed through a lucite light pipe by a 56DVP phototube. The primary purpose of these counters is to provide cosmic-ray rejection in the detector trigger. The 16 cylindrical layers of drift chambers (Figure 44) outside the pipe counters share a common volume with a 50% argon 50% ethane gas mixture. The signal wire spacing is 18 mm for the 6 innermost layers and 36 mm for the outer 10 layers. The wires in each layer alternate in angle with respect to the beam line (0^{o}, $+3^{o}$, -3^{o}), starting with the inner layer axial. Chamber signals are amplified and latched after each beam crossing. The rms spatial resolution in the azimuthal direction is 200μ, the rms z resolution is 0.38 cm. Complete details of the drift chamber system are given in Reference 43.

Immediately surrounding the drift chambers lies a ring of 48 plastic scintillation counters, each 20 cm wide and viewed at each end by an XP2230 phototube. These scintillation counters ("TOF counters") determine flight times for charged particle identification and are used in the detector trigger. Signal pulse heights are recorded in order to

TABLE 7

MARK II DETECTOR COMPONENTS
(All dimensions cm)

Item	Average Radius	Fraction of 4π Acceptance	Length (Z)	Thickness	Fraction of Radiation Length	Fraction of Absorption Length
Beampipe	8.0	-	-	0.021	0.012	-
Pipe Counters	12.1	0.95	81	3.8	0.038	0.02
Air Space	28.1	-	-	28.3	0.001	-
Lexan Window	37.3	0.95	179	0.32	0.009	-
Drift Chambers	41 - 144	0.92-0.66	198.4-264.6	113	0.009	-
Outer Can	150.6	0.66	264.6	0.64	0.071	0.02
TOF Counters	152.4	0.76	304.2	2.6	0.064	0.04
Coil	165	0.78	411.5	14	1.2	0.29
Shower Counters	197	0.70	380	41	14	0.42
Flux Return	246	0.68	450	23	13	1.35
Prop. Tubes	271	0.61	450	2.6	0.04	-
Flux Return	282	0.63	450	23	13	1.35
Prop. Tubes	295	0.48	450	2.6	0.04	-

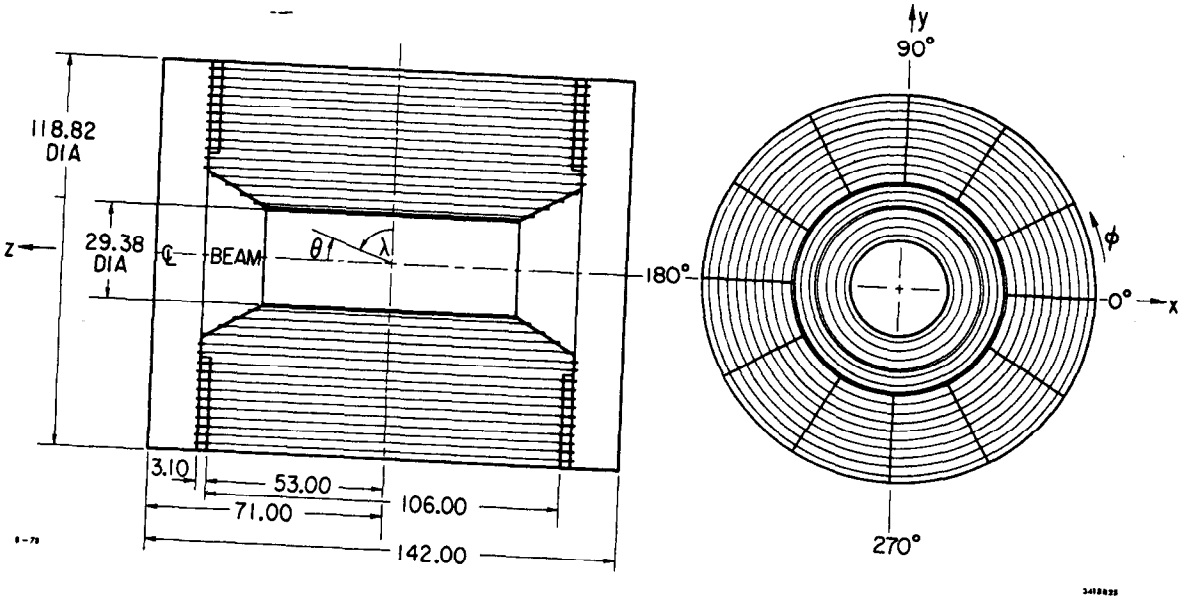

Fig. 44. Mark II drift chamber system (all dimensions in inches).

enable off-line correction for time slewing. The rms time-of-flight resolution for this system is about 300 psec.

Outside the solenoid coil is an array of 8 lead and liquid argon shower counters providing electron-hadron identification information. Each counter consists of 18 alternating layers of lead strips and plates, each 2 mm thick, with liquid argon in the 3 mm gaps. In the lead stack there are three determinations of ϕ, two of θ, and one at 45°(U) with 3.8 cm wide θ and ϕ strips and 5 cm wide U strips. The eighteen layers are ganged for readout with the first four samples interleaved to provide six samples in depth. The signals are amplified, shaped, and the peak value held for each beam crossing. The rms energy resolution of these shower counters as measured with Bhabha scattering events is $\delta E/E \sim 11.5\%/\sqrt{E(GeV)}$. Details of the mechanical design, cryogenic systems, and electronics readout can be found in Reference 44. The muon detection tubes, the proportional chamber and liquid argon ionization chamber endcaps, and the photon detection capabilities of the shower counters were not used in this analysis. They are discussed in Reference 44.

The magnetic field is generated by a main solenoid winding in series with two compensation coils that serve to ensure $\int B.d\ell$ along the beam line is zero, a necessary condition for stable beam storage. The magnet dissipates 2.8 MW at the operating current of approximately 4000 Amps.

layer and the axial layer drift chamber latch information is inspected by hardware for tracks in the chambers.[45] If the hardware fails to satisfy preset trigger criteria on the number of tracks found, the latches are cleared and the system made ready for another beam crossing signal after a ∿35 μsec delay. If the preset trigger criteria are satisfied, the chamber, counter, and shower module information is transferred via CAMAC to a VAX 11/780 computer that writes ∿4 k bytes of data per event onto tape. Some 80% of the events are analyzed with the VAX to give information used for monitoring chamber and counter efficiencies, as well as general detector performance. The trigger system is disabled for ∿60 msec after an event to allow time to transfer the data to tape.

The detector trigger rate depends sensitively on the preset trigger criteria. The data used in this analysis were recorded with a trigger that required two charged particles. The trigger demanded first, one track in the barrel region ($|\cos\theta| < 0.65$, $p_\perp > 100$ MeV) with a TOF counter on the end of the track and hits on at least 4 of the 6 axial drift chamber layers, and second, at least one other track with hits on at least 3 of the inner 5 drift chamber layers. The algorithms used and the track finding hardware are discussed in detail in Reference 45. The trigger rate with this trigger ranges from ∿1 HZ at 4.0 GeV up to ∿5 HZ at 6.0 GeV, depending on SPEAR beam

The solenoid field is monitored by a magnetic-resonance probe located inside the flux return but outside the tracking volume. The field was mapped with a Hall probe before the tracking chamber package was inserted into the coil. Field components were measured at about 3000 points over the tracking volume ($r = 0.13$ to 1.5 m, $-1.40 < z < 1.40$ m). The variation of the field magnitude was found to be 2.5%. A polynomial expression in r and z was fit to the field data to yield a parameterization accurate to 0.03% in B_z and 2 Gauss in Br and Bø. The absolute value of the field strength was measured at the center of the magnet by a magnetic resonance probe to be 4042±1 Gauss at the operating current. The error in the measured track momenta due to uncertainty in the field is much smaller than the measurement error in the tracking chambers.

B. Trigger

The Mark II trigger is derived from signals from a beam pickup electrode, pipe counters, TOF counters, and the drift chambers. Hits in the drift chambers (counters) are latched using a 430 nsec (12 nsec pipe, 50 nsec TOF) wide gate derived from the beam pickup signal. If fewer than 4 of 9 drift chamber layers had signals, or no valid pipe latch configuration was found, all latches are cleared and the system made ready for the next beam crossing. If a valid pipe latch configuration is found, and at least 4 of 9 drift chamber layers had signals, the inner 3 stereo

conditions. The time lag required to write data onto tape, along with the off-line computer time needed for event reconstruction sets the maximum trigger rate <8 HZ.

The advantage of triggering with this track definition is that the track finding efficiency is relatively insensitive to the drift chamber efficiency. For 95% chamber efficiency on each layer, the track finding efficiency for at least 4 out of 6 layers is 99.8%. Since only events with 2 tracks with $|\cos\theta| < 0.79$ are used in this analysis, the effect of the detector trigger on detection efficiencies is <1%, mostly due to pipe counter inefficiency. This represents a tremendous improvement over the Mark I triggering scheme and eliminates a major source of possible systematic error in the total cross section and inclusive momentum distribution measurements.

C. Tracking

To reconstruct charged tracks, combinations of 7 drift chamber hits are found that lie on a candidate track helix. Further hits falling within tolerances of the candidate track are added to the list of possible points. A chisquare criterion based on the measured spatial resolution is applied to define the track. Low momentum tracks are multiple scattered, so tracks below 100 MeV $p_\perp$ are excluded from consideration in all events. Further, about 20% of tracks with only 7 or 8 drift chamber points are lost to the chisquare criterion. For this reason, only tracks that

pass through 10 or more drift chamber layers ($|\cos\theta| < 0.79$) are included in the hadronic event sample. For tracks in this sample, the reconstruction efficiency in hadronic events is $\sim$98%, independent of multiplicity, as determined by a handscan of $\sim$600 hadronic events.

To construct an event vertex, tracks found by the above procedure are classified as primary or secondary, according to the value of the distance of closest approach to the beam axis (R_{min}). Primary tracks have $R_{min} \leq 0.15$ m and any z at R_{min}. All other tracks are classed as secondaries. The vertex is that point which minimizes the sum of the perpendicular distances to each primary track. In the χ^2 minimization procedure, weights are assigned based on individual track fits, taking into account position resolution and multiple scattering. The vertex distributions in radius and z of a random sample of events are shown in Figures 45 and 46. The vertex distributions have tails at large z due to interactions of the beam with residual vacuum chamber gas, and at large r due to interactions in the beam pipe and pipe counters.

For annihilation events, the track fits and hence the momentum resolution were improved by constraining all tracks to a common vertex position and refitting them. The transverse position of the interaction region is measured in elastic scattering events with a precision of $\lesssim$.5 mm in x and y. If the vertex radial position is less

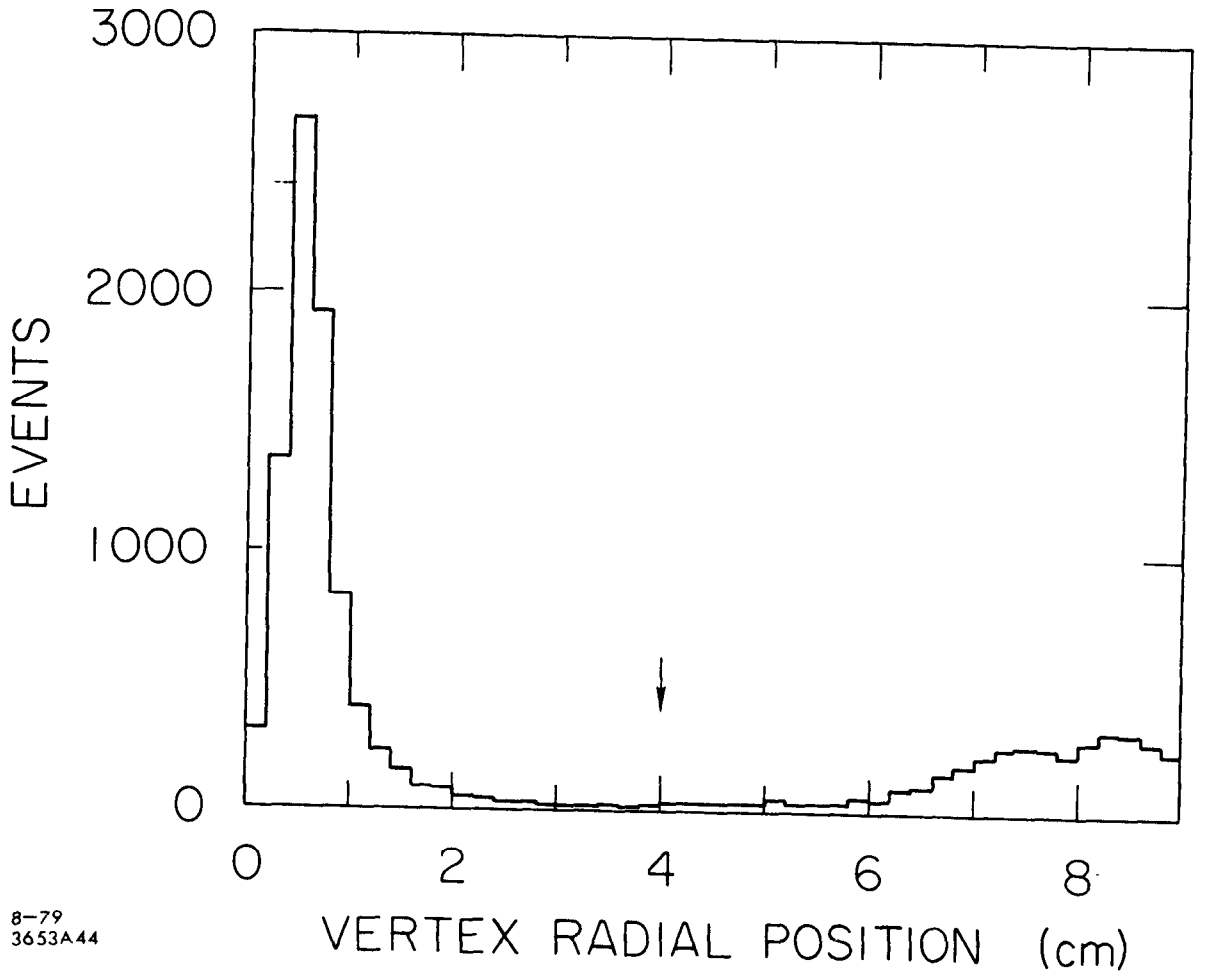

Fig. 45. Radial distribution of event vertices. The arrow marks the vertex radius cut for hadronic event definition.

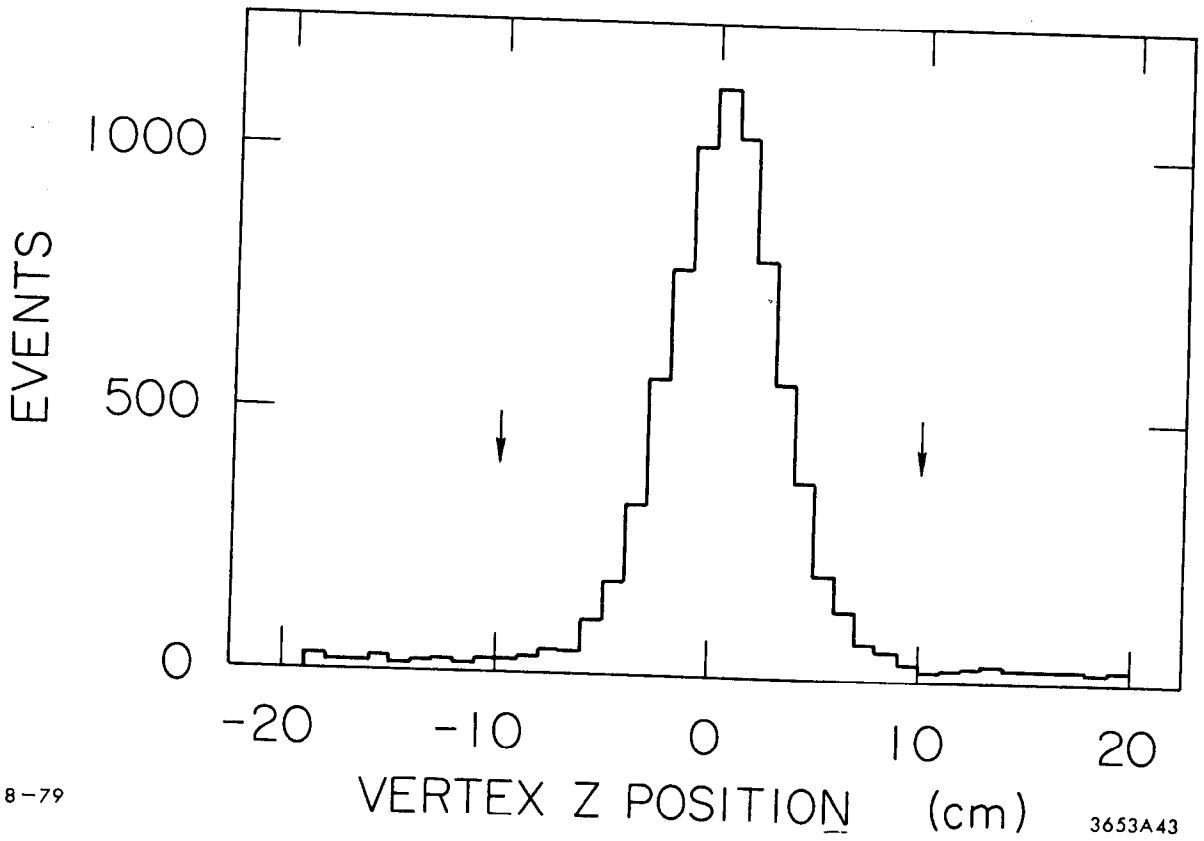

Fig. 46. Z distribution of event vertices with vertex radius < 4 cm. The arrows mark the boundaries of the hadronic signal region.

than 4 cm, then all tracks with R_{min} within 1.5 cm of the interaction point and z at R_{min} within 15 cm of the interaction point are constrained to the crossing point with the remaining tracks reclassified as secondaries. The resulting rms momentum resolution for primary tracks is

$$\delta_{p/p} \simeq \left[\left(0.005 \times p(\text{GeV})\right)^2 + (0.0145)^2\right]^{\frac{1}{2}} \quad .$$

VII. EVENT SELECTION, LUMINOSITY MEASUREMENT, AND DETECTION EFFICIENCY FOR THE MARK II DETECTOR

The analysis procedures used for the Mark II data are quite similar to those used for the Mark I data. Events are selected by requiring a vertex be found with $r < 15$ cm and at least two charged tracks be found, with at least one charged track having $|\cos\theta| < 0.65$. About 15% of the events logged on tape during colliding beam running are hadronic events, about 20% are elastic scatters or muon pairs, and the remainder are background events. Cosmic rays are eliminated from further consideration as in the Mark I analysis (Section III).

A. Hadronic Event Selection

Hadronic events are selected from the remaining event sample by requiring three or more prongs in the event or two prongs in the event provided that the azimuthal angle between the tracks is greater than 20° and less than 160°, the tracks have opposite charges, and have momenta >300 MeV. As in the Mark I (Section III.A), the momentum and coplanarity cuts in the two prong sample reduce contamination from elastic scatters, muon pairs, and two photon exchange processes. In addition, electrodynamic contamination from Bhabha events was removed in the 2, 3 and 4 prong event sample with the following procedure. Electron tracks were identified by pulse height in the liquid argon;[46] 2 and 3 prong events were removed if any track was identified

as an electron and 4 prong events were removed if at least 2 tracks were identified as electron. Additional cuts were made in events containing tracks with $x > .7$.[47] A visual scan containing some 600 hadronic events was performed, and, from the results, we estimate <4% of hadronic events are misidentified or lost.

B. Backgrounds

After passing the above cuts, the remaining hadronic event sample contains background events from beam-gas and beam-wall interactions, the two-photon processes $e^+e^- \to e^+e^-e^+e^-$ and $e^+e^- \to e^+e^-\mu^+\mu^-$, and heavy lepton decays. These background events are removed by the same methods used in the Mark I analysis (Section III.B).

Events from beam wall collisions are eliminated by imposing a vertex position cut, $r < 4$ cm. We estimate 5±3% of annihilation events are lost due to this cut. Vertices with $/Z/ < 10$ cm are called beam-beam events, with beam-gas background determined from the regions $10 < /Z/ < 15$ cm. To remove this background ($\lesssim$3% of events) distributions in multiplicity and momentum were formed from the signal and background z regions, and the distributions subtracted.

The remaining two-photon background is removed from the detected event sample as in the Mark I analysis, with account taken of the improved trigger efficiency (<2% of hadronic events). The τ background is again removed by

Monte Carlo calculation (<10% of events), with improved parameters shown in Table 8.

C. Bhabha and Muon Pair Events

Events from the reactions $e^+e^- \rightarrow e^+e^-$ and $e^+e^- \rightarrow \mu^+\mu^-$ are separated with the criteria that there be only two tracks, oppositely charged, with flight times equal to ±3 nsec, collinear to ≤10°, momenta $\geq E_{cm}/4$, $|\cos\theta|$ of the positive track <0.65, and the ϕ for both tracks projected into the shower modules must be more than 40 mrad from a crack between modules. Separation of Bhabha from muon pair production events is accomplished by liquid argon counter pulse height data. As shown in Figure 47, a cut at sum of pulse heights equal to 0.8 separates ee and μμ final states. The cut is asymmetrically placed to ensure no contamination of μμ events by Bhabhas during those runs when one of the shower modules was not working.

The time integrated luminosity measurement is the ratio of the number of Bhabha scattering events detected in the range $|\cos\theta| < 0.65$ to the calculated detected cross section.[48] As in the Mark I (Section III.C), the Bhabha luminosity measurement is checked against the luminosity measured from muon pairs ($|\cos\theta| < 0.65$) and a luminosity monitor counter array centered at 22 mrad from the beam line.

Detected cross sections are calculated with the input data being the cosθ range, momentum and collinearity cuts,

TABLE 8

MONTE CARLO PARAMETERS USED FOR CALCULATION OF THE EXPECTED NUMBER OF DETECTED τ DECAY EVENTS

(Mark II)

Mass	1.78 GeV
Branching Fractions	
$\tau \rightarrow e\nu\nu$	.164
$\mu\nu\nu$	.160
$\pi\nu$	.104
$\rho\nu$	.230
$A1\nu$	.093
Continuum ν	.249

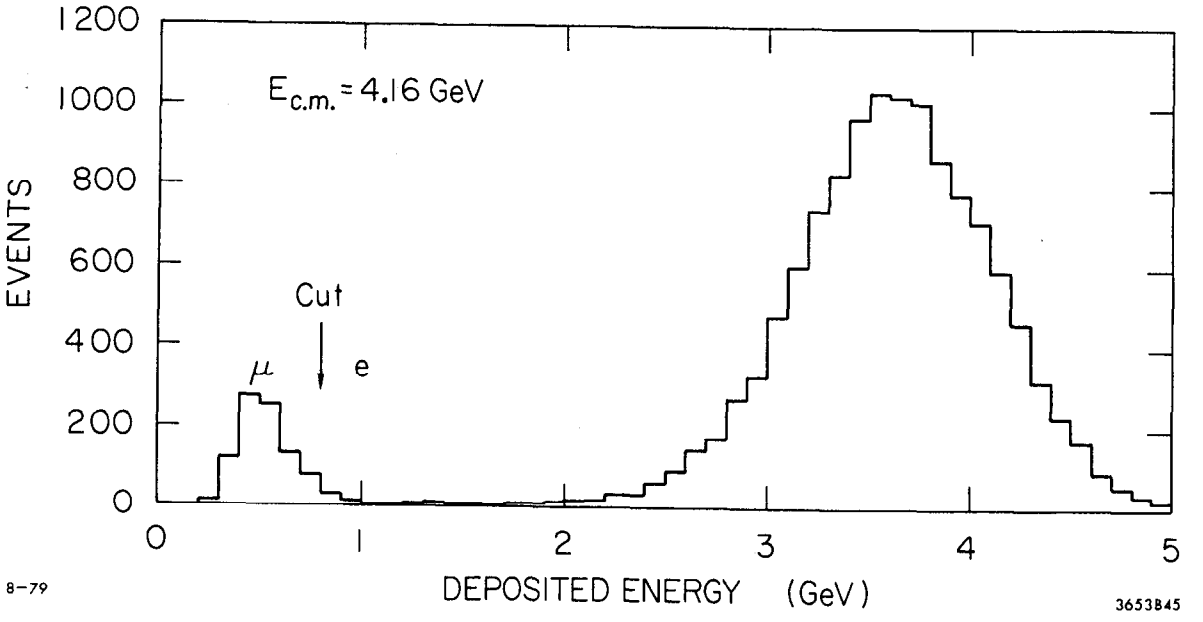

Fig. 47. Sum of pulse heights distribution for ee and μμ final states.

rms beam bunch length, and the amount of external radiator (.065 radiation lengths). The detected angular distribution of Bhabha events is fitted within the range $|\cos\theta| < 0.65$ with overall normalization determined by the number of Bhabha events (Figure 48). Then, to check the event selection procedures, we fit the $\mu\mu$ angular distribution with normalization determined from the number of Bhabha events (Figure 49). Within statistical errors, the luminosity measured from the muon pair events agrees with the Bhabha measurement, at all energies. Although the luminosity monitor is much improved in the Mark II as compared with the Mark I (systematic error ±6%), it is still used only to provide a continuous on-line relative normalization for evaluating performance of the apparatus and storage ring.

As in the Mark I, Bhabha events are chosen to set the normalization because their measurement provides the smallest systematic and statistical errors of the three methods of luminosity measurement. The systematic uncertainty in the Bhabha integrated luminosity measurement is estimated to be ±4.5%.

D. Raw Yields

Figures 50 and 51 give for a random hadronic event sample the observed number of tracks as a function of $\cos\theta$ and ϕ, and demonstrate the 2π angular acceptance in ϕ and 0.79 acceptance in $|\cos\theta|$.

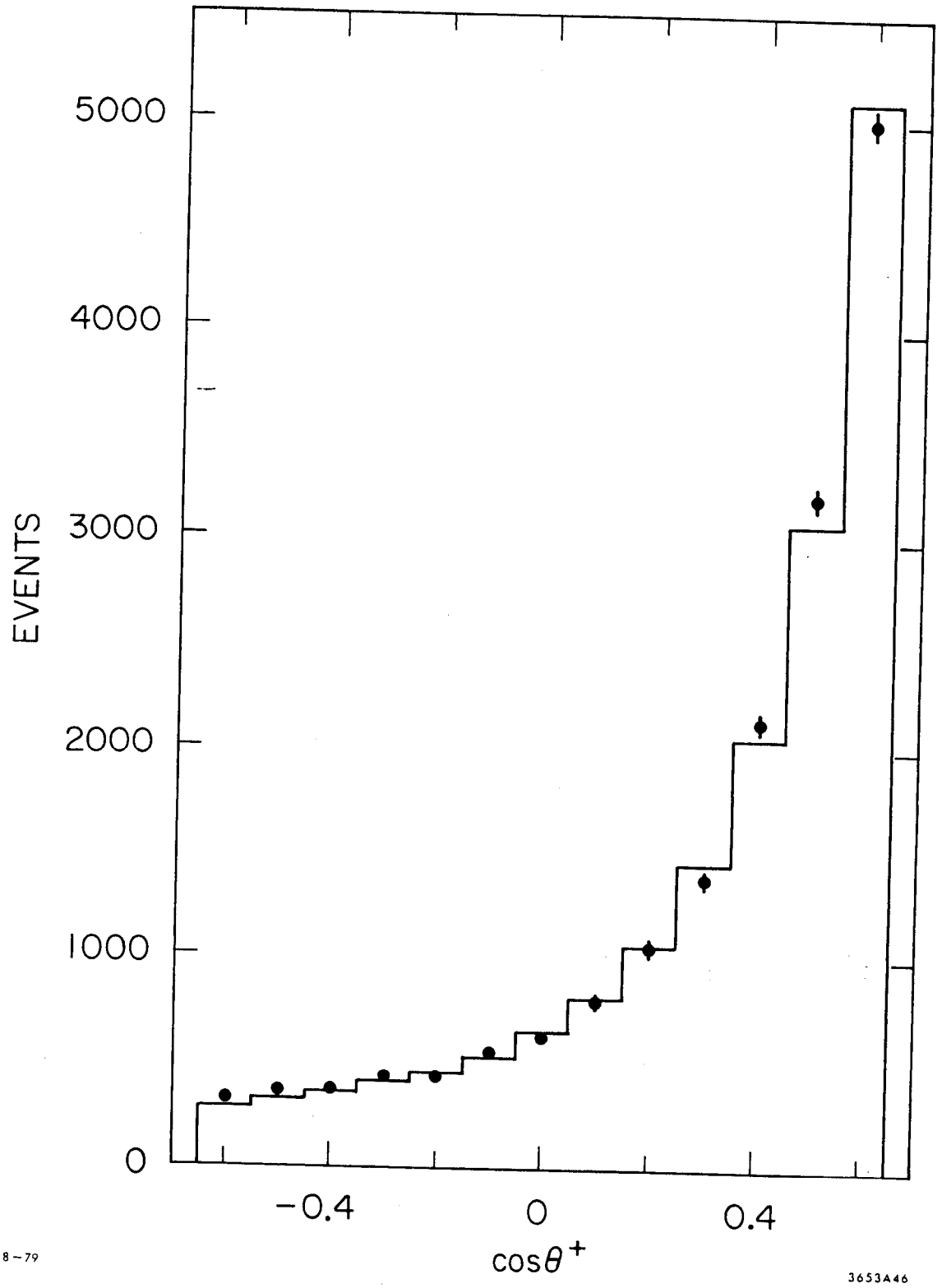

Fig. 48. Angular distribution of Bhabha event positive tracks. The histogram is the QED prediction.

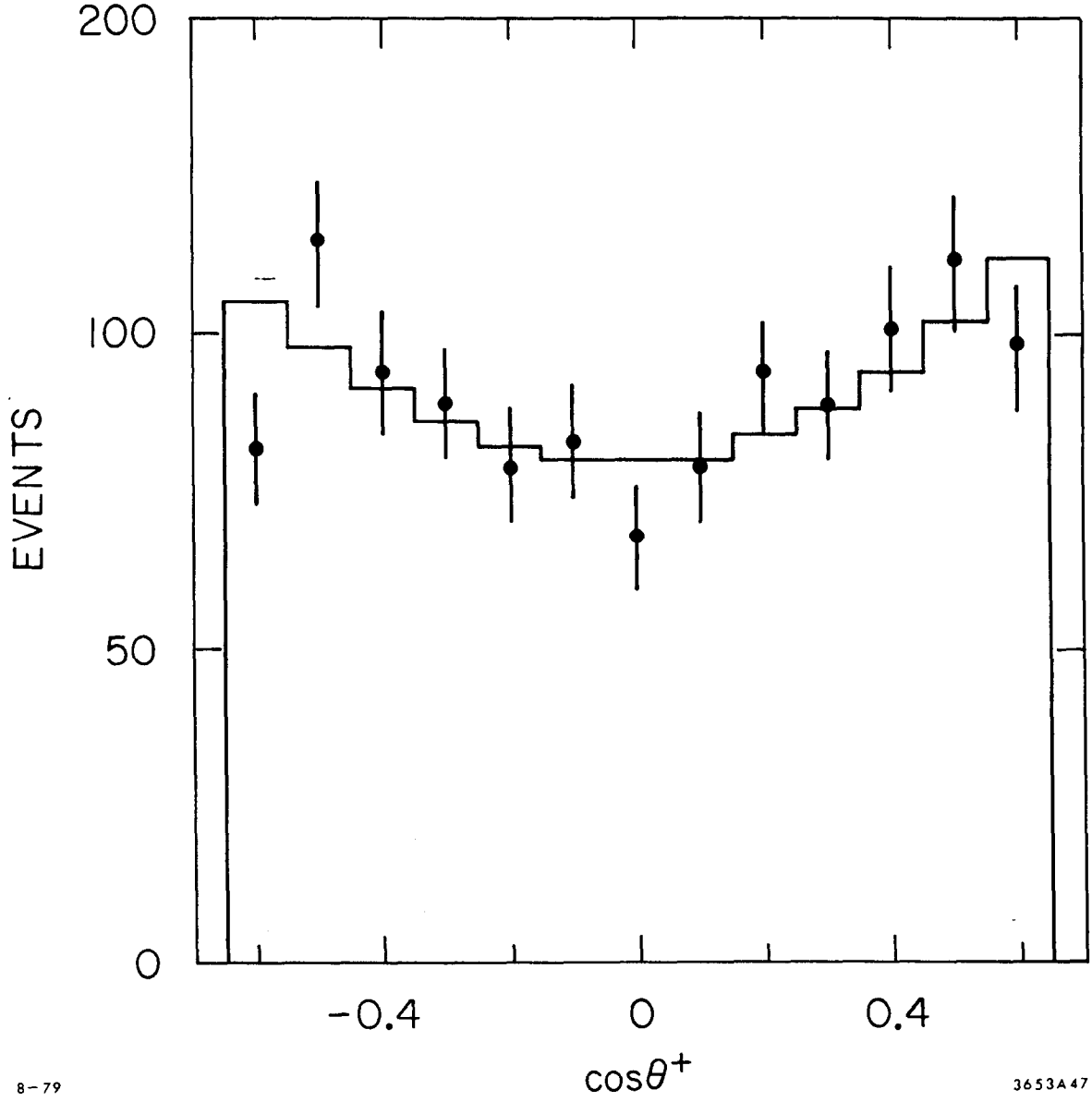

Fig. 49. Angular distribution of positive tracks from μμ events. The histogram is the QED prediction, with normalization set by the number of Bhabha events.

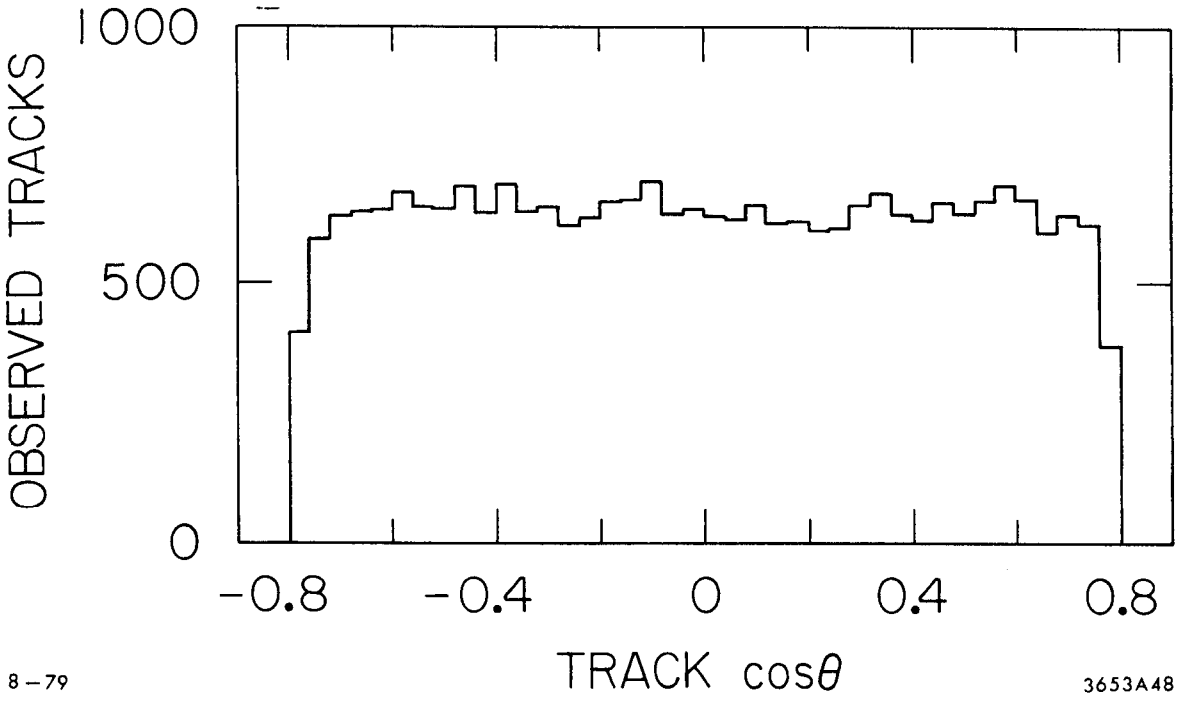

Fig. 50. Observed number of hadronic tracks versus track cos(θ).

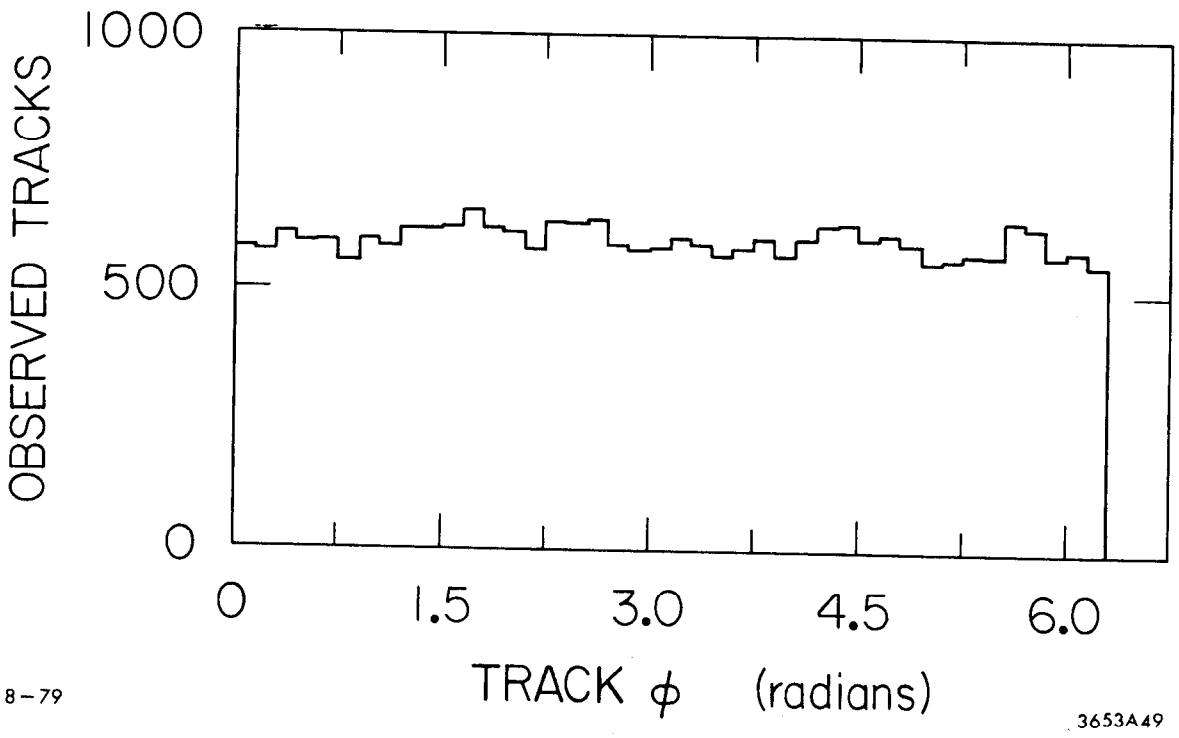

Fig. 51. Observed number of hadronic tracks versus track ϕ.

Figures 52 to 55 display various distributions taken directly from the hadronic event sample with no efficiency correction factors applied and show the general trends in the raw data. Figures 52 and 53 give the observed charged particle multiplicity distributions at several energies, and the mean observed charged multiplicity as a function of energy. The mean values are lower than in the Mark I (Figure 16) because of the increased detection efficiency in the lower multiplicities in the Mark II. Figure 54 displays the observed yield of hadronic events. The data indicate peaks near 4.1 and 4.4 GeV, as seen in the previous experiments. Figure 55 gives for ≥ 3 charged prong detected hadronic events the observed single particle x distribution. The observed inclusive momentum distribution again shows a steep decrease with increasing x. As in the Mark I, some of the variation of the total hadronic yield with energy and of the inclusive single particle yield with track momentum is a result of the dependence of the detection efficiency on the total center-of-mass energy and individual particle momenta.

E. Detector Efficiency

The same techniques used in the Mark I analyses (Section IV) for detector efficiency determination have been applied to the Mark II analysis. The only difference is that since there are so little data, no spline fits to the

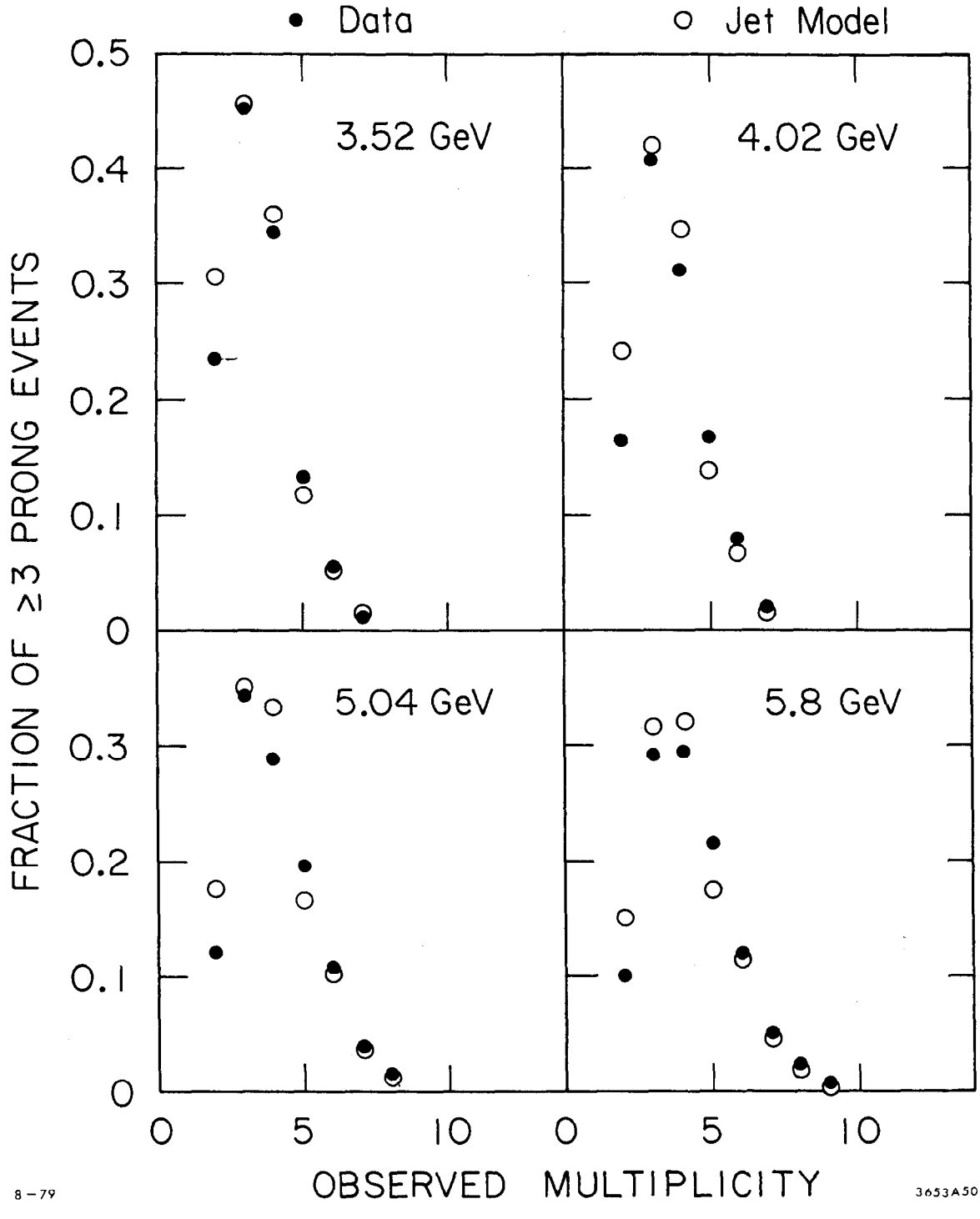

Fig. 52. Observed charged multiplicity fractions for hadronic events, with all backgrounds removed, normalized to the number of >2-prong events. The open circles are the jet model predictions.

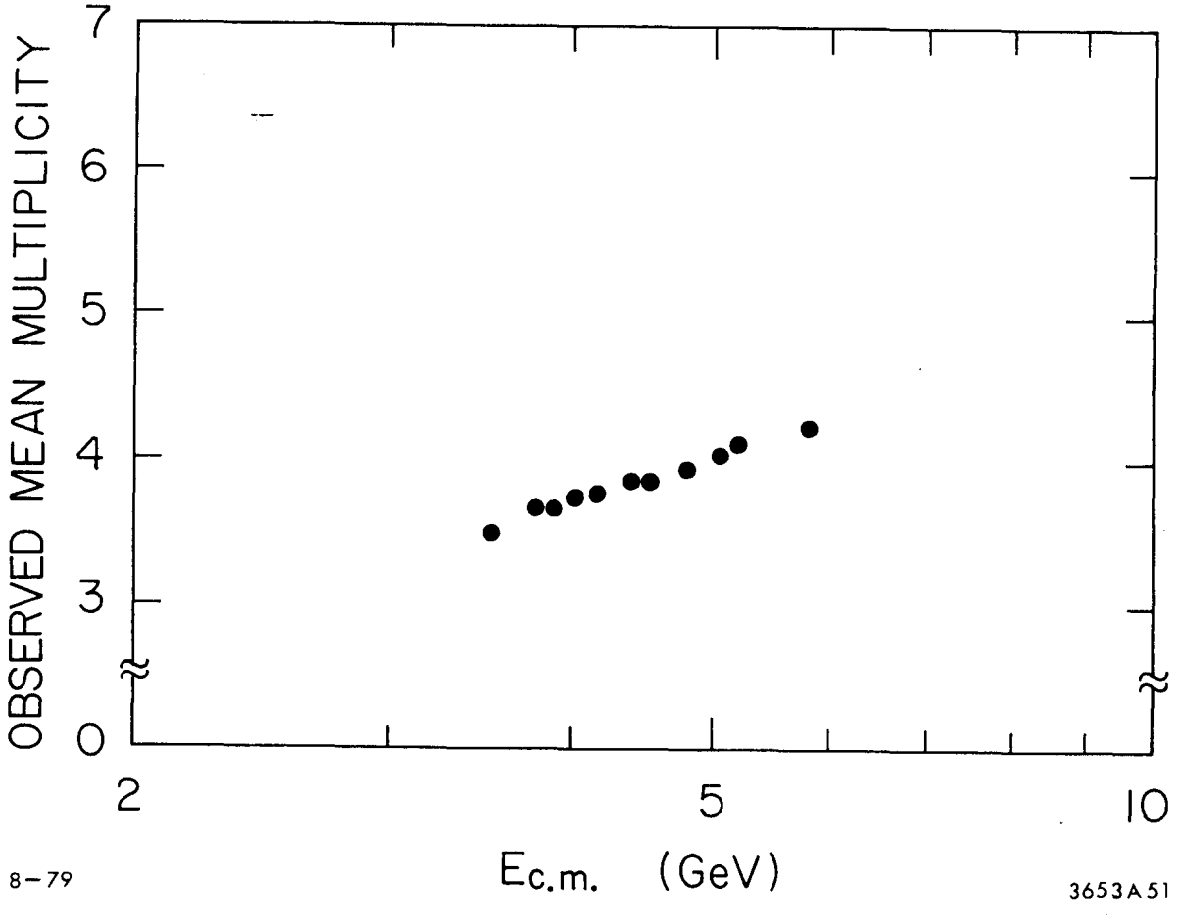

Fig. 53. Observed mean charged multiplicity for hadronic events versus center-of-mass energy.

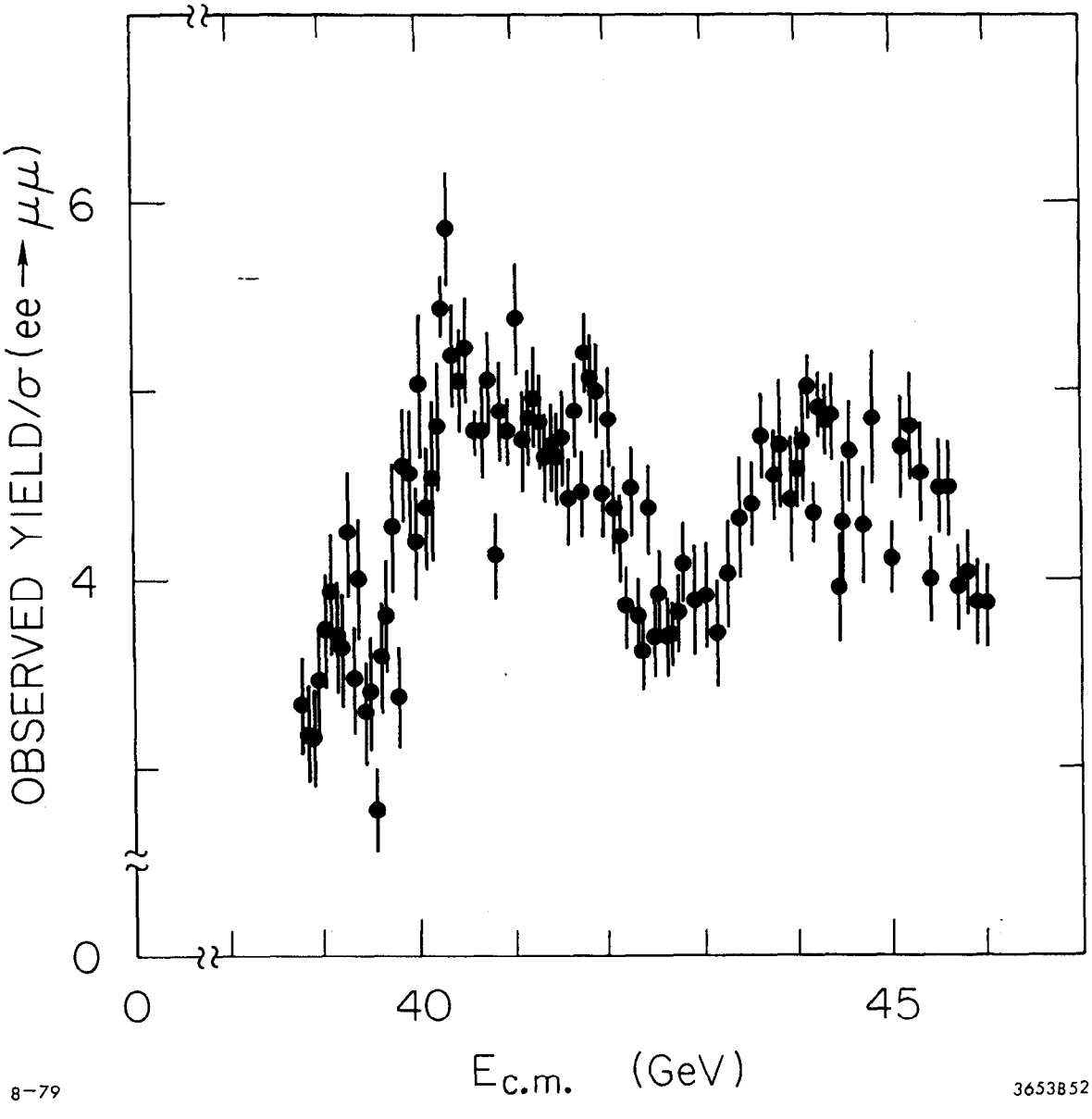

Fig. 54. Observed hadron yield corrected with the jet model efficiency determined without radiative corrections and divided by the muon pair-production cross section versus E_{cm}. Compare with Mark I, Figure 22.

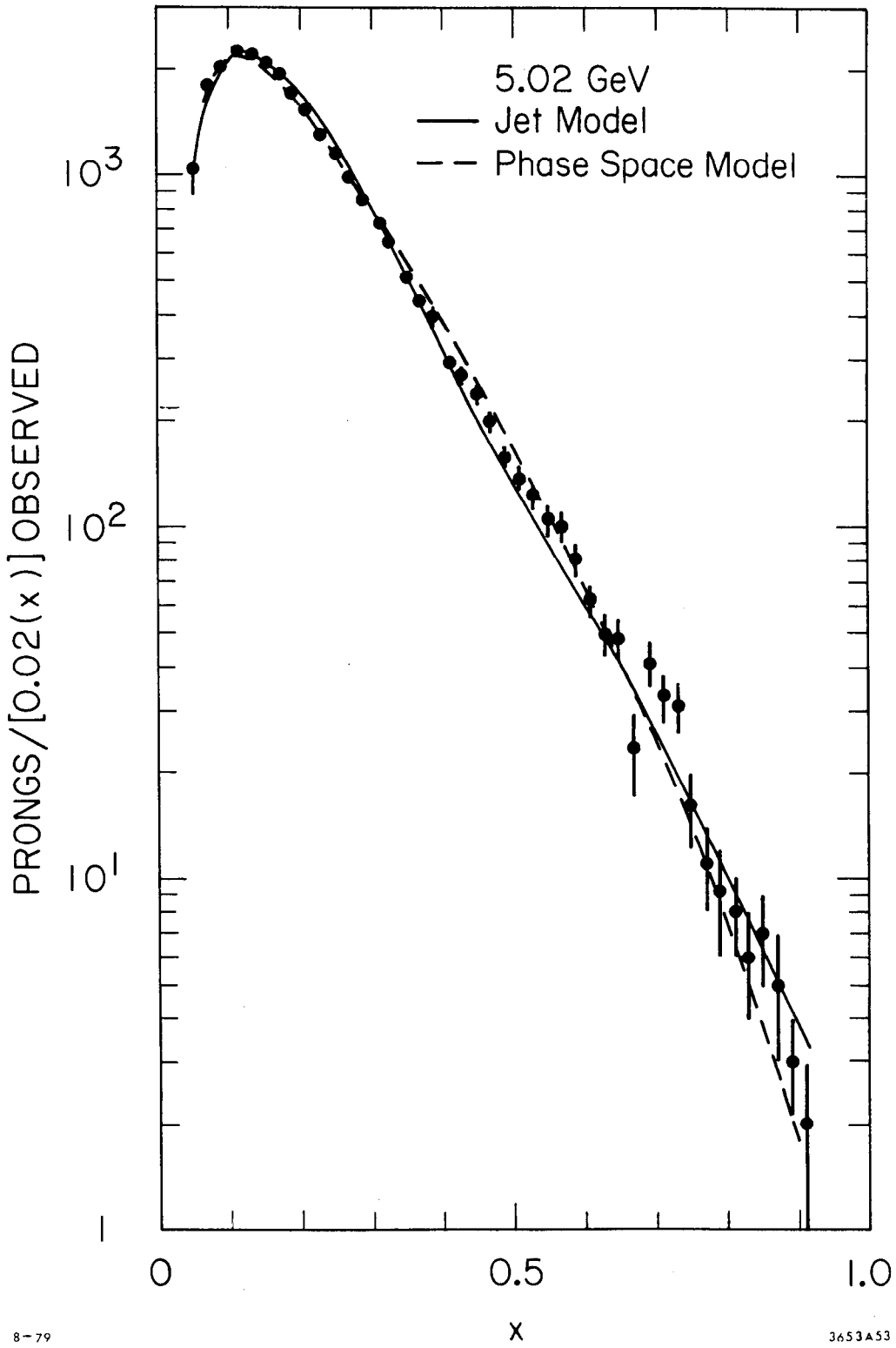

Fig. 55. Observed single particle x distribution for events with three or more detected charged particles for E_{cm} = 5.04 GeV along with the phase space and jet model predictions.

$\tilde{\varepsilon}_{qp}$ matrix elements were performed. Monte Carlo simulations were run at each energy where unfolds were performed.

The detector simulation again includes all aspects of the detector performance. The same production model parameters used in the Mark I analyses were found to fit the Mark II detected distributions. Figures 52 and 55 show comparison of the observed multiplicity and momentum distributions in the data and the jet model. The Mark I parameters provide an acceptable fit.

The production model dependence of $\bar{\varepsilon}$ and the $\tilde{\varepsilon}_{qp}$ is reduced to ±4.5% and ±10%, respectively, in the Mark II. Figure 56 displays the $\tilde{\varepsilon}_{02} \rightarrow \tilde{\varepsilon}_{08}$ matrix elements for comparison with the Mark I results and the hand calculation of Appendix I. The Mark II detection efficiency is greater than that of the Mark I and the matrix elements vary more slowly with energy.

Figure 57 gives $\bar{\varepsilon}$ values determined from the unfolds of a restricted sample of the data. Note that the energy dependence of $\bar{\varepsilon}$ is considerably smaller in comparison with Figure 27. This largely results from the higher detection efficiency of the low multiplicity events in the Mark II as compared to the Mark I. The smooth curve in Figure 57 is used to interpolate $\bar{\varepsilon}$. Figure 58 gives the single particle inclusive momentum detection efficiency, $\varepsilon(x)$, vs. x. The Mark II has a higher detection efficiency than the Mark I

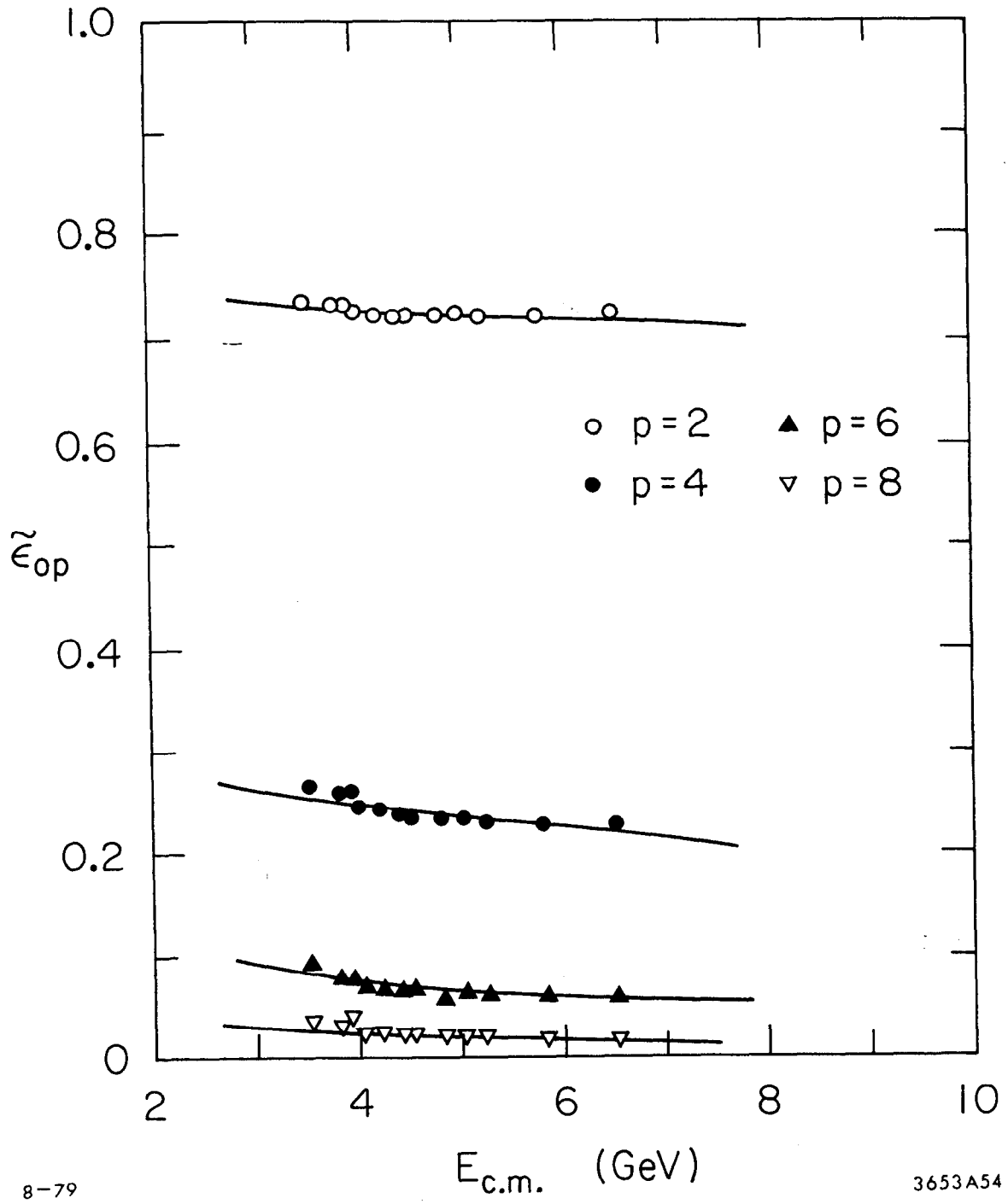

Fig. 56. Detection efficiency matrix elements $\tilde{\epsilon}_{02} \rightarrow \tilde{\epsilon}_{08}$ versus E_{cm}. These elements are the probabilities of completely missing a 2, 4, 6, or 8 produced charged prong event, respectively. They are defined by $\tilde{\epsilon}_{op} = 1 - \sum_i \tilde{\epsilon}_{ip}$. These elements should be compared with those of the Mark I (Figure 26).

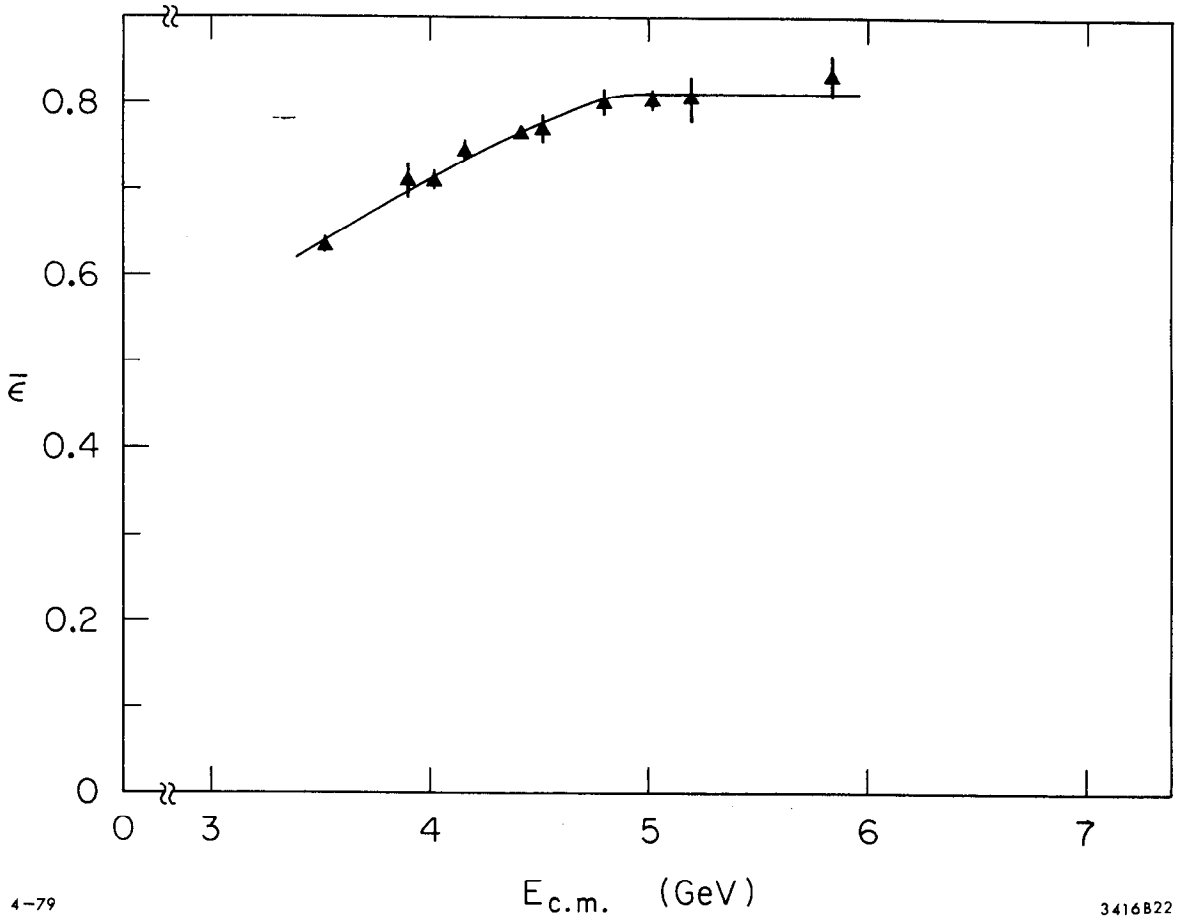

Fig. 57. Effective hadronic detection efficiency $\bar{\epsilon}$ (Equation 4.8) versus E_{cm}. The curve is used for interpolation.

due to the increased solid angle and better triggering efficiency. As in the Mark I, the accuracy with which $\varepsilon(x)$ can be determined ($\pm 8\%$) dominates the systematic uncertainties in the inclusive momentum spectra.

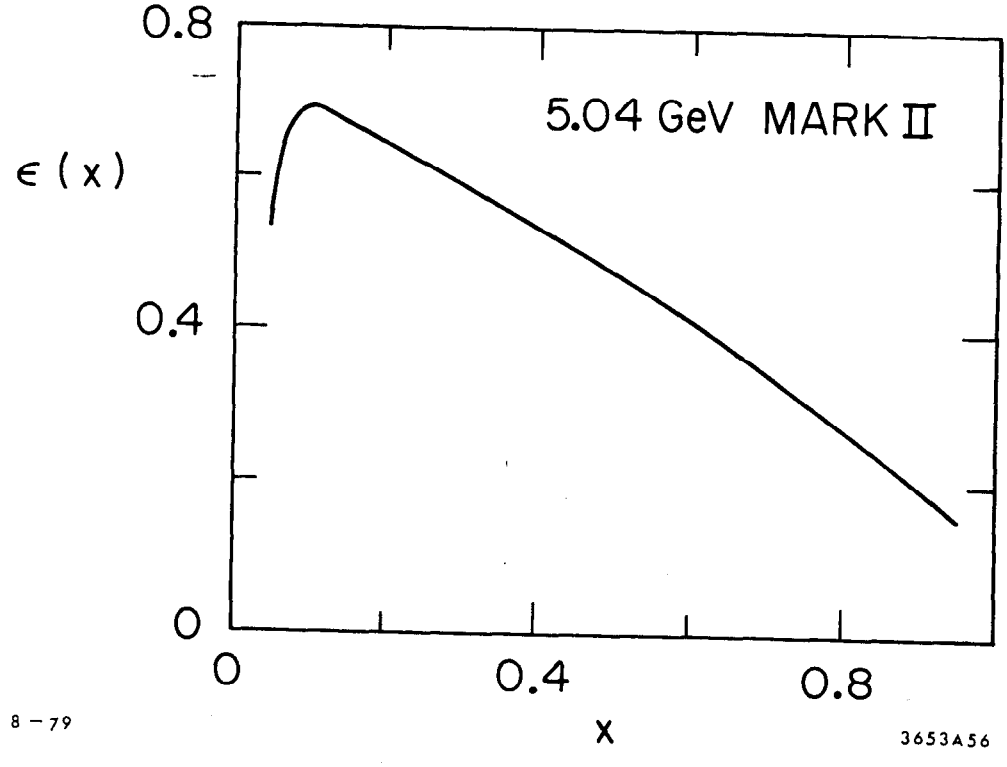

Fig. 58. Single particle inclusive detection efficiency, $\varepsilon(x)$, versus $x = 2p/E_{cm}$ for 5.04 GeV.

VIII. PRELIMINARY RESULTS

A. Total Annihilation Cross Section and Inclusive Momentum Distributions

Figure 59 shows preliminary values of R as a function of energy for the Mark II data. The error bars shown are statistical only. There are possible additional overall and point-to-point systematic errors. From the estimated uncertainty in the luminosity (±4.5%), event selection procedures (±4.6%), and detector efficiency determination (±4.5%), we expect the overall possible systematic uncertainty is ±8%. We expect any additional smooth variation from the highest energy to the lowest is <3%. The point-to-point systematic fluctuations are estimated to be ±4%.

The data of Figure 59 are in good agreement with the Mark I measurement (Figure 29). The energy region from 4.6 to 5.9 GeV was not well covered by the Mark I measurements. The Mark II data in this region smoothly interpolate from the structure at 4.4 GeV to the scaling region above 5.5 GeV. Below 4.6 GeV, the Mark I and Mark II data show the same structure, within errors. Some evidence is seen in the Mark II data for a structure near 4.18 GeV as reported by the DASP[49] collaboration.

Figure 60 shows as a function of energy the produced mean charged multiplicity inferred from the unfold results. These measurements are in good agreement with Mark I results, within the systematic errors (±2.5%).

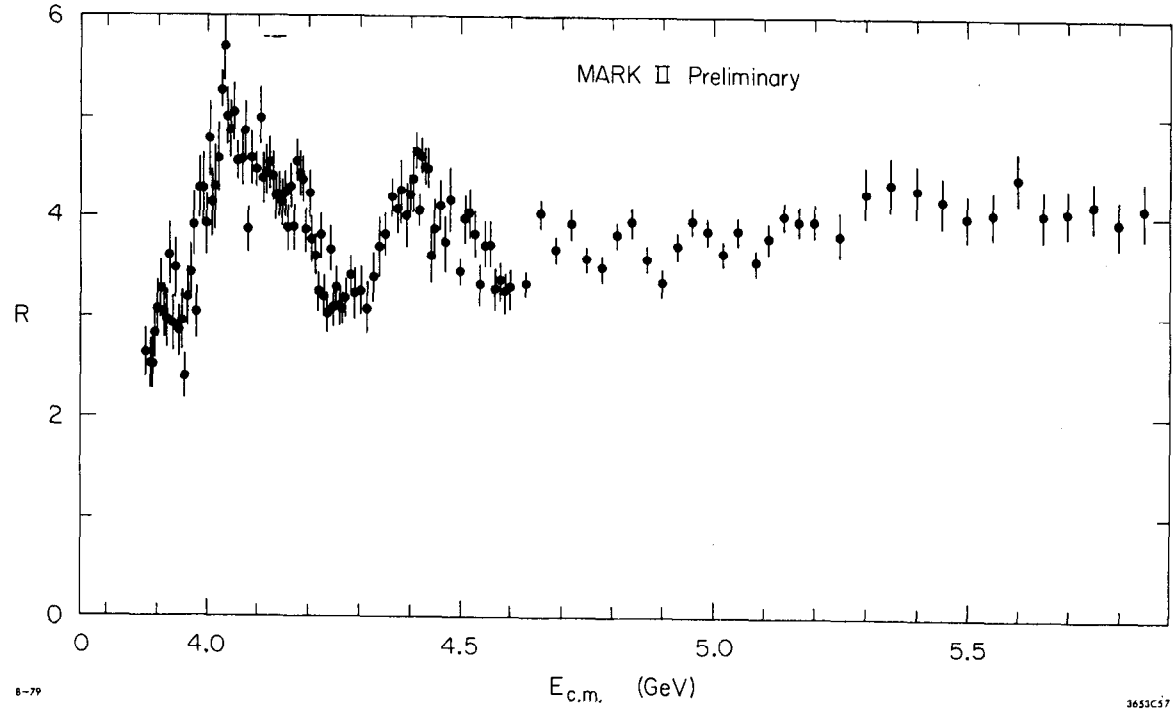

Fig. 59. The ratio $R = \sigma(e^+e^- \rightarrow \text{hadrons})/\sigma(e^+e^- \rightarrow \mu^+\mu^-)$ versus E_{cm}.

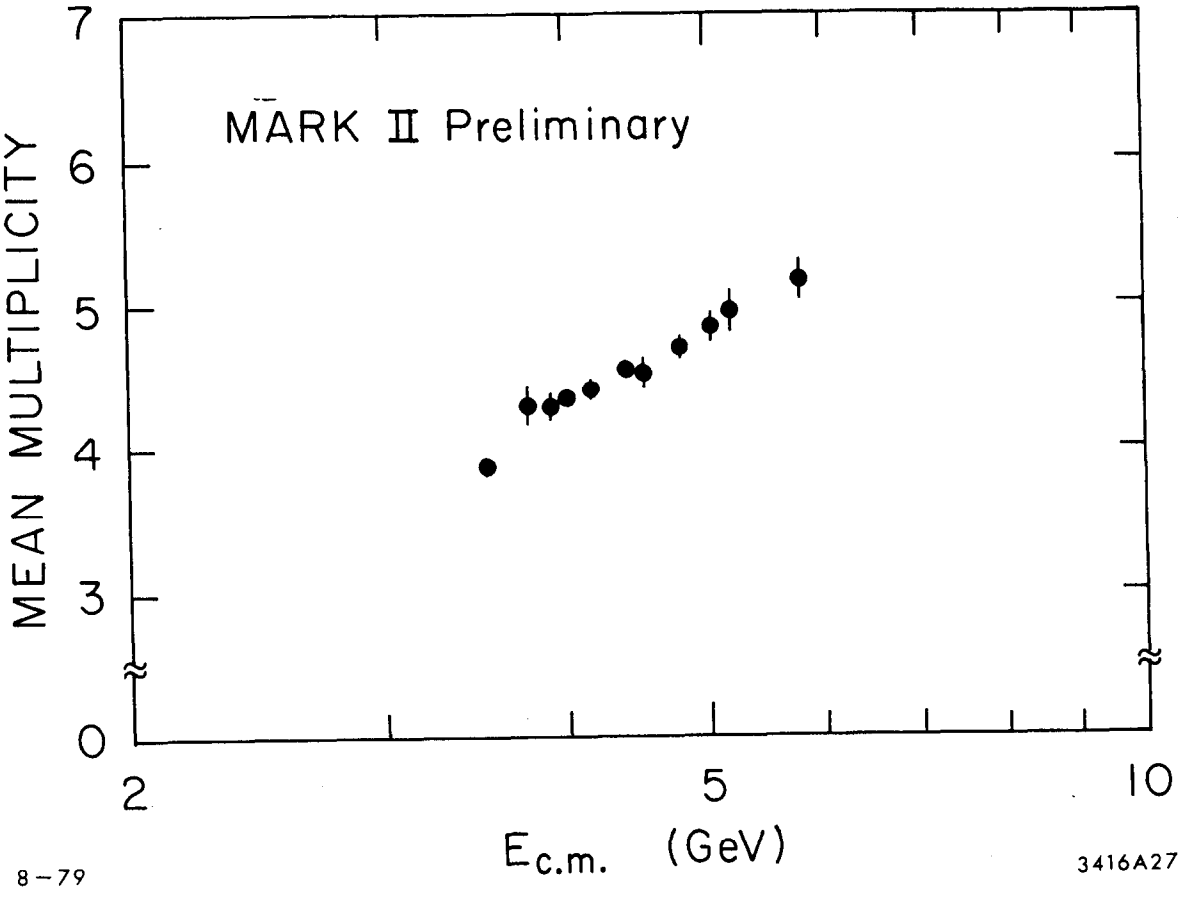

Fig. 60. Mean produced charged multiplicity versus E_{cm}.

Figure 61 displays the $s\frac{d\sigma}{dx}$ distributions measured at 5.04 and 5.68 GeV with the Mark II. The errors indicated are statistical only. These curves are subject to a possible systematic uncertainty of ±10% at the highest and lowest x values, with smooth variation across the range of x. Again the region $x > 0.8$ is particularly subject to possible systematic errors from the non-Gaussian tails of the momentum resolution at high x, and from the possibility of leakage of QED events into the hadronic event sample. The inclusive momentum distributions of Figure 61 are in good agreement with the previous measurements.

B. Improvement of these Results

These results have been labelled "preliminary" because the full power of the Mark II detector has not been utilized. In particular, no use has been made of the neutral particle detection of the liquid argon shower counters. These counters and the neutrals which they detect may allow, for instance, a looser cut in the two-prong event sample for elimination of the two-photon contamination. In addition, these counters will enable us to determine neutral particle momentum spectra, although with lower efficiency than that of the charged spectra. Information available in the endcaps for improvement of the charged particle tracking solid angle has not yet been utilized. Finally, the particle identification capabilities of the time of flight, shower counter, and muon systems and the secondary

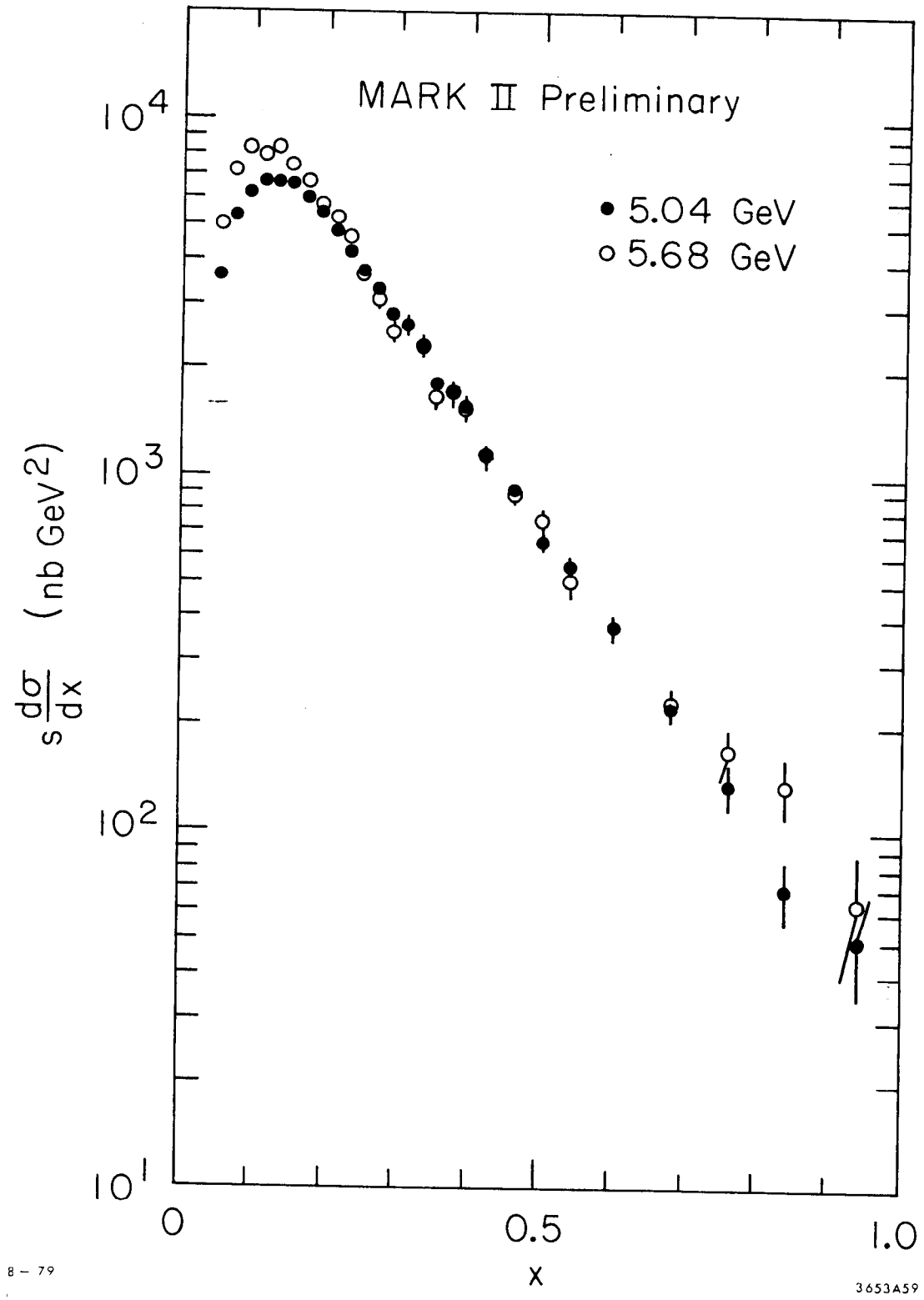

Fig. 61. Corrected single particle inclusive x distribution versus x.

vertex recognition capabilities provided by the drift chamber have not been used to determine the inclusive momentum spectra of the various different particles.

The single charged particle events were not used in this analysis. The combination of beam-gas, two-photon, and Bhabha events with only one prong reconstructed severely contaminates the one-prong event class; the observed number of events exceeds the Monte Carlo prediction by an order of magnitude. This problem precluded use of the one prong events in this preliminary analysis. A great deal of work remains to be done before the capabilities of the Mark II detector will be fully utilized.

IX. CONCLUSIONS

Excluding the narrow resonances ψ, ψ', we have observed three distinct regions of structure in R in the center-of-mass energy range 2.6 to 7.8 GeV. The first is a scaling region below 3.7 GeV where R is constant with value 2.7±0.5. In the region $3.7 < E < 5.5$ GeV, R has a complicated energy dependence with distinct maxima at 3.77 and 4.4 GeV and with an additional complicated transition region between 3.9 and 4.3 GeV. Above 5.5 GeV R is again constant with value 4.3±0.4. Aside from the narrow resonances ψ, ψ', no additional narrow resonances have been found, with upper limits summarized in Table 9. This upward step in R has been widely interpreted as evidence of the opening of new hadronic degrees of freedom in the form of the production of "charmed" quarks. In fact, the upward step (1.6±0.3) is about 15% larger than the value 4/3 one would expect in a naive quark model although the naive model prediction is within the systematic uncertainty. The value of R for $E > 5.5$ Gev is 30% larger than the naive model predicts (10/3), and that is outside the expected experimental systematic error. The observed structure in R qualitatively supports a quark-parton model for strong interactions.

For $x > 0.3$, the inclusive momentum distributions $s\frac{d\sigma}{dx}$ scale. The distributions are approximated by the form $ce^{-\beta x}$ for $x > 0.3$, with

$$\beta = 6.8 \pm 0.3 \quad \text{and} \quad c = 2 \pm 0.3 \times 10^4 \ .$$

The systematic errors and restricted Q^2 range of these measurements preclude any study of possible scaling violations as, for instance, predicted by QCD. The scaling of the inclusive distributions and the magnitude of and presence of scaling regions in R provide confirmation of the quark-parton hypothesis.

TABLE 9

Results of the Search for Narrow Resonances. Upper Limits (90% confidence level) for the Radiatively Corrected Integrated Cross Section of a Possible Narrow Resonance. The Width of this Resonance is assumed to be Small Compared to the Mass Resolution.

Mass Range (GeV)	Limit on $\int \sigma_H \, dE_{cm}$ (nb MeV)
3.20 → 3.50	970
3.50 → 3.68	780
3.72 → 4.00	850
4.00 → 4.40	620
4.40 → 4.90	580
4.90 → 5.40	780
5.40 → 5.90	800
5.90 → 7.60	450

APPENDIX I

Hand Calculation of ε_{qp}

A simple hand calculation of the ε_{qp} will show the important contributions to the detector inefficiencies. If we let r = the fraction of solid angle within which tracks are not observed, and P = the probability of detecting a track in the detector, then, if tracks are produced isotropically in θ and ϕ,

$$\varepsilon_{qp} = \frac{p!}{q!\ (p-q)!}\ r^{p-q}\ p^{q}\ . \qquad (A.1)$$

Further, if s = the probability that a track be in the solid angle of the detector and make a TASH, and t = the probability that a track be in the detector but not TASH, then r+s+t = 1 and

$$p^{q} = \begin{array}{l}(\text{Probability of q tracks in the}\\ \text{detector}) - (\text{probability of only}\\ \text{one TASH}) - (\text{probability of no TASH})\end{array}$$

$$p^{q} = (s + t)^{q} - qst^{q-1} - t^{q}\ .$$

Substituting into A.1 and simplifying,

$$\varepsilon_{qp} = \frac{p!}{q!(p-q)!}\, r^{p-q}(s+t)^{q}\ \left(1 - \frac{t^{q}}{(s+t)^{q}}\ [1+q(s/t)]\right).$$

Since the average measured TASH efficiency is $s/(s+t) \equiv \tau$, and s+t = 1-r, we have

$$\varepsilon_{qp} = \left\{ \frac{p!}{q!(p-q)!} \; r^{p-q}(1-r)^{q} \right\} \left(1-q\tau(1-\tau)^{q-1}-(1-\tau)^{2} \right). \qquad (A.2)$$

From A.2, we see that the probability that q charged prongs are detected of the p charged prongs produced is given by the probability that q charged prongs land within the acceptance of the detector (the factor inside { }), multiplied by the probability that at least two of those q prongs will cause a TASH to occur.

Table 10 shows the elements ε_{qp} for p up to 8 prongs, not modified by the effect of the TASH, calculated for the Mark I ($r \sim 0.35$). Note that the ε_{op} elements are the probabilities that an event with p prongs produced is completely missed. Table 11 shows the ε_{qp} as given by the complete expression A.2. In Table 11 the quantity τ, the average TASH efficiency, is the TASH efficiency from Figure 8 evaluated at momentum given by $E_{cm}/2p$. Comparing the ε_{op} elements in Tables 10 and 11 shows that the TASH requirement causes a sizable inefficiency even for high multiplicity events at high energy. Furthermore, within this model we expect that the inefficiency becomes worse at lower energies, giving an energy dependence to our efficiency matrix elements. Table 12 shows for comparison the ε_{qp} values obtained by Monte Carlo calculation, for the Mark I.

Table 13 is the detection efficiency matrix evaluated for the Mark II detector, r = .21. Here we retain only the term inside { } of Equation A.2, since the triggering of the detector is a negligible contribution to the detection inefficiency. Table 14 shows for comparison the $\tilde{\varepsilon}_{qp}$ values obtained by Monte Carlo calculation for the Mark II. Comparison of Tables 11-14 shows that the jet model angular distribution and the restrictive cuts in the two-prong event sample cause additional inefficiency over that of the isotropic distribution assumed for this calculation.

This simple calculation clearly illustrates that the trigger requirement of two TASHing charged tracks is a severe one, causing an overall decrease and an energy dependence in the average detection efficiency.

TABLE 10

DETECTION EFFICIENCY MATRIX FOR THE MARK I DETECTOR
(not modified by the TASH requirement)
Equation A.2

Prod / detected	2	4	6	8
0	0.58	0.13	0.01	0.0
1	0.0	0.0	0.0	0.0
2	0.42	0.31	0.10	0.02
3		0.38	0.24	0.08
4		0.18	0.33	0.19
5			0.24	0.28
6			0.08	0.26
7				0.14
8				0.03

TABLE 11

DETECTION EFFICIENCY MATRIX FOR THE MARK I DETECTOR

(Full Expression with TASH, Eq. A.2)

E_{cm} = 7.4 GeV

Prod / detected	2	4	6	8
0	0.62	0.24	0.08	0.03
1	0.0	0.0	0.0	0.0
2	0.38	0.22	0.06	0.01
3		0.36	0.22	0.07
4		0.18	0.32	0.18
5			0.24	0.28
6			0.08	0.26
7				0.14
8				0.03

TABLE 12

DETECTION EFFICIENCY MATRIX FOR THE MARK I DETECTOR

Jet Model Calculation, E_{cm} = 7.4 GeV

Prod / detected	2	4	6	8
0	0.83	0.44	0.20	0.09
1	0.00	0.0	0.0	0.0
2	0.09	0.04	0.01	0.0
3	0.05	0.25	0.14	0.05
4	0.03	0.22	0.24	0.14
5		0.04	0.25	0.23
6		0.01	0.13	0.25
7			0.02	0.16
8				0.06

TABLE 13

DETECTION EFFICIENCY MATRIX FOR THE MARK II DETECTOR

FROM EQUATION A.2

Prod / detected	2	4	6	8
0	0.38	0.03	0.0	0.0
1	0.0	0.0	0.0	0.0
2	0.62	0.17	0.02	0.0
3		0.41	0.09	0.01
4		0.39	0.26	0.05
5			0.39	0.16
6			0.24	0.30
7				0.33
8				0.15

TABLE 14

DETECTION EFFICIENCY MATRIX FOR THE MARK II DETECTOR

Jet Model Calculation, E_{cm} = 5.04 GeV

Prod / detected	2	4	6	8
0	0.73	0.24	0.06	0.02
1	0.0	0.0	0.0	0.0
2	0.23	0.11	0.03	0.0
3	0.03	0.37	0.18	0.06
4	0.01	0.26	0.30	0.16
5		0.02	0.29	0.25
6			0.14	0.27
7			0.01	0.18
8				0.06

APPENDIX II

Smoothing the Matrix Elements

In order to perform the spline fits on the matrix elements $\tilde{\varepsilon}_{qp}$, we used the following procedure.

First, the results of the Monte Carlo calculation, $\tilde{\varepsilon}'_{qp}$, for all elements were independently fit versus energy with either spline or linearized fits. The constraint of probability conservation was imposed at each energy:

$$\tilde{\varepsilon}_{on} = 1 - \sum_{\substack{i \\ i \neq o}} \tilde{\varepsilon}_{in} \quad . \tag{A.3}$$

To implement this condition, weights were assigned based on the statistical errors on the fits to the individual elements $\tilde{\varepsilon}'_{qp}$. We minimized the quantity

$$\chi^2 = \frac{(\tilde{\varepsilon}_{in} - \tilde{\varepsilon}'_{in})^2}{(\delta\tilde{\varepsilon}'_{in})^2} - \lambda(\Sigma \cdot \tilde{\varepsilon}_{in} - 1)$$

where $\tilde{\varepsilon}_{in}$ satisfies the constraint Equation A.3, and $\tilde{\varepsilon}'_{in}$ and $\delta\tilde{\varepsilon}'_i$ are determined by the independent fits. We have

$$\frac{\partial\chi^2}{\partial\tilde{\varepsilon}_{in}} = 0 = \frac{2(\tilde{\varepsilon}_{in} - \tilde{\varepsilon}'_{in})}{(\delta\tilde{\varepsilon}'_{in})^2} - \lambda$$

$$\rightarrow \quad \tilde{\varepsilon}_{in} = \frac{\lambda}{2} (\delta\tilde{\varepsilon}'_{in})^2 + \tilde{\varepsilon}'_{in}$$

or

$$\lambda = 2\left(\frac{1 - \Sigma_i \tilde{\varepsilon}'_{in}}{\Sigma_i (\delta\tilde{\varepsilon}'_{in})^2}\right)$$

and so

$$\tilde{\varepsilon}_{in} = \tilde{\varepsilon}'_{in} + \frac{(\delta\tilde{\varepsilon}'_{in})^2}{\Sigma_i (\delta\tilde{\varepsilon}'_{in})^2}\left[1 - \Sigma_i\, \tilde{\varepsilon}'_{in}\right] .$$

This equation gives from the independent fits $\tilde{\varepsilon}'_{in}$ the element $\tilde{\varepsilon}_{in}$ satisfying the constraint A.3 The Monte Carlo calculated points along with the curves for $\tilde{\varepsilon}'_{in}$ and $\tilde{\varepsilon}_{in}$ were plotted for each matrix element. Then the independent fits $\tilde{\varepsilon}'_{in}$ were adjusted to make the $\tilde{\varepsilon}_{in}$ smooth functions of energy and a good representation of the Monte Carlo calculation results.

APPENDIX III

Data Acquisition and Electronics Calibration in the Mark II at SPEAR

I. Aspects of e^+e^- Storage Ring Operation

The design of data acquisition systems for particle detectors at e^+e^- storage rings is constrained by several important aspects of storage ring operation. The beams are bunched, crossing in each experimental pit once every few μsec (780 nsec at SPEAR, 2.2 μsec at PEP). Advantage can be taken of this time structure by operating the detection apparatus synchronously with the beam crossing. Data taking is regularly interrupted by periods of beam injection ($\sim$ once every 2-4 hours) to make up for beam loss. Such periods can be used for hardware checkout. Radiation safety requirements make access to the radiation areas where detectors are located difficult and time consuming. Such time losses cannot be tolerated in the multi-user storage ring environment; access to the detector is limited.

Since characteristic electrodynamic cross sections and the machine luminosity are small, the interesting data rate ($\sim\sigma_{\mu\mu}\cdot\mathscr{L}$) is quite low, usually less than 1 Hz. The combination of widely varying background rates, low "good" data rate, and rapidly changing physics as a function of beam energy forces the need for a flexible and easily changed detector triggering scheme. The important variables that detector triggering depends upon are: number of

charged prongs, track momenta, total energy deposited, position of the event vertex (both along the beam line (z) and radially away from it (r)), time of the event relative to beams crossing, and the topological arrangement of prongs (collinearity, coplanarity,...). The main backgrounds to be be eliminated by the triggering scheme are beam-gas and beam-wall interactions, synchrotron radiation, and cosmic rays.

II. Implications for Data Acquisition Systems Design

The features of storage ring operation mentioned above have important implications for the design of data acquisition systems. Operation of the detection apparatus synchronously with the beams crossing requires no chamber or counter signal delay elements. Apparatus design should allow all essential information to be stored on each beam crossing and replaced if unwanted. No multievent hardware storage capability is required for the purpose of data read in.

The low data rate characteristic of storage ring operation allows data acquisition to proceed slowly ($\sim$0.1 sec/event). This long acquisition time allows a large amount of peripheral processing to be performed. Microprocessors can control collection, compaction, and correction of raw data before interruption of the host computer and data transfer to tape. A large amount of

hardware multiplexing is acceptable, eliminating the need for duplication of expensive hardware.

The low rate of interesting data does not imply a small off-line computing workload. A typical e^+e^- storage ring experiment requires $\approx$1 IBM 370/168 for off-line analysis. The sample of events to be analyzed must be as free of backgrounds as possible. Advantage of the long acquisition time and synchronous operation can be taken in the detector trigger by use of a hierarchical triggering scheme. Such schemes are cheap and reliable, and should be programmable and easily tested.

The time available during the frequent periods of injection can be used for hardware calibration and checkout. Such frequent calibrations eliminate the need for fancy standards on cables, time-to-amplitude converters, sample and hold units, etc. Only precision calibrators are required. The hardware calibration provides a convenient high statistics method for determining electronics related constants (gains, pedestals,...), and monitoring the stability of the electronics under changing conditions of beams, temperature, etc. The failure detection capabilities of the calibration system are maximized by input of calibration signals as far upstream (i.e., before preamplification) as possible. System design should allow easy change from data collection mode to calibration mode and back again with no access to the detector.

Use of microprocessors in the data acquisition system provides both advantages and possible pitfalls. Correction of the raw data simplifies the structure of the analysis programs. The electronics related constants, for example, can be transmitted by the host computer to the microprocessors, eliminating a (large) lookup table in the on-line and off-line programs. Also, microprocessors provide greater flexibility for changing hardware configurations, merely requiring reprogramming rather than redesign. Any such system with peripheral processing of raw data requires extensive error checking to ensure valid data are written to tape. The host computer, by analyzing a sample of the incoming data, provides a constant monitor of detector performance. This monitoring, along with checks performed before and during data collection, provides protection against possible hardware failure.

III. Data Acquisition in the Mark II

A. Design Features

The Mark II electronics design features a hierarchical triggering scheme, synchronous operation with limited use of signal delay elements, extensive use of multiplexed hardware and microprocessors, and use of precision calibrators. The basic components of the electronics system are organized around the detector components: TOF system for the scintillation counter information, time-to-amplitude converters (TAC's) for the drift chamber information, and sample and hold units (SHAM's) for the shower counter information.

The TAC's and SHAM's form systems of multiplexed analog modules processed in large groups by a single analog to digital converter ('ADC'). The TAC's (SHAM's) are stopped and cleared (gated) by signals derived from the beam pickup signal. The TAC's and SHAM's operate in true synchronous fashion, refreshing the data from each input channel every beam crossing. The data are continually refreshed until a trigger occurs and further data is inhibited while the event is read out.

The counter data are handled in a conventional fashion; signal delay elements are needed. The counter signals are split (80-20), delayed ($\sim$500 nsec), and sent to LeCroy 2228 TDC's and 2249 ADC's. The delay is long enough to allow time to make a trigger decision and start (gate) the TDC's (ADC's). These modules lack the fast clear feature needed for synchronous storage ring operation, but were used because they were commercially available. Complete details of the TAC's, SHAM's and preamplification systems can be found in Reference 51.

B. Triggering the Detector

The Mark II trigger is derived from signals from a beam pickup electrode, pipe counters, TOF counters, and drift chamber wires. The trigger is a two-tiered system, involving a fast "primary" trigger and a slower "secondary" trigger.

The primary trigger is formed from signals from the beam pickup, pipe counters, and drift chamber wires.

Figure 62 shows a block diagram of the primary trigger logic. The drift chamber signal used in the primary trigger ("drift chamber majority," or "DCM") is formed ∿10 nsec after TAC stop from an "or" of all the wires in each layer, and is true if ≥4 of 9 layers have a hit. A primary trigger occurs if DCM, 2 of the 4 pipe counters, and the beam crossing signal are coincident. The primary trigger signal starts the secondary trigger logic and inhibits resets while the secondary trigger is operating. If the secondary trigger logic fails to find a valid trigger configuration, the system becomes ready for the next beam crossing signal after a ∿35 μsec delay. Typical primary trigger rates at SPEAR are 30 Hz to 2 kHz, depending on beam conditions. The pipe counter is included in the primary trigger to discriminate against cosmic rays; the DCM information helps select triggers with charged tracks.

The secondary trigger logic inspects the inner 3 stereo layer and the axial layer drift chamber latch information for evidence of charged tracks. The drift chamber latch information is parallel loaded into shift registers in the TAC's at TAC stop time. If a primary trigger occurs, the shift register information is shifted out serially and inspected for evidence of tracks within various curvature "roads." Duplicate tracks are removed and the numbers of tracks of two types are counted by "track counters." The first track type ("A" track) is defined by requiring hits

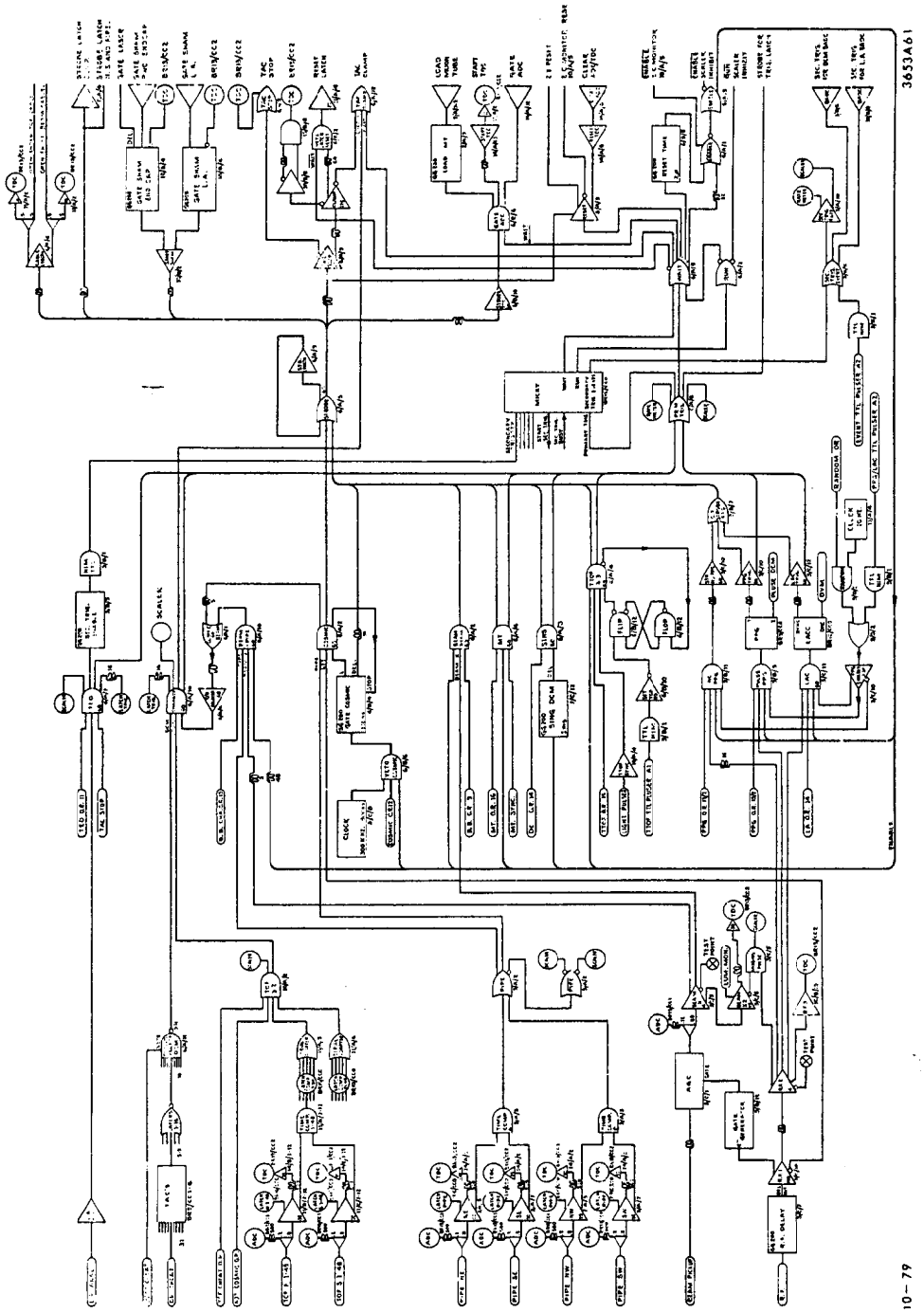

Fig. 62. Primary trigger logic for the Mark II detector.

in a road on at least 4 of the 6 axial layers, and a time-of-flight counter on the end of the track. The second type ("B" track) is defined by requiring hits in a road on at least 3 of the inner 5 drift chamber layers. The number of tracks in the two track types is compared against preset trigger criteria. If the preset trigger criteria are satisfied, a secondary trigger signal is generated that starts the microprocessors and interrupts the host computer (VAX 11/780). Pattern recognition information from the secondary trigger logic is saved for later use by off-line tracking routines. The algorithms used in the track finding hardware are discussed in Reference 52.

The trigger system is disabled for ∿60 msec while the data are transferred to memory by the VAX. For a secondary trigger rate of ∿3 Hz, the detector livetime is ∿90%. The Mark II triggering system is powerful, flexible, and easily programmable. The main drawback of this triggering system is its inability to discriminate the z position of the event vertex. All other important charged track triggering variables are (or could easily be) incorporated into the existing hardware.

C. Drift Chamber and Liquid Argon Pulse Height Readout Using the BADC

The same microprocessor and ADC system ("Brilliant ADC" or "BADC") converts the TAC and SHAM analog information into digital form. The BADC's perform the operations

of collection, compaction, and correction of the analog data, amortizing the cost of the microprocessor over each CAMAC crate of up to 608 input channels. Details of the BADC readout system design are given in Reference 53. The analog signals are gated by CAMAC command from the BADC onto a common buss connected to the ADC. The ADC digitizes the analog signal, and passes the value to the arithmetic and logic unit, or 'ALU.' The ALU checks to see if the ADC value is above a threshold set independently for each channel. If so, the ADC value is corrected using the following algorithm: If Q is the raw ADC value, and $Q' = Q-\delta$, then $\tilde{Q} = Q'(\alpha + \beta Q')$ where α, β, and δ are constants for each channel. The value of Q along with the logical channel label (drift chamber layer and wire or liquid argon module, layer, and strip) is stored in BADC memory for subsequent host readout. The algorithm is implemented in a 256 word PROM, with the identical program in each of the 14 BADC's. The information relating physical channel to logical channel, the thresholds, and the correction constants are loaded through CAMAC into a 4K RAM in each BADC at begin run time. Table 15 shows the generalized format for the BADC constants table.

This generalized BADC system allows reduction of event data acquisition time, reduction of host computer processing time, and simplifies the structure of the analysis program by eliminating $\sim$28000 constants.

TABLE 15

FORMAT FOR BADC CONSTANTS TABLE[54]

MEMORY LOCATION	DESCRIPTION		
0	buffer pointer		1 set for each segment
1	test control word		
2	number of segments		
3	number of channels in segment 1		
4	mux starting address for segment 1		
5	base for segment 1		
6	ε for channel 1	1 set for each channel	
7	δ for channel 1		
8	β for channel 1		
9	α for channel 1		
10	ε for channel 2		
11	δ for channel 2		
12	β for channel 2		
13	α for channel 2		
"			
"			

IV. Calibration

A. Design Features

The use of the BADC and the similarity between time and charge measurements allows use of standard hardware and software for calibration of the different systems. The general technique involves choosing settings for the calibration controller, which generates calibration signals, measuring $\langle Q \rangle$ and $\langle Q^2 - \bar{Q}^2 \rangle$ for each setting and input data channel, and then fitting a curve for each input channel through the resulting $\langle Q \rangle$ values. The curve parameters are then used to determine α(gain), β(quadratic), δ(offset), and ε(threshold) for each input channel. By calculating $\langle Q \rangle$ and $\langle Q^2 - \bar{Q}^2 \rangle$ in the BADC's, large slow data flows to the main CPU are eliminated. For ease of operation, the primary trigger logic is arranged such that at begin run time the system to be calibrated can be selected by setting hardware output register bits (Figure 62). In order to take full advantage of the failure detection capabilities of the calibration system, the calibration signals are generated in such a way as to mimic as closely as possible the effect of actual data signals. The calibration signals are injected onto the actual signal pickup devices, ahead of preamplification. Further, the range in pulse height (SHAM's) or time (TAC's) in the calibration exceeds the range for actual colliding beam data. Remotely programmable calibration controllers allow complete computer control of the entire

calibration sequence; no cables or switches need to be moved or can be left in positions such that colliding beam data could be destroyed.

The determination of ε, α, β, and δ for each channel is made after completion of the fits. The BADC algorithm is implemented in 16 bit 2's complement arithmetic with a multiplication performed as follows: two 16 bit integer numbers are multiplied to yield a 32 bit product, the lower 16 bits are truncated, and this result stored as the final answer. The floating point constants α and β determined from the fit parameters must be converted to 16 bit integers and modified to take into account the multiplication algorithm in the BADC. This conversion is properly accomplished by setting IALPHA = $\alpha x\ 2^{16}$, IBETA = $\beta x\ 2^{32}$, and then checking for overflow of 16 bits.

Location of electronics failures in the several thousand input channels is achieved by inspecting the fit parameters. Bad channels are located by finding the fit parameters or fit chisquare outside tolerances. Summary lists of such bad channels are automatically compiled and displayed for CAMAC crate and for system layer (drift chamber) or module (liquid argon). Additional information provided is a summary of failures by number of channels out of tolerance for each fit parameter and fit chisquare. Other information, such as histograms of fit parameters over all channels in the system, and individual channel fits, is

compiled and easily displayed. Channels failing the calibration cuts can be "turned off" in BADC software by setting the threshold (ε) for that channel very high. This allows removal of "hot" wires, channels with wires removed or connections lost, and removal from the data of "flaky" channels until the hardware can be fixed.

B. Drift Chamber Calibration

The calibration controller for the drift chamber calibration is a pulse pair generator (PPG). The PPG contains a stabilized quartz crystal oscillator, and outputs a timed pulse pair after receipt of a front panel interrupt. The time separation of the pulse pair is controlled from a CAMAC register. One pulse of the pair is amplified and fanned out to the high voltage lines of each of the 16 drift chamber layers, through the high voltage distribution boxes.[43] The signal ($\sim$10 $\times$ threshold) is picked up by capacitive coupling to the chamber sense wires, amplified by the drift chamber preamps, and send back to generate TAC start for each input channel. TAC stop and BADC start are generated by the other pulse from the PPG (Figure 62).

The VAX controls the calibration sequence. The accumulators in the BADC's for $\langle Q \rangle$ and $\langle Q^2 - \bar{Q}^2 \rangle$ are cleared, and the PPG time set. The VAX then pulses the PPG, and waits until the BADC's have finished their calculation. The VAX then generates another pulse pair by pulsing the PPG, and so on, until 50 points are taken. The BADC's

are then read in, the $\langle Q \rangle$ and $\langle Q^2 - \tilde{Q}^2 \rangle$ values stored, the BADC accumulators reset, and a new time written to the PPG. Six such runs are taken, five to determine the fit parameters (α, β, δ), and one to determine the pedestal value (ε). Only linear fits are used ($\beta = 0$).

The rms resolution of the system, averaged over all channels, is about 900 psec. The constants are adjusted so that the numbers stored for $\tilde{Q}$ by the BADC during colliding beam running are in 0.1 nsec units, with zero being a direct hit on the sense wire.

C. Liquid Argon Calibration

The calibration controller for the liquid argon calibration is a DAC. The liquid argon calibration is accomplished by injecting a known charge into the preamplifier inputs within the module. This is accomplished by charging a known capacitance to a known voltage from the DAC. The capacitors are then discharged into the modules using FET switches. A sync signal from the DAC module is used to synchronize the FET switches, the SHAM gate signal and BADC start (Figure 62). Using the same method as in the drift chamber case, the DAC is remotely programmable via CAMAC, and 6 points are taken, 5 for the fit parameters and one to check the calibrator noise. Quadratic terms are retained in the fit. The constants are adjusted so that $\tilde{Q}$ calculated by the BADC during colliding beam running is in units of 0.1 MeV collected energy.

REFERENCES

1. Terazawa, H., Rev. Mod. Phys. 45, 615 (1973).
2. $\mu\pi$ group: F. Ceradini et al., Phys. Lett. 47B, 80 (1973).
   $\gamma\gamma$ group: C. Bacci et al., Phys. Lett. 44B, 533 (1973).
   Boson group: B. Bartoli et al., Phys. Rev. D6, 2374 (1972).
   BCF group: M Barnardini et al., Phys. Lett. 51B, 200 (1974).
3. G. Cosme et al., Phys. Lett. 40B, 685 (1972).
4. L. M. Kurdadze et al., Phys. Lett. 42B, 515 (1972).
5. A. Litke et al., Phys. Rev. Lett. 30, 1189 (1973),
   Ibid, 1349 (1973).
   G. Tarnopolsky et al., Phys. Rev. Lett. 32, 432 (1974).
6. B. Richter, Invited talk at Conference on Lepton Induced Reactions, Irvine, California, December 1973.
7. J.-E. Augustin et al., Phys. Rev. Lett. 33, 1406 (1974).
8. J. J. Aubert et al., Phys. Rev. Lett. 33, 1404 (1974).
9. C. Bacci et al., Phys. Rev. Lett. 33, 1408 (1974),
   Ibid, 1649 (1974).
10. W. Braunschweig et al., Phys. Lett. 53B, 393 (1974).
11. G. S. Abrams et al., Phys. Rev. Lett. 33, 1453 (1974).
12. S. D. Drell and T. M. Yan, Phys. Rev. 187, 2159 (1969),
    Ibid, Phys. Rev. D1, 1617 (1970), R. P. Feynman,
    Photon-Hadron Interactions (1972).
13. T. Appelquist, H. D. Politzer, Phys. Rev. D12, 1404 (1975).
14. G. Hanson et al., Phys. Rev. Lett. 35, 1609 (1975).

15. Y. S. Tsai, Phys. Rev. D12, 3533 (1976).

16. J. D. Bjorken, Phys. Rev. 179, 1547 (1969).

17. G. J. Feldman et al., Phys. Rev. Lett. 38, 1489 (1977).
M. L. Perl et al., Phys. Rev. Lett. 35, 1489 (1975).

18. J. S. Whitaker, Ph.D. Thesis, LBL Report LBL-5518 (1976).

19. In muon pair events the accidental probability is <0.3%. We conclude that most of the accidentals in hadron events are due to photons from hadron decays.

20. For details of track reconstruction, see R. J. Hollebeek, Ph.D. Thesis, LBL Report LBL-3874 (1975).

21. Electrons are identified by pulse height criteria in the shower counters. If $x(= 2p/\sqrt{s}) > 0.3$, then the track is identified as electron if the pulse height is greater than $(62 \cdot p(\text{GeV}) - 5 \cdot p^2(\text{GeV}))$. Due to the poor shower counter resolution, the additional topological requirements were needed to ensure no hadronic events were lost due to these cuts.

22. S. J. Brodsky et al., Phys. Rev. D4, 1532 (1971).
J. E. Zipse, Ph.D. Thesis, LBL Report LBL-4281 (1975).

23. J. Parisi et al., Phys. Rev. D4, 2927 (1971).

24. M. L. Perl et al., Phys. Rev. Lett. 35, 1489 (1975).
W. Bacino et al., Phys. Rev. Lett. 41, 13 (1978).
Y. S. Tsai, Phys. Rev. D4, 2821 (1971).
G. Feldman, Proc. of the 19th International Conference on High Energy Physics, Tokyo, 777 (1978).

25. J.-E. Augustin et al., Phys. Rev. Lett. 27, 233 (1975).

26. F. A. Berends et al., Nucl. Phys. B68, 541 (1974) and B63, 381 (1973).

27. CERN Courier 16, 356 (1976).

28. G. Hanson et al., Phys. Rev. Lett. 35, 1609 (1975).

29. G. Bonneau and F. Martin, Nucl. Phys. B27, 381 (1971). The diagrams included in the radiative correction are shown in Figure 21.

30. R. F. Schwitters, Proc. 1975 Int. Symposium on Lepton-Photon Interactions at High Energies, Stanford, 1975, p. 5.

31. J. Siegrist et al., Phys. Rev. Lett. 36, 700 (1976).

32. P. Rapidis et al., Phys. Rev. Lett. 39, 526 (1977), Ibid 39, 974 (1977).

33. We employed cubic polynomials ("splines") tied together at breakpoints with continuous first and second derivatives. The routines ICSFKU and ICSSCU from the IMSL program library were used to accomplish the data smoothing. See Appendix II.

34. J. D. Jackson and D. L. Scharre, Nucl. Inst. & Methods 128, 13 (1975).

35. Resonance parameters are from SLAC-PUB-1955 presented by V. Lüth at the International Conference on High Energy Physics, Palermo (1975).

36. P. Rapidis et al., Phys. Rev. Lett. 39, 526 (1977). Ibid 39, 974 (1977).

W. Bacino et al., Phys. Rev. Lett. 40, 671 (1978).

37. J. Siegrist et al., Phys. Rev. Lett. 36, 700 (1976).

38. J. Burmester et al., Phys. Lett. 66B, 395 (1977).

39. R. Brandelik et al., Phys. Lett. 76B, 361 (1978).

40. SLAC-PUB 2315 presented by D. L. Scharre at the 14th Recontre de Moriond, Les Arcs (1979).

41. R. Brandelik et al., Nucl. Phys. B148, 189 (1979).

42. T. Appelquist and H. Georgi, Phys. Rev. D12, 1404 (1975).
E. C. Poggio et al., Phys. Rev. D13, 1958 (1976).

43. W. Davies-White et al., Nuclear Inst. and Methods 160, 227 (1979).

44. G. S. Abrams et al., IEEE Trans. on Nuclear Science, NS-25, 309 (1978).
G. S. Abrams et al., SLAC-PUB 2331 (1979), sub. to Phys. Rev. Lett.

45. H. Brafman et al., IEEE Trans on Nuclear Science, NS-25, 692 (1978).

46. Electrons are identified as tracks into the liquid argon barrel ($|\cos\theta| < 0.65$, 40 mrad away from cracks between modules) that have pulse height $> 0.5p + 0.25$ for momentum $p > 0.9$ GeV.

47. We discarded events with ≥ 1 track, $x \geq 0.7$ and:
a. 5 or 6 prongs with ≥ 2 electrons.
b. 4 prongs with ≥ 1 electron.
c. 3 or 4 prongs with the $x > 0.7$ track collinear ($\leq 10°$) with another track of $x > 0.4$.

48. F. A. Berends et al., Nucl. Phys. B68, 541 (1974) and B63, 381 (1973).

49. R. Brandelik et al., Phys. Lett. 76B, 361 (1978).

50. T. Appelquist and H. Georgi, Phys. Rev. D8, 4000 (1973).
A. Zee, Phys. Rev. D8, 4030 (1973).
T. Appelquist and H. D. Politzer, Phys. Rev. D12, 1404 (1975).
F. J. Yndurain, Nucl. Phys. B136, 533 (1978).
M. Dine and J. Sapirstein, Phys. Rev. Lett. 43, 668 (1979).

51. G. S. Abrams et al., IEEE Trans. on Nuclear Science, NS-25, 309 (1978).
W. Davies-White et al., Nuclear Instr. and Methods 160, 227 (1979).
E. L. Cisneros et al., SLAC-PUB-1844 (1976).

52. H. Brafman et al., IEEE Trans. on Nuclear Science, NS-25, 692 (1978).

53. M. Breidenbach et al., SLAC-PUB-2032 (1977).

54. Here buffer pointer is the pointer to the first free word in BADC memory and test control word controls whether the BADC is in data acquisition mode or calibration mode. A "segment" is a drift chamber layer or liquid argon strip. The MUX starting address is 32x CAMAC slot position plus starting channel number. The "base" is the starting channel label (corresponding to the hardware address in word 4) that is incremented by one for each channel in the segment.